Doctoral Dissertation
Doctoral Program in Civil and Environmental Engineering (34^{th}cycle)

A novel functional coating and a reliable design approach to fully exploit the strength of annealed glass

By

Gregorio Mariggiò

******

Supervisor(s):
Prof. M. Corrado, Supervisor
Prof. G. Ventura, Co-Supervisor

Doctoral Examination Committee:
Prof. M. Paggi, Referee, Scuola IMT Alti Studi di Lucca
Prof. J. Schneider , Referee, Technical University of Darmstadt
Prof. P. Cornetti, Politecnico di Torino
Dr. L. Galuppi, Università di Parma
Dr. C. Kothe, Technical University of Dresden

Politecnico di Torino
2022

Declaration

I hereby declare that, the contents and organization of this dissertation constitute my own original work and does not compromise in any way the rights of third parties, including those relating to the security of personal data.

Gregorio Mariggiò
2022

* This dissertation is presented in partial fulfillment of the requirements for **Ph.D. degree** in the Graduate School of Politecnico di Torino (ScuDo).

This thesis is dedicated to my loving parents

Acknowledgements

First, I would like to express my heartfelt gratitude to my supervisors Prof. Mauro Corrado and Prof. Giulio Ventura for their invaluable guidance, for their constant support, and for the many hours spent in discussions which contributed to the development of new ideas and methods. Their knowledge, experience and suggestions made me grow significantly both professionally and personally.

Throughout this project, I have met a number of additional experts, all of whom have provided invaluable contribution and advise. A special thank goes to Prof. Roberta Bongiovanni and Dr. Sara Dalle Vacche for their contribution in the chemical aspects involved in this thesis. Moreover, Prof. Christian Louter deserves a special appreciation for providing me with essential feedback that considerably improved the quality of the project.

In addition, the financial supports of the Italian Ministry of Education to the project "XFAST-SIMS: Extra fast and accurate simulation of complex structural systems" and of Politecnico di Torino and Compagnia di San Paolo to the project "GLASS & CO: Enhancing the effective strength of structural glass with functional coatings" are gratefully acknowledged.

The author also wish to thank Eng. Luisa Gaiero and Eng. Stefano Forzano for thier help in preparing the specimens and Eng. Simona Bargiacchi and Dr. Luca Contiero from Cromology Italia S.p.A. for their active contribution to the project, and in particular for carrying out the artificial weathering of the glass specimens.

For the extraordinarily great atmosphere inside and outside the workplace, I would like to thank my colleagues and friends Alessio, Gianmarco, Sebastiano F., Giulia, Domenico, Francesco, Sebastiano R., Silvio, Gianfranco.

Finally, I must express infinite gratitude to my family for the unwavering support, and to Delia, simply because she has always been close to me, providing me with her support for so many years.

Abstract

Glass is increasingly being used in structural applications nowadays. Large glass façades, all-glass staircases, roofs, walkways, and spectacular long suspended bridges are all hallmarks of the modern architecture. However, the intrinsic strength of annealed glass is not fully exploited due to the stress corrosion and the lack of a universal and reliable design method. Therefore, the design of glass components is redundant and conservative, resulting mainly in costs and emissions increase. Moreover, from an architectural point of view, oversized load-bearing glass members are undesirable.

Stress corrosion is a chemical phenomenon which affects annealed glass. This phenomenon, also known as static fatigue, causes a reduction of the tensile strength due to the combined presence of applied tensile stress and humidity. As a result, the actual strength of annealed glass components is limited. According to previous findings published in the literature, stress corrosion can be prevented by avoiding the interaction between water molecules and the silica network.

Besides the stress corrosion, the glass strength is prevented from being fully exploited due to the lack of a generally valid design approach. The large dispersion in size and position of flaws determines a wide variability of the failure stress, hence a distinct and universally acceptable glass strength cannot be identified. As a consequence, deterministic approaches, that nowadays are widely adopted for the design of glass components, lose in reliability and enforce to adopt large safety factors, limiting the actual load-carrying capacity of glass members. Several researchers have raised serious concerns regarding the applicability and accuracy of the deterministic design approach. The main reason of concern is that the glass strength is not a true material property since it varies, not only with the statistical flaws distribution, but also with the test setup and the element size.

In the first part of the research project, a UV cured coating combining hydrophobicity and barrier to water vapour with good adhesion to glass, has been investigated and developed for preventing stress corrosion in annealed glass. The coating is obtained by combining a cycloaliphatic diacrylate resin with a very low amount of a perfluoropolyether methacrylate co-monomer, which migrated to the free surface, creating a compositionally graded coating. The adhesion to glass is improved, using as a primer an acrylated silane able to co-react with the resins. The coating effectiveness is assessed experimentally by comparing the load-carrying capacities of coated and un-coated glass plates. New and naturally aged glasses are analysed. The results evidence an increase of the design bending strength between 60 and 90% with respect to the strength of un-coated glass. The durability of the polymeric coating is also examined. Three scenarios are analysed in terms of ageing: (i) cyclic loading, carried out by subjecting coated samples to repetitive loading; (ii) natural weathering, performed by exposing coated samples to atmospheric agents; (iii) artificial weathering, conducted by exposing coated specimens to fluorescent UV lamps, heat and humidity. The coating's durability is determined indirectly, based on its residual effectiveness in preventing stress corrosion, by comparing the bending strength of aged coated glass specimens to that of un-coated and freshly coated specimens using the coaxial double ring test. The obtained results demonstrate that the proposed formulation is nearly insensitive to cyclic loading, has excellent performance in case of natural weathering, while is slightly more sensitive to artificial weathering.

In the second part of the research project a novel computational methodology aiming for a safe and optimized design of glass components has been developed. The methodology, that adopts a stress intensity factors-based fracture criterion, can be applied to predict the edge strength of glass components with arbitrary geometry and edge flaws scenario. The novel developed methodology consists of: (i) modelling the structural element through the finite element method, (ii) randomly applying to the FE model a population of flaws extracted from a pre-defined statistical distribution function, (iii) computing the related stress intensity factors, (iv) evaluating the load carrying capacity by equating the maximum stress intensity factor to the fracture toughness. Because of the stochastic nature of the problem, where the size of the edge flaws is the random variable, the Monte Carlo method is used to obtain the cumulative distribution function of the failure load. Finally, the critical load referred to a chosen probability of failure is derived. The eXtended Finite Element method is used because of its intrinsic capability to deal with multiple cracks of any position

and length without adapting the mesh topology, and because it allows for a direct evaluation of the stress intensity factors at the tip of the cracks without any post-processing. The current version of the numerical methodology is limited to plane stress/strain models, although its extension to 3D problems is quite straightforward. Several case studies are shown to demonstrate the accuracy and reliability of the method in assessing the structural integrity of glass components. It is also shown that by adopting the developed method rather than a stress-based approach, the load-carrying capacity prediction increases by 21 to 82%, depending on the stress gradient along the glass component. In conclusion, the methodology provided has huge potentiality for being generalized for all brittle materials and thus applied to ceramics as well as polysilicon structures for micro-electro-mechanical systems (MEMS).

Contents

List of Figures

List of Tables

Chapter 1

Introduction

1.1 Background and motivation

The use of glass in the building industry is evolving towards structural applications: modern architecture features large glass façades, all-glass staircases, roofs, walkways and spectacular long suspended bridges. The Apple store on 5th Avenue in New York, the Grand Canyon skywalk, the brick façade of the Chanel store in Amsterdam [7] are just few examples of the latest innovative architectural solutions based on the structural use of glass. Intensive research over the previous decade has resulted in the development of novel structural elements including, among others, bricks, post-tensioned glass beams [8], sandwich structures with thin and ultra-thin glass panes [9], and new recipes, thus fostering the use of glass for structural components. From a structural and architectural standpoint, high compressive strength (greater than 200 MPa [10]) and transparency are the most appealing properties of glass. However, transparency is not just a beauty characteristic; it also allows for energy savings. As for example, the use of glass provides for natural daylight, reducing the energy consumption due to both artificial lighting and heating. In addition, the use of photovoltaic glass in building façades allows to generate energy. All these factors contribute to make glass a valuable material in modern structures, helping the achievement of the environmental sustainability.

Glass, on the other hand, is a challenging building material due to its almost perfect elastic-brittle mechanical response and sensitivity to cracking. The exploitable tensile strength of glass varies extremely in the range of 200 to 500 MPa [11], depend-

ing on the size of surface flaws and the presence of chemical or thermal treatments. Aiming at increasing the reliability of glass as structural material, nowadays, several aspects related to the tensile strength are still object of study: the relation between the size of surface flaws and the strength [12–14], the effect of ageing [15–17], the effectiveness of repairs on strength recovery [18], the derivation of the best statistical distribution function for the strength to be included in the probabilistic approach for structural design [19, 20], the micro cracks detection by means of the thermal stress-induced light scattering method [21], and the automatic scratch detection using deep learning approaches [22].

However, the structural design and optimization of load-bearing glass components continues to be a challenge. Griffith flaws cause the brittle failure in glass [23]. Flaws and scratches occur during the manufacturing process, as well as during handling, assembly, everyday use and maintenance [24]. Therefore, the flaw size and position, as well as the glass strength have a large dispersion. In certain cases, experimental findings provide scattered values of the glass strength with a spread of 30-50% with reference to the mean strength [25]. This results in a lack of confidence about glass structure design methods based on deterministic approaches, as well as the introduction of large safety factors to guarantee a safe design. Several researchers have questioned the suitability and validity of these common glass design approaches, even given the narrow scope for which they were developed [26–30]. The deterministic approaches, adopted by the European standards [4, 31], rely on a parameter, namely glass strength, which is commonly derived for glass surfaces exposed to uniform biaxial tensile stress. As a consequence, the application of these approaches is not strictly appropriate in case of arbitrary supporting and loading conditions, as for example in-plane or concentrated loads and connections [26]. Especially because the glass strength is not a true material property, as it depends on the flaws size distribution, the fracture toughness, the test setup, as well as the specimen size and geometry [28, 32–34].

Besides the brittleness, the sensitivity to cracks, and the absence of a design method that could include any case study, the stress corrosion phenomenon limits the exploitation of the intrinsic tensile strength of annealed glass. Stress corrosion is a degradation phenomenon which concerns the sub-critical growth of flaws and micro-cracks, with a consequent decrease of the tensile strength of the material over time [35]. Several studies agree that stress corrosion is caused by the combine action of water and applied stress [35, 2, 36, 37].

1.2 Main objectives

The current research looks into the two challenges described above in relation to the use of glass for structural applications, and strives to address them. To summarize, this project focuses on developing a novel strategy for preventing stress corrosion in glass and a new reliable design approach for the structural optimization of glass component. These two topics are covered separately in this thesis, however, they were combined since they both aim to fully exploit the strength of annealed glass and enhance its reliability while also pursuing for a more sustainable design.

In order to solve the issue of stress corrosion, a UV cured coating combining hydrophobicity and barrier to water vapour with good adhesion to glass, has been investigated and developed. Different methods for overcoming stress corrosion have been discovered; currently, the most well-known solutions for glass strengthening are based on tempering processes, producing a surface compression state through thermal or chemical treatments [38]. On the contrary, these methods have a number of drawbacks, including significant energy costs and/or long treatment periods [39]. Protective polymeric coatings can be an effective alternative since they limit the intervention to the surfaces of glass while keeping the structural component's transparency. UV-cured coatings are preferable in most circumstances because they are environmentally friendly: they do not include solvents and hence emit fewer toxic organic vapours. Furthermore, because the polymerization occurs in a few of seconds and does not require heating, costs are minimized.

To assess the strength of structural members made of annealed glass a new and reliable computational design approach is here presented and tested. The proposed approach combines finite element analysis, fracture mechanics theory and Monte Carlo simulations for the reliable prediction of the load-carrying capacity of glass components. Instead of using a stress-based failure criterion, the design approach adopts a stress intensity factor-based criterion. The extended finite element method (XFEM) is used to model cracks and for the direct evaluation of the stress intensity factors at crack tips. Using the XFEM approach, in fact, cracks are introduced mathematically, rather than physically, in finite element models, by enriching the standard approximation of the displacement field [40–42]. This allows for modelling an arbitrary number of cracks in any position without the need for local mesh refinement around cracks. The current version of the developed computational methodology is limited to plane stress/strain models, therefore it can be used for

the prediction of the edge strength of any flat glass component under in-plane static loads. However, the extension of the proposed method to 3D problems is quite straightforward.

1.3 Organization of the thesis

This dissertation consists of seven chapters, organized as follows:

Chapter 2 - The stress corrosion phenomenon is introduced. Moreover, a compositionally graded hydrophobic UV-Cured coating for the prevention of glass stress corrosion is presented. The details of the chemical formulation and preparation of the coating are provided. Additionally, the physical, chemical and mechanical properties of the coating are investigated.

Chapter 3 - The effectiveness of the coating in preventing glass stress corrosion is assessed by comparing the failure stress of coated and un-coated glass specimens. The experimental data are treated statistically using the Weibull, Normal and Log-Normal distributions. Moreover, the goodness of fit of the three statistical distributions to the data is evaluated with the Anderson-Darling test. Finally, a detailed fractographic analysis is conducted to correlate measured failure stress values with crack sizes.

Chapter 4 - The durability of the coating is investigated. In this regard, three types of ageing are considered: *(i)* mechanical ageing by subjected coated samples to cyclic loads; *(ii)* natural weathering carried out by exposing coated glass samples to atmospheric agents; *(iii)* artificial weathering conducted by exposing coated specimens to fluorescent UV lamps, heat and water.

Chapter 5 - A new computational methodology for the structural integrity assessment of glass components is introduced. The application field, the assumptions underlying the approach and the parameters which influence the glass strength are all discussed. In addition, the extended finite element method (XFEM) is presented for the direct evaluation of the stress intensity factors at the crack tips.

Chapter 6 - A number of examples are solved to evaluate the accuracy of the developed XFEM-based methodology. Different scenarios are investigated to identify the limits to the applicability of the method. The influence of the crack inclination with respect to the mesh orientation and the number of Gauss points

on the evaluation of the stress intensity factor is studied. Moreover, the stress intensity factor is calculated for different values of crack length in order to identify the minimum crack length with respect to the mesh size. Finally, the effectiveness of the method is evaluated for cracks located near stress concentration regions as well as interacting multiple edge cracks.

Chapter 7 - Several case studies are analysed with the proposed computational design approach to demonstrate its accuracy and reliability in assessing the structural integrity of glass components. A comparative study is conducted to show the differences between the stress-based design approach and the proposed one. The influence of the stress gradient on the load-carrying capacity of glass components is investigated using four different test configurations: a specimen under uniaxial tensile load, a beam under three point bending, a simply supported beam under uniformly distributed load, and a cantilever beam subjected to uniformly distributed load.

Chapter 2

Stress corrosion in glass and a mitigation strategy[1]

2.1 Introduction

The purpose of this Chapter is to introduce the phenomenon of stress corrosion in glass and to provide a solution for preventing it. Stress corrosion is a chemical-physical phenomenon which limits the exploitation of the intrinsic tensile strength of annealed glass. Stress corrosion is also known as static fatigue and consists in a reduction of the material strength caused by the combined action of applied stress and humidity on the silica network that composes glass. The classical theory to account for this phenomenology involves the chemical reaction of water molecules with the silica network, taking place at the tip of the cracks, although other interpretations have been also provided [43].

Static fatigue in glass was discovered at the end of the 19*th* century by Grenet [44], who observed that the strength of glass depended on the rate of loading or on the length of time a load was applied. However, only in the 1960s' a clear explanation was found for this phenomenon. In that decade, several experimental tests were carried out that permitted to identify different stages of crack propagation in glass

[1] Part of the work described has been previously published in:
S. Dalle Vacche, G. Mariggiò, A. Vitale, R. Bongiovanni, M. Corrado. Compositionally graded hydrophobic UVcured coatings for the prevention of glass stress corrosion. Coatings 9, 424 (2019).
G. Mariggiò, S. Dalle Vacche, R. Bongiovanni, C. Louter, M. Corrado. Enhancing the design bending strength of new and aged glass with a functional coating. Glass Struct. Eng. 5, 135–146 (2020).

and to measure the effects of water and water vapor on the sub-critical propagation of microcracks [2, 36]. As represented by the schematic representation shown in Fig. 2.1, there is a threshold for the applied stress below which crack propagation does not occur, even in the sub-critical regime. Once the threshold is overcome, three regions are evidenced for crack propagation velocity. In region I the crack velocity is dependent on the applied stress; in region II the crack velocity is nearly independent of the applied stress; in region III the crack velocity is again function of the applied stress, however, the slope is very steep, relating to an unstable crack propagation that occurs when the stress intensity factor overcomes the material toughness, $K_{\mathrm{I}} > K_{\mathrm{IC}}$. The stress corrosion occurs in regions I and II that, in fact, are highly influenced by the amount of environmental humidity.

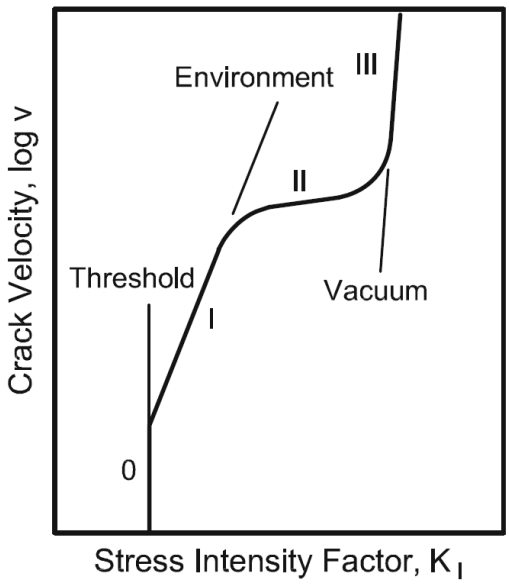

Fig. 2.1 Velocity of a running crack versus the stress intensity factor (adapted from [1])

Pioneering experimental studies carried out by Wiederhorn [2] allowed to derive empirical relationships between the sub-critical crack propagation velocity and the stress field - represented by the stress intensity factor at the crack tip - for different percentages of environmental humidity (see Fig. 2.2). According to Fig. 2.2 the effect of an increasing amount of water in the environment is a shift of region I towards lower values of K_{I}, without changing the slope, and a shift of region II towards higher values of crack velocity.

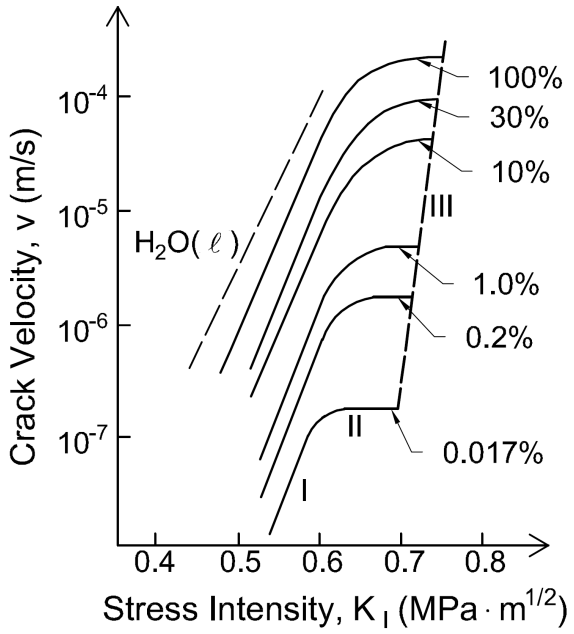

Fig. 2.2 Effect of humidity on the crack propagation in soda-lime glass (adapted from [2])

In 1962, Charles and Hillig [37] first proposed a theory based on chemical reactions to explain the phenomenon of stress corrosion. Then, 20 years later, Michalske and Freiman [35], starting from the phenomenological model proposed by Charles and Hillig developed a detailed chemical model for the interaction of the environment with mechanically strained bonds in glass at the crack tip. The reaction involves three steps, as represented in Fig. 2.3a: (i) a water molecule from the environment approaches a bridging Si-O-Si bond at the crack tip, and forms an hydrogen bond with the oxygen atom belonging to the silica network (here indicated with O_{br}) while the lonepair orbitals from the oxygen of water (here indicated with O_w) interact with the Si atom; (ii) a proton transfer to O_{br} and an electron transfer from O_w to the Si atom occur with a concerted reaction, resulting in the destruction of the original bridging bond between O_{br} and Si, and in the formation of two new bonds: one between O_w and Si, and one between H and O_{br}; (iii) finally, the bond between O_w and transferred H breaks. As a result, surface hydroxyl groups are now present on each fracture surface. The chemical process is enhanced by the presence of alkali ions, like in the case of soda-lime silica glass [45]. In this case, the presence of terminal structures, in which sodium alkali ions are associated to the very strong Si-O-Si unending network through an oxygen–sodium ionic bond,

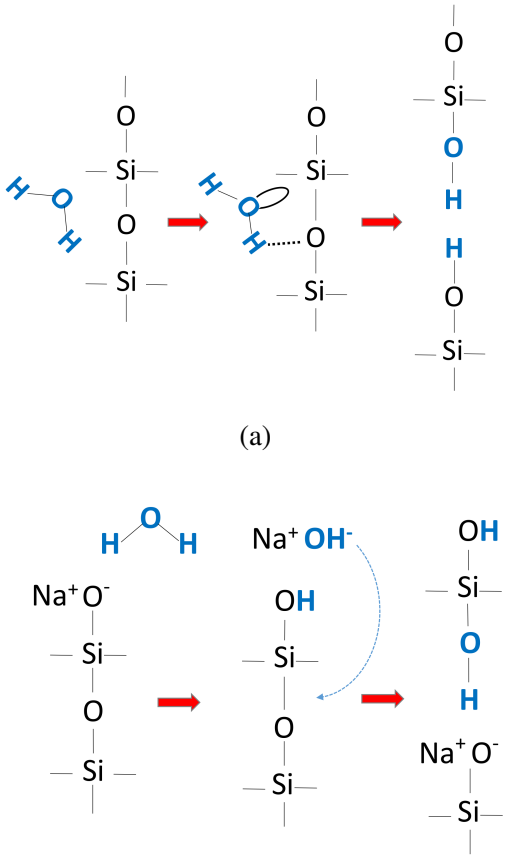

Fig. 2.3 Representation of the reaction between water and strained Si-O-Si bond at the crack tip: (a) silica glass; (b) soda-lime silica glass

strongly influences the reaction at the crack tip between soda-lime glass and water molecules. As a first step in fact, the oxygen–sodium bond breaks down, and the oxygen dissociates the water molecule to satisfy its force field with a hydrogen ion or a free hydroxyl ion. This facilitates the occurring of the second step, in which the strong bond between silicon and oxygen breaks, yielding two ends: one end becomes a silanol end by attachment of the hydroxide ion or by proton transfer while on the other end a new terminal structure is formed, capable of dissociating another water molecule (see Fig. 2.3b).

Stress corrosion, as any other chemical reaction, is an activated process. The activation energy is provided by mechanical stress and, therefore, the reaction occurs more rapidly where the stress field is the largest, i.e., at the tip of micro-cracks [35].

Different ways to overcome stress corrosion have been found; so far, the well-known solutions for glass strengthening are based on tempering processes, either through thermal or chemical treatments, which produces a surface compression state [38]. On the other hand, there are different issues with these technologies, such as high-energy costs and/or long treatment times [39]. Other solutions to such a problem proposed in the literature include: polymeric and metallic coatings for glass rods and silica lightguides [46–48], silicon grease for the edge strengthening of glass plates [49], and graphene coatings [50].

Protective polymeric coatings can be an effective alternative, since they have the advantage of limiting the intervention to the surfaces of glass plates while maintaining the transparency of the structural component. Moreover, coatings are routinely used in glass industry for many purposes; selective coatings to improve the thermal performance of glazing, anti-fingerprint coatings, and anti-shatter films are just a few examples [51]. In most cases, UV-cured coatings are preferred because they are environmentally friendly. They do not contain solvents and, therefore, toxic organic-vapor emissions are minimized. In addition, costs are reduced because the polymerization takes place in a few seconds and does not require heating. Typically, UV-cured coatings are made of acrylates, a class of polymers characterized by high reaction rate, stability, and high glass transition temperature, which makes them more resistant and suitable for outdoor applications [52]. However, they have poor adhesion and do not show water repellency, which are properties required for protecting glass from stress corrosion. The use of fluoropolymers is well known for water resistance and water repellency [53], while silanes can ensure adhesion, acting as a bridge and creating covalent bonds between the polymer and the glass surface [54, 55]. Preferably, a glass coating against stress corrosion must maximize adhesion on the glass side and hydrophobicity on the air side.

Therefore, in this work we examine a UV-curable acrylic system copolymerized with a methacrylic perfluoropolyether (PFPE) and an acrylic silane. The challenge was to obtain the best balance between hydrophobicity and adhesion of the coating, which are usually in competition. The composition of the coating was chosen with the aim of developing a copolymer exhibiting a compositional gradient, so that, the obtained coating ensured water repellency thanks to the surface segregation of the fluorinated component, and adhesion towards the glass substrate, thanks to the presence of the silane at the interface. Concerning the selection of the fluorinated co-monomer, attention was paid to the present constraints and regulations on the use of

this class of chemicals. In fact, fluoroalkylic chains of type C_nF_{2n+1} raise concerns for being toxic, persistently polluting the environment and bioaccumulating in humans. Short-chain fluorinated chains (i.e., shorter than C_4) and perfluoropolyethers are considered safe alternatives, approved by the U.S. Food & Drugs Administration (FDA) and the European Food Safety Authority (EFSA) [56, 57]. In this Chapter, the physical, chemical, and mechanical properties of the coating, including adhesive strength and water resistance, are investigated.

2.2 Materials and Methods

2.2.1 Materials

The chemical structures of the products used in this work are reported in Fig. 2.4.

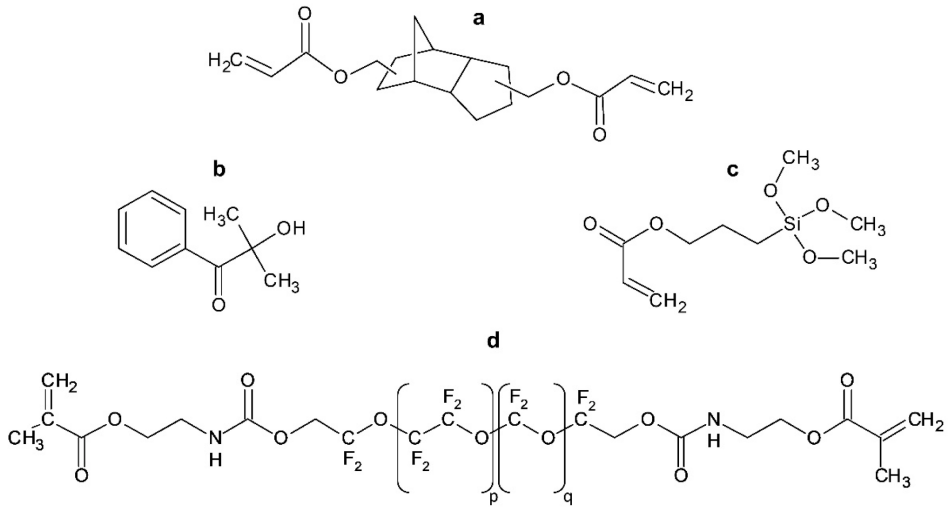

Fig. 2.4 Chemical structures of (a) Ebecryl® 130, (b) Darocur® 1173, (c) 3-(acryloyloxy) propyltrimethoxysilane and (d) Fluorolink® MD700

Tricyclodecanediol diacrylate (Ebecryl® 130, by Allnex Belgium SA, Drogenbos, Belgium) and a bifunctional urethane methacrylate perfluoropolyether (PFPE) macromer containing more than 80% of PFPE (Fluorolink® MD700, by Solvay Specialty Polymers, Bollate Milano, Italy) were used as oligomers, and will be called "E" and "F", respectively in what follows. 2-hydroxy 2-methyl 1-phenyl propan-1-one (Darocur® 1173, by BASF, Germany) was added as a photoinitiator,

henceforth indicated with "D". The silane was 3-(acryloyloxy) propyltrimethoxysilane, 94%, supplied by Alfa Aesar (Thermo Fisher (Kandel) GmbH, Karlsruhe, Germany). Thermo Scientific^{TM} British standard slides (referred to as glass slide in what follows) made from extra-white soda-lime glass, (Thermo Fisher Scientific Inc., Waltham, USA) were used as substrates for the coating characterization.

2.2.2 Silanization of glass slides

Silanization of glass with 3-(acryloyloxy) propyltrimethoxysilane was carried out following the procedure reported in Reference [58]. Glass substrates were surface modified by immersion in ethanol or water solutions of the silane. The concentration of silane was 0.2 vol% and 1 vol% in ethanol and 0.2 vol% in water. In the case of ethanol solutions, the glass slides were immersed in the solutions for 2 hours while they were heated to 70 °C and stirred with a magnetic mixer. The slides were then washed for 15 minutes in fresh ethanol in an ultrasonic bath to remove non-bound silane. In the case of water solution, the silanization was performed at room temperature by immersing the glass slides for 5 minutes; then the slides were rinsed with deionized water. For both water-based and ethanol-based silanization, treated slides and plates were dried in an oven at 115°C for 1h to promote silanol condensation.

For UV-curable coatings, the use of silane coupling agents is of particular interest. Silane coupling agents show two types of functionality: an organofunctional group R cable of co-reacting with the coating under irradiation and hydrolyzable groups X able to form chemical bonds with inorganic materials as glass. The general formula of the silane coupling agent is shown in Fig. 2.5.

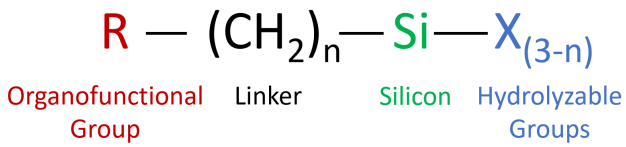

Fig. 2.5 General formula for silane coupling agent

The reaction between silane and glass in water solution results in the formation of covalent bonds between the glass substrate and the silane (see Fig. 2.6). The subsequent reaction between the R groups and the UV-curable resin forms durable

bridging bonds between glass and coating. Silane coupling agents chemically bond to substrates, that have hydroxyl end groups, by means of a reaction which develops over 4 main steps. The first phase involves the hydrolysis of the terminal groups, the hydrolysis is followed by the condensation reaction that takes place between two hydrolyzed silane molecules leading to the formation of siloxane groups and an oligomer. In the third step, the oligomer forms intermolecular hydrogen bonds with a hydroxyl terminal of the substrate. During the last step the hydrogen bond is replaced, with condensation, by a covalent bond, obtaining an oxygen bridge and the generated water escapes from the system. The final result of reacting an organosilane

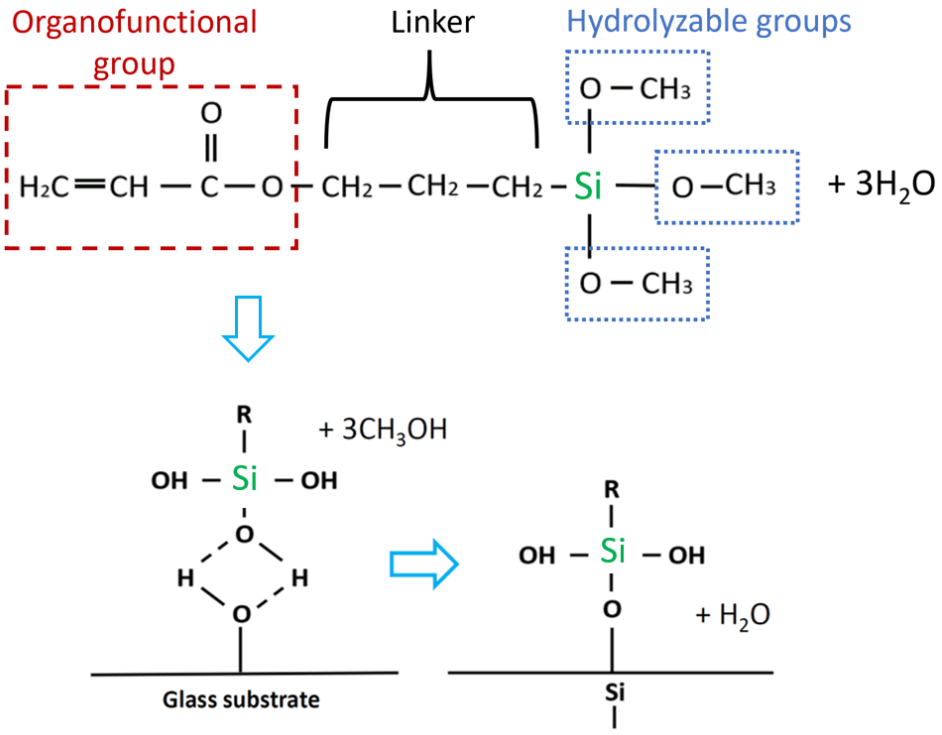

Fig. 2.6 Schematic representation of the deposition of silanes on substrate surfaces, adapted from [3]

with a substrate ranges from altering the wetting or adhesion characteristics of the substrate to ordering the interfacial region [3].

Table 2.1 Composition of the EFD coating

Product	Code	phr
Ebecryl® 130	E	100
Fluorolink® MD700	F	1
Darocur® 1173	D	3

2.2.3 Preparation of test specimens

The composition of the coating investigated in this work is summarized in Table 2.1. In the following, it is referred to as EFD, from the codes of its three constituents.

Reference coatings were made using 100 phr of Ebecryl® (E) or Fluorolink® (F) added with 3 phr of photoinitiator Darocur®: they are labelled ED and FD, respectively. For each characterization test, a specific protocol for the sample preparation was followed:

- Specimens for water contact angle, resistance to water and UV-visible spectroscopy: coatings with 50 µm thickness were prepared on the substrate of glass slides using a wire bar coater (Fig. 2.7). The thickness of the coating was verified for a few of specimens by means of an optical microscope. The constant value of the thickness of the coating is guaranteed by the use of a wire bar coater and a consolidated procedure for the specimen production. The wettability of the substrates was tested before use to check for the presence of contaminants.

- Specimens for single lap shear test: surface modified glass slides were used, with a circular bonding area having a diameter of 4 mm. The procedure sketched in Fig. 2.9 was adapted from Swentek and Wood [59]. A polytetrafluoroethylene (PTFE) mask (100 µm thick), slightly larger than the overlapped area of the two slides, was punched to obtain a circular hole; four perpendicular cuts were pre-made on the PTFE mask in order to ease removal after the curing. The mask was placed on one glass slide and the correct amount of resin was placed into the circular hole with a syringe, then a second glass slides was placed on top. The joint was then cured as described below, and the mask was removed by tearing it apart. Finally, the lap shear specimens were mounted in the tensile test set-up as shown in Fig. 2.10. Other glass slides were used as

spacers for the alignment of the specimens, both during assembly and in the dynamometer.

- Specimen for tensile test: resin specimens with formulations FD and ED were prepared with a rectangular cross-section in an open aluminum mold. The cross-section dimensions were 7.75×1.05 mm^2 for the FD resin, and 7.75×1.20 mm^2 for the ED resin (see Fig. 2.8).
- Specimens for water vapor permeability tests: a 100 µm wire bar coater was used to prepare the films.

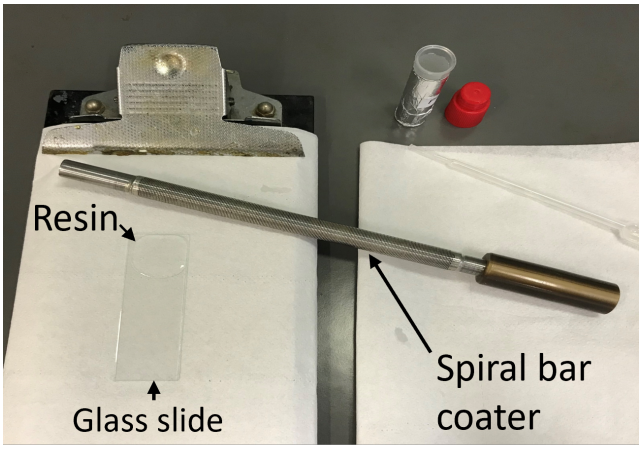

Fig. 2.7 Specimens preparation

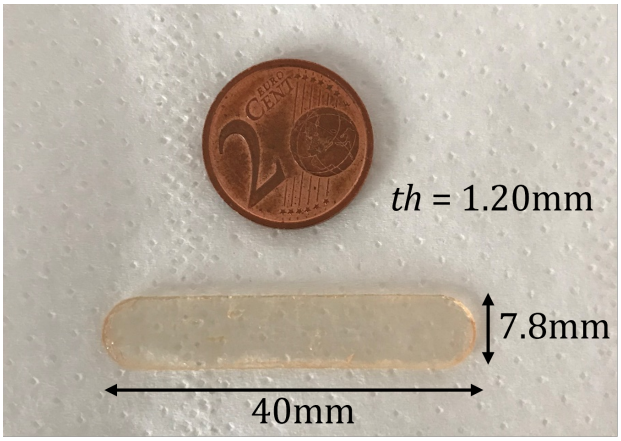

Fig. 2.8 Resin specimen used in the tensile test

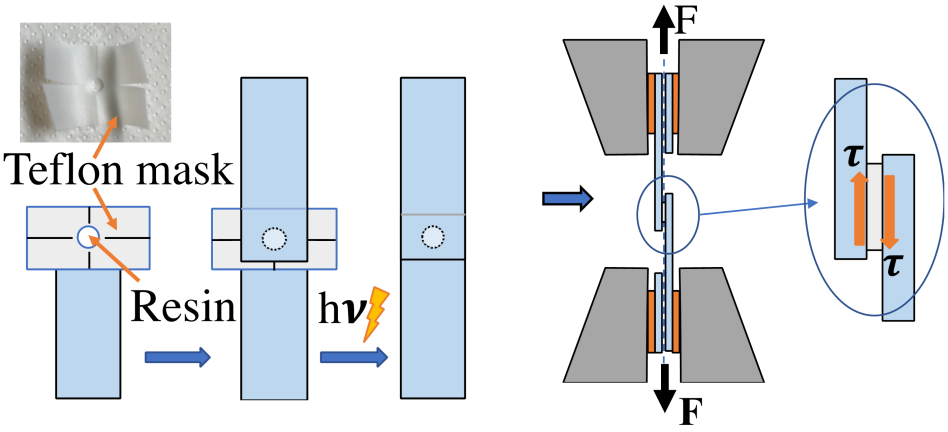

Fig. 2.9 Scheme of the preparation of the single lap shear specimen and scheme of the lap shear specimen mounted in the tensile test set-up

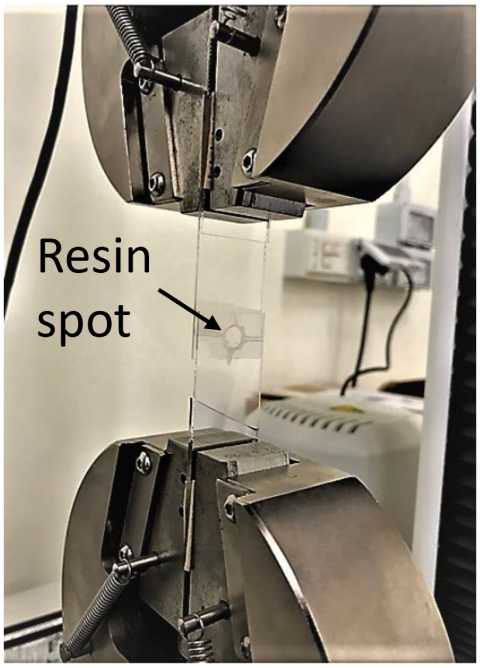

Fig. 2.10 Photo of the lap shear specimen mounted in the tensile test set-up

All types of specimens were cured with a 5000-EC UV flood lamp system (Dymax Corporation, Torrington, CT, USA) with medium intensity mercury bulb (Fig. 2.11). The intensity of the radiation was measured by means of a UV Power Puck II radiometer (EIT, LLC., Leesburg, USA) and was tuned by changing the distance between the specimens and the UV source. The coatings were cured with an intensity of 100 mW cm^{-2} for 2 min under N_2 flow, after 30 s of N_2 flow prior to curing. The lap shear specimens were cured at 100 mW cm^{-2} intensity in air for 3 min (1.5 min per side).

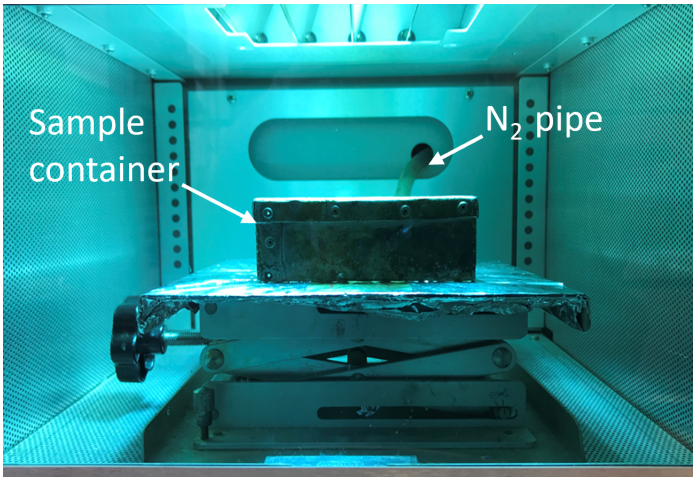

Fig. 2.11 UV curing system

2.2.4 Characterization methods

Static contact angle measurements were performed in order to assess the surface properties of both glass and EFD coating (Fig. 2.12). A Krüss DSA100 instrument (KRÜSS GmbH, Hamburg, Germany) was used, equipped with video camera and image analysis software, with the sessile drop technique. Water and hexadecane were the testing liquids and each measurement was repeated five times. Water and hexadecane drops were 10 µl and 5 µl, respectively. Contact angle measurements were used to estimate the surface energy of the coating, according to the geometric average model [60]:

$$(1+\cos\theta_i)\gamma_i = 2\left(\sqrt{\gamma_i^d\gamma_s^d}+\sqrt{\gamma_i^p\gamma_s^p}\right) \tag{2.1a}$$

$$\gamma_s = \gamma_s^d + \gamma_s^p \tag{2.1b}$$

where θ_i is the contact angle measured on the solid for the liquid i (water or hexadecane); γ_s, γ_s^d and γ_s^p, indicate the surface energy of the solid surface (polymer), and its dispersive and polar components, respectively. The surface energy values used for the calculations, embedded in the internal library of the FTA32 Software (First Ten Ångstroms,Portsmouth, VA, USA), are for water $\gamma_w = 72.8\,\mathrm{mN\,m^{-1}}$, $\gamma_w^d = 21.8\,\mathrm{mN\,m^{-1}}$, $\gamma_w^p = 51.0\,\mathrm{mN\,m^{-1}}$, and for hexadecane $\gamma_h = 28.1\,\mathrm{mN\,m^{-1}}$, $\gamma_h^d = 28.1\,\mathrm{mN\,m^{-1}}$, $\gamma_h^p = 0.0\,\mathrm{mN\,m^{-1}}$. Water contact angle analyses were repeated after the lap shear mechanical tests on the site of detachment of the joints. In this case, due to the small area of interest, only one measurement per sample was performed.

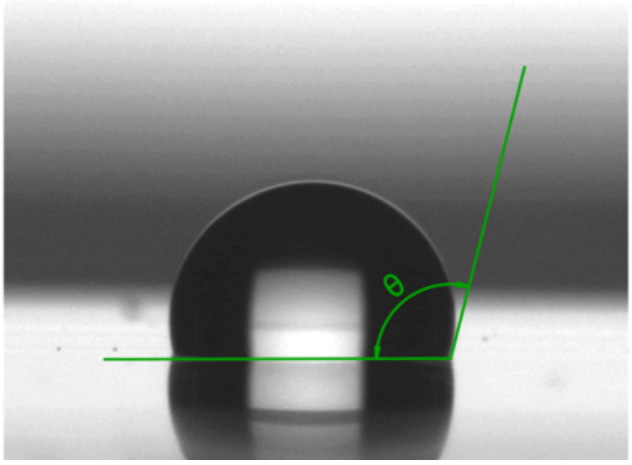

Fig. 2.12 Water drop on UV-cured coating

The surface roughness of bare and coated glass slides was assessed with a Surftest 201 series 178 portable measuring instrument (Mitutoyo Italiana S.r.L. Lainate (MI), Italy), according to DIN 4768 standard [61]. The sampling length was set at 0.8 mm and the evaluation length was taken as three times the sampling length; the arithmetic average roughness R_a, the mean roughness depth R_z, and the maximum roughness depth R_{max} were reported.

A JENWAY 6850 UV/Vis (Cole-Parmer, Stone, UK) UV-visible spectrophotometer was used to evaluate the transparency of the coatings; standard British glass slides were used as reference.

Resistance to water was assessed by immersion of the coated glass in demineralized water for 14 days at room temperature (RT), followed by 4 h at 60 °C. Daily inspections were performed according to the ASTM D870-15 (2015) standard [62].

Gloss values were measured with a ZGM 1020 glossmeter with a 60° angle (P. Zehtner Testing Instruments, Reigoldswil, Switzerland). A glass slide was taken as reference, and the relative change in gloss due to the coating was evaluated.

Single lap shear tests and tensile tests were performed by means of an Instron 3366 electromechanical universal testing machine (ITW Test and Measurement Italia S.r.l. Instron CEAST Division, Pianezza (TO), Italy) equipped with a 10 kN load cell. In order to perform the lap shear test, six specimens with formulation EFD were employed with a cross head speed of 5 mm/min; the adhesive strength of the joint, τ_{max}, was calculated as the ratio between the maximum load F_{max} obtained during the lap shear test and the initial bonded area, which was calculated from the diameter of the PTFE mask's circular hole. To perform the tensile test, three resin specimens were used for both ED and FD formulations.

A MultiPerm permeometer (ExtraSolution made by PermTech, Pieve Fosciana, Italy) was used to measure the Water Vapor Transmission Rate (WVTR). The test conditions were adapted from the ASTM F372-99 (2003) standard [63]; relative humidity was set at 80%. WVTR of each coating was evaluated as the average of three measures and compared to a standard 25 µm PET film, used as reference for barrier to water properties. All the specimens were subjected to a conditioning cycle to remove the residual humidity from the chambers and the films, bringing the system to the set temperature; the duration of conditioning cycle was 15 h. All the WVTR results were normalized to a thickness of 25 µm, according to Eq. (2.2):

$$\mathrm{WVTR}_{25} = \frac{\mathrm{WVTR}\, l}{25} \tag{2.2}$$

where l is the thickness of the film in µm. Specimen thickness was measured with a coating thickness gauge QuaNix 7500 (Automation USA, Westminster, USA). An optical microscope Olympus BX53M (Olympus Corp., Tokyo, Japan) was used to analyze the morphology of the films before and after permeability tests.

2.3 Results and discussion

2.3.1 Physical and chemical properties of the coating

In order to prevent stress corrosion of glass, a protective coating made with a cycloaliphatic acrylic resin copolymerized with a methacrylic perfluoropolyether (PFPE) and an acrylic silane primer, cured by UV-light, has been developed. The composition of the coating, referred to as EFD, is shown in Table 2.1

The wettability and the surface energy of the coating were estimated through water and hexadecane static contact angle measurements (see Eqs. (2.1a) and (2.1b)). The static contact angles values were 103.18° ± 1.58° and 52.10° ± 2.18° for water and hexadecane, respectively. The calculated surface energy was $\gamma_s = 19.18\,\mathrm{mN\,m^{-1}}$, with a polar component $\gamma_s^p = 1.36\,\mathrm{mN\,m^{-1}}$ and a dispersive component $\gamma_s^d = 17.92\,\mathrm{mN\,m^{-1}}$. This value is much lower than the coating without fluorinated co-monomer and similar to the pure PFPE [58]. The obtained results indicated and confirmed that the presence of PFPE monomer in a small amount (1 phr) ensures a strong surface modification, because it is able to migrate to the surface exposed to air, creating a compositional profile in the coating as discussed in a previous work [64].

The surface roughness, measured according to DIN 4768 [61], was similar for the bare glass slide and for the ED coating, while it was higher for the EFD coating. The FD coating could not be assessed as it was scratched by the stylus tip during the measurement. For the glass slide the values obtained were $R_a = 0.05 \pm 0.005\mu m$, $R_z = 0.3 \pm 0.05\mu m$, and $R_{max} = 0.3 \pm 0.05\mu m$; for the ED coating $Ra = 0.06 \pm 0.02\mu m$, $R_z = 0.3 \pm 0.05\mu m$, and $R_{max} = 0.3 \pm 0.1\mu m$; for the EFD coating $R_a = 0.21 \pm 0.08\mu m$, $R_z = 2.4 \pm 1.1\mu m$, and $R_{max} = 3.8 \pm 2.3\mu m$.

UV-visible analysis was done on the EFD coating in order to evaluate its transparency, which is relevant to preserve the properties of glass. The results are shown in Fig. 2.13, where they are compared to ED (formulation with only Ebecryl® 130 and Darocur® 1173) and FD (formulation with only Fluorolink® MD700 and Darocur® 1173) spectra taken from Reference [58]. The transmittance is higher than 80% in the visible range for all the formulations, which means that the transparency of glass is almost completely preserved.

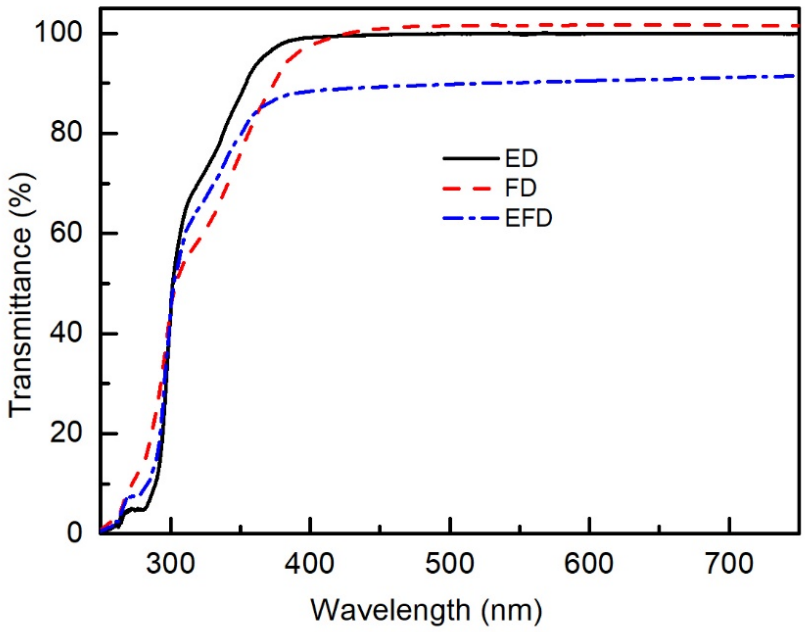

Fig. 2.13 UV-VIS spectra of ED, FD and EFD coatings

The gloss measurement revealed that when the ED coating was applied on the glass slides, the gloss increased by 5% with respect to the bare slide, while with the FD and EFD coatings it decreased by 22% and 20%, respectively. This again suggests that the surface of the coating is enriched in the PFPE monomer which is characterized by lower gloss values.

Barrier properties were assessed by $WVTR_{25}$ tests (as defined in Section 2.2.4), performed on the UV-cured films and the results were compared to a polyethylene (PET) film which showed $WVTR_{25} = 22.4 \pm 0.45\,g/(m^2\,24h)$. The $WVTR_{25}$ results are presented in Table 2.2. The coating made only of PFPE (FD) was very leaky; whereas the results of ED and EFD coatings were similar. Therefore, it was proven that the permeability to water of the coating is not affected by the presence of a small amount of fluorinated component. The WVTR25 of the EFD film was of the same order of magnitude as the PET, showing acceptable barrier to water properties.

Before and after the permeability measurements, the films morphology was observed with an optical microscope in order to find possible evidence of degradation due to the exposure to water vapor. A magnification of the EFD and FD film surfaces after the permeability tests is shown in Fig. 2.14: the EFD film did not show

Table 2.2 Barrier to water results

Composition	$WVTR_{25}$ $g/(m^2\,24h)$
EFD	87.1 ± 15.8
ED	53.1 ± 7.76
FD	316 ± 20.2

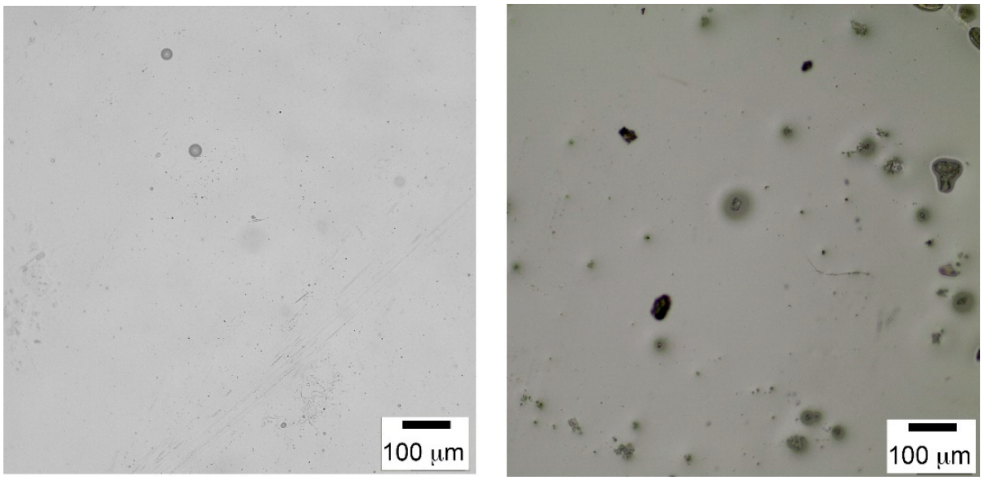

(a) (b)

Fig. 2.14 Surface of EFD (a) and FD (b) coatings after permeability test

significant damage, while on the FD surface several pinholes were visible. The presence of pinholes in the coating is consistent with the high value of $WVTR_{25}$ obtained.

2.3.2 Mechanical properties of the coating: adhesive and tensile strength

The adhesion properties between the photopolymerized EFD coating and glass were studied. In order to improve the adhesion between the glass substrate and the coating, a silane coupling agent was used to functionalize the glass surface. A silane with an acrylic functional group was chosen, so that it can co-react with UV-cured coating creating covalent bond. Different concentration of silane in different solvents were tested in order to select the most economic and environmentally friendly solution in view of a commercial application. Water contact angle was performed on

Table 2.3 Results of immersion test of coated glass with different silanization conditions

Glass surface treatment	Coating failure
None	1 day
Silanization 0.2 vol.% in ethanol	No
Silanization 1 vol.% in ethanol	No
Silanization 0.2 vol.% in water	No

untreated and silanized glass, as the successful modification of the glass surfaces is expected to significantly modify the surface hydrophilic character [65]. As expected, the value obtained on the untreated glass slides was lower than 10°, confirming the full wettability of the raw substrates. The surface functionalization of glass with the silane increased the θ_w in all the tested conditions. Similar results were obtained with 1 vol.% silane in ethanol ($\theta_w = 69.4° \pm 3.1°$) and 0.2 vol.% silane in water ($\theta_w = 67.6° \pm 4.1°$). With 0.2 vol.% in ethanol the contact angle was lower ($\theta_w = 56.6° \pm 3.0°$); therefore the silanization process in water was more efficient, which is relevant for economic and environmental sustainability reasons.

A preliminary assessment of adhesion was performed checking the resistance upon immersion in water. The coating was cured on untreated and silanized glass. Tab. 2.3 shows the results obtained after 14 days of immersion in water at Room Temperature (RT) followed by 4 h of immersion at 60°C: in the "Coating failure" column the time elapsed before the detachment of the coating from the glass substrate is reported. The coating detached from the untreated glass after 1 day at RT, whereas all systems with treated substrates survived the entire immersion test, confirming the effectiveness of the surface silanization in the improvement of adhesion and water resistance.

Single lap shear tests (for which the geometry of the specimens and the set up are described in Section 2.2.4) were performed on EFD joints on silanized glass slides, as shown in Figs. 2.9 and 2.10 . The shear stress vs. displacement curves are reported in Fig. 2.15 and the obtained average τ_{max} is reported in Table 2.4, together with the data regarding the inspection of the joints after failure. In the table are also reported the data obtained for FD and ED, taken from Reference [58]. The average value of τ_{max} obtained for EFD specimens was 24.9 ± 2.8 MPa, which proved a good adhesion between the glass substrate and the photopolymerized formulation. It is worth noticing that the adopted single lap shear set-up (see Fig. 2.9) does not provide

only shear stress, but also additional moment, geometrical singularities, and material singularities. As a consequence, the actual adhesive strength has to be greater than the evaluated one. Furthermore, it is important to remark that the result refers to the air side of the glass.

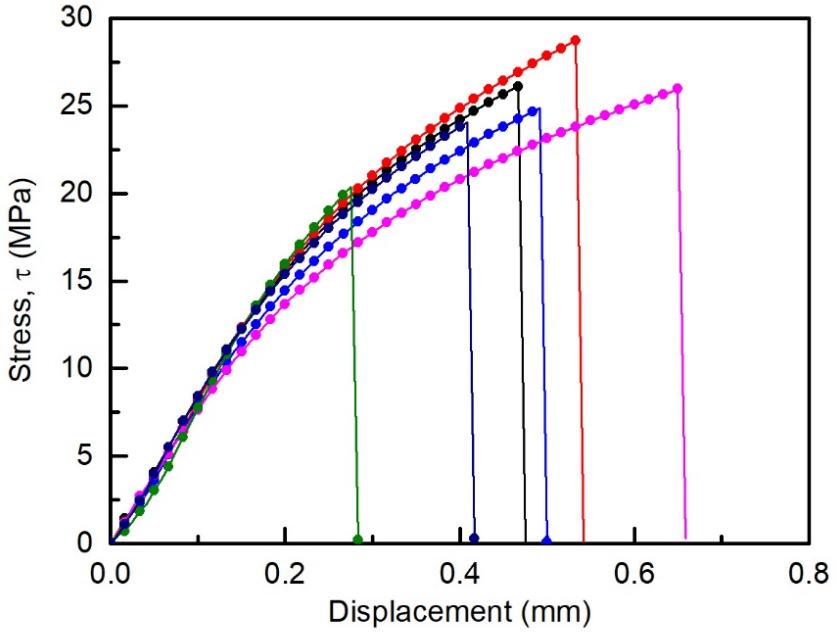

Fig. 2.15 Stress-displacement curves obtained in the lap shear test for EFD joints on silanized glass

In absence of silanization it was not possible to perform the single lap shear test because the adhesion was so poor that the glass slides detached during the preparation of the specimens. The values of τ_{max} are very similar for ED and EFD, while the reported τ_{max} for FD specimens is lower: the results proved that the small amount of fluorinated component does not affect the adhesion properties of the coating, assuming that the PFPE chains migrate far from the glass surfaces. For all the specimens the joint failed leaving the entire polymer disk on one side of the joint. The sites of the glass slides where the joint detached (detachment sites) were inspected with water contact angle measurements. For the ED and EFD joints the water contact angle measurements gave similar results, and the measured value confirmed that the glass surfaces were still silanized. For the FD joints, the contact angle value was higher, which probably indicated a residual presence of the polymer.

Table 2.4 Results of the lap shear test: τ_{max} is the shear strength, θ_w is the water contact angle measured on the glass surface at the joint detachment site right after the lap-shear test, $\theta_w^{'}$ is the water contact angle measured on the detachment site after rinsing

	EFD	ED	FD
τ_{max} (MPa)	24.9 ± 2.8	24.5 ± 2.8	5.8 ± 1.0
θ_w (°)	68.4 ± 2.5	61.5 ± 2.6	75.1 ± 2.5
$\theta_w^{'}$ (°)	65.8 ± 2.8	60.8 ± 2.4	72.6 ± 4.3

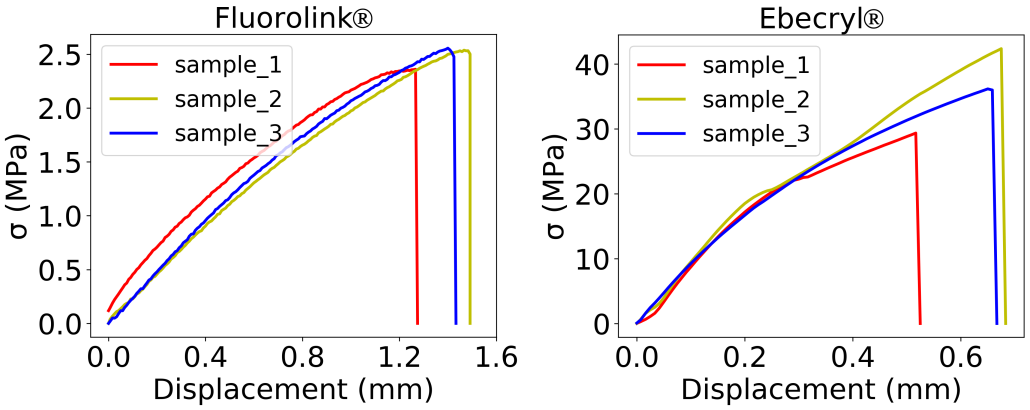

(a) (b)

Fig. 2.16 Tensile test results for (a) the FD formulation and (b) the ED formulation

Tensile tests were performed on the FD and ED specimens of Fig. 2.8. The stress-displacement curves of the cured FD and ED specimens are reported in Fig. 2.16. Both resins showed a brittle rupture under the experimental conditions applied. However, the average tensile strength of the FD specimens was $\sigma_{\mathrm{FD},max} = 2.48$MPa, that is one order of magnitude lower than that of the ED specimens $\sigma_{\mathrm{ED},max} = 35.98$MPa .

2.4 Conclusions

The EFD coating was prepared with a co-reactive silane primer, a cycloaliphatic UV-curable resin, a fluorinated methacrylate co-monomer, showing good barrier to water vapor, hydrophobicity, transparency and adhesion properties. Good adhesion and high water repellency were present at the same time thanks to a compositional gradient. The hydrophobic behavior was due to the presence of a low amount (1 phr)

of the fluorinated co-monomer which was selectively enriching the outer surface of the coating. The adhesion was due to the covalent bonding between the silane layer and the coating itself. The obtained results are very promising in terms of water repellency, permeability and adhesion to glass, however, the coating's effectiveness in preventing stress corrosion has yet to be proven.

A wide experimental investigation was carried out and it will be presented in Chapter 3 to investigate the effectiveness of the coating in glass stress corrosion prevention on different kinds of glass, including also aged glass. Moreover, the coating durability is an issue that will be tackled in Chapter 4. In this context, the durability of the coating against mechanical ageing, natural and artificial weathering will be considered by exposing coated specimens to cyclic loads, UV radiation, heat and water.

Chapter 3

Assessment of the effectiveness of the coating for new and aged glass[1]

3.1 Introduction

A polymeric coating was prepared using an UV-curable formulation, based on a hydrocarbon acrylic resin (Ebecryl® 130, by Allnex Belgium SA, Drogenbos, Belgium) and a photoinitiator (Darocur® 1173, by BASF, Germany), added with a small amount (1 phr) of a fluorinated methacrylate (Fluorolink® MD700, by Solvay Specialty Polymers, Bollate Milano, Italy). The formulation, whose details can be found in Chapter 2, was coated on glass, previously treated with a silane primer containing an acrylic group (3-(acryloyloxy) propyltrimethoxysilane, Alfa Aesar by Thermo Fisher (Kandel) GmbH, Karlsruhe, Germany). The primer modifies the glass surface by reaction with the silanol groups, while through the acrylic functions it co-reacts with the (meth)acrylic resins upon UV irradiation. Forming covalent bonds between the soda-lime glass and the coating, it increases the adhesion strength. In the case discussed in this Chapter, the silylation of the glass was performed by immersing the specimens in solutions of the silane in water (0.2 vol%) for 5 min at room temperature, rinsing them with de-ionized water and drying them in an oven at 100 °C for 30 min to facilitate silanol condensation. The coating was spread on the glass surface by a wire wound bar, and cured by UV irradiation, according to the

[1]Part of the work described has been previously published in:
G. Mariggiò, S. Dalle Vacche, R. Bongiovanni, C. Louter, M. Corrado. Enhancing the design bending strength of new and aged glass with a functional coating. Glass Struct. Eng. 5, 135–146 (2020).

procedure reported in Chapter 2. After irradiation a transparent solid film, with a thickness of 50 µm, as revealed by inspection with an optical microscope and shown in Fig. 3.1, was obtained. The thickness of the coating was verified for a few of specimens, its constant value is guaranteed by the use of a wire bar coater and a consolidated procedure for the specimen production.

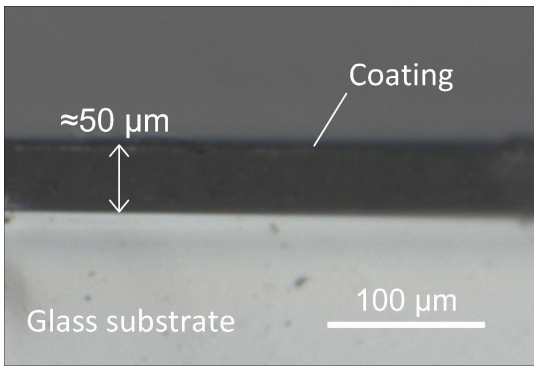

Fig. 3.1 Cured coating on the glass substrate

The formulation here described was chosen to provide a compositionally graded coating able to ensure within one layer good barrier to water vapor, hydrophobicity, transparency and adhesion properties, as needed for hindering the stress corrosion of glass. The hydrocarbon resin is transparent and has acceptably low water vapour transmission rate ($WVTR_{25}$), however it is not water repellent, as shown by the water contact angle θ_{water} which is lower than 90°. The fluorinated resin has high water repellency (water contact angle θ_{water} higher than 90°), but has high permeability, and shows poor adhesion strength (τ). The properties of the resins and of the compositionally graded coating were studied in Chapter 2, and are summarized in Table 3.1 for convenience.

Table 3.1 Properties of the coating and of its components

Composition	$WVTR_{25}$ ($g/m^2/24h$)	θ_{water} (°)	Adhesion strength τ (MPa)
Compositionally graded coating	87.1 ± 15.8	103.2 ± 1.6	24.9 ± 2.8
Hydrocarbon acrylate resin	53.1 ± 7.8	67.6 ± 4.1	24.5 ± 2.8
Fluorinated methacrylate	316.0 ± 20.2	102.9 ± 2.6	5.8 ± 1.0

As discussed in Ref. [53, 66, 67], adding a small amount of a fluorinated resin to a hydrocarbon resin results in a compositional gradient as sketched in Fig. 3.2: due

to the difference in polarity between the two resins, the fluorinated one selectively migrates to the air surface and is not present at the glass interface. This gradient becomes irreversible after curing under UV light the latter. Therefore, the coating shows the water repellency of the fluorinated component, although it is present at low concentration; the adhesion and water vapour transmission rate are not affected as these properties are imparted by the hydrocarbon resin covalently linked to the silane primer at the glass interface.

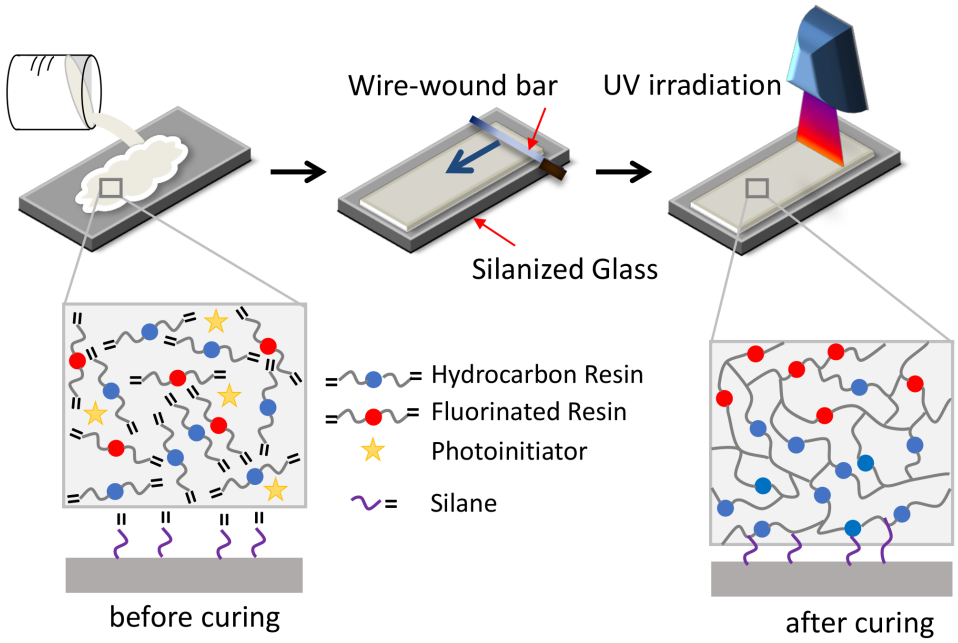

Fig. 3.2 Schematic representation of the compositionally graded coating

3.2 Experimental protocol

3.2.1 Coaxial double ring test

The effectiveness of the coating in protecting glass surfaces against stress corrosion was assessed experimentally by comparing the load-carrying capacity of coated and un-coated specimens. Equibiaxial bending tests were carried out with a coaxial double ring setup having the supporting ring with diameter $D_S = 90$ mm and the

loading ring with diameter $D_L = 40$ mm (see Figs. 3.3 and 3.4). Square glass samples were tested, with nominal thickness $h = 4$ mm and edge size $l = 120$ mm (see Fig. 3.4). The actual thickness of the samples was measured for all glass typologies involved in this study, its value approached 4 mm and remained almost constant for all glass samples. The dimensions of the testing rig and the samples, and their ratios were designed according to the prescriptions provided by the ASTM C1499-19 [68] Standard, in line with a number of similar experiments recently carried out to investigate the bending strength of glass ([18, 16, 69]). A servo-hydraulic MTS universal testing machine was used, with a load cell capacity of 10 kN. The loading ring was connected to the testing machine with an articulated joint to ensure uniform contact between the loading ring and the surface of the specimen.

Four typologies of glass samples were tested: (*i*) new un-coated glass samples (NU), (*ii*) new coated glass samples (NC), (*iii*) naturally aged un-coated glass samples (AU), (*iv*) naturally aged coated glass samples (AC). Sets of 25 and 20 specimens were tested for un-coated and coated glass, respectively. To ensure constant and harsh environmental conditions for stress corrosion, the supporting ring and the specimens were inserted in a watertight container filled with water, for the entire duration of the test (see Fig. 3.3b).

Both new and aged glasses were soda-lime glass, as proven by the FTIR-ATR (Fourier Transform InfraRed-Attenuated Total Reflection) spectroscopy carried out on selected samples and shown in Fig. 3.5. Peaks of the absorbance at $910\,\mathrm{cm}^{-1}$ and $768\,\mathrm{cm}^{-1}$ are representative of the symmetric and asymmetric vibration of the Si-O-Si bond [70]. The IR spectra of the new and aged glasses used in this study are compared to that of a microscope slide made of low-iron soda-lime glass. All the three spectra shown in Fig. 3.5 are perfectly overlapped.

Concerning the ageing conditions of the naturally aged glass samples, they were cut from glass panes of single glazing windows obtained from refurbishment works of a low-rise building located in Torino, Italy. Their service life was between 25 and 30 years. Inspection by means of an optical microscope showed no differences between the two faces of the aged glasses in terms of size and shape of flaws and scratches. Since the adhesion property of the coating was assessed for the air side of the glass (see Section 2.3.2), we chose to test the side exposed to air during the production of the glass panes, in accordance with the criterion adopted for the new glass specimens. Consistently, the coating was applied on the air side in all the cases,

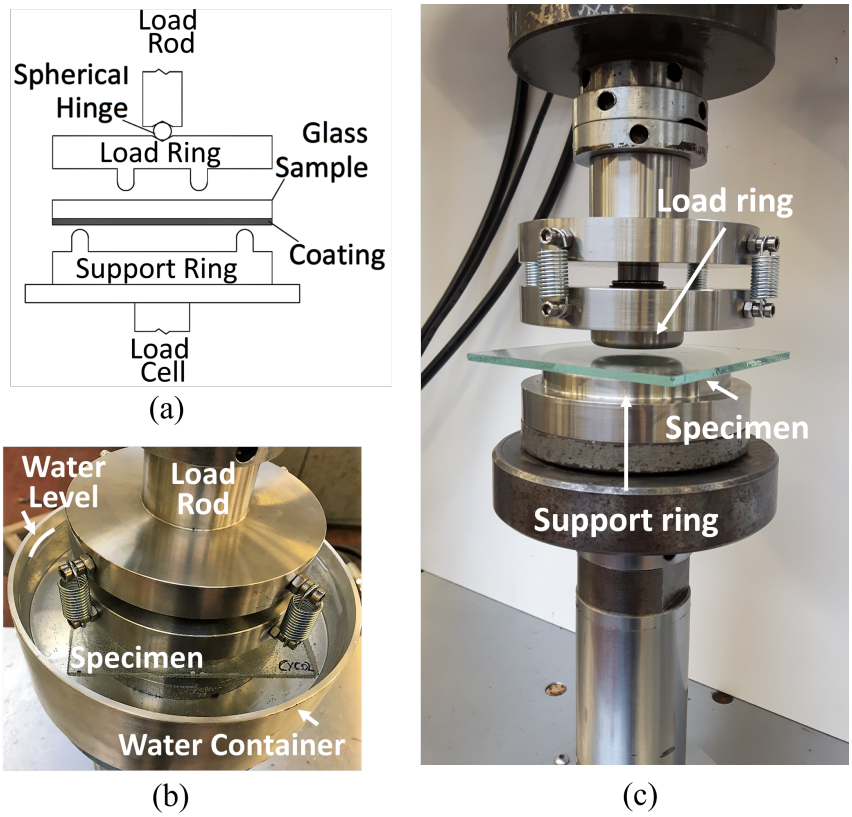

Fig. 3.3 Coaxial double ring set-up: (a) sketch; (b) detail of the water container; (c) global picture of the test rig

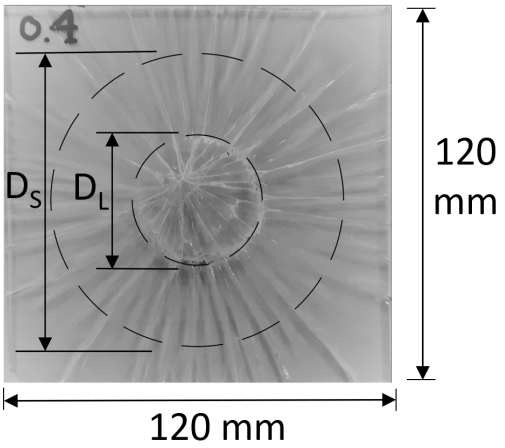

Fig. 3.4 Glass specimen geometry

while a self-adhesive film was applied on the tin side in order to hold the fragments together after breaking of the specimen.

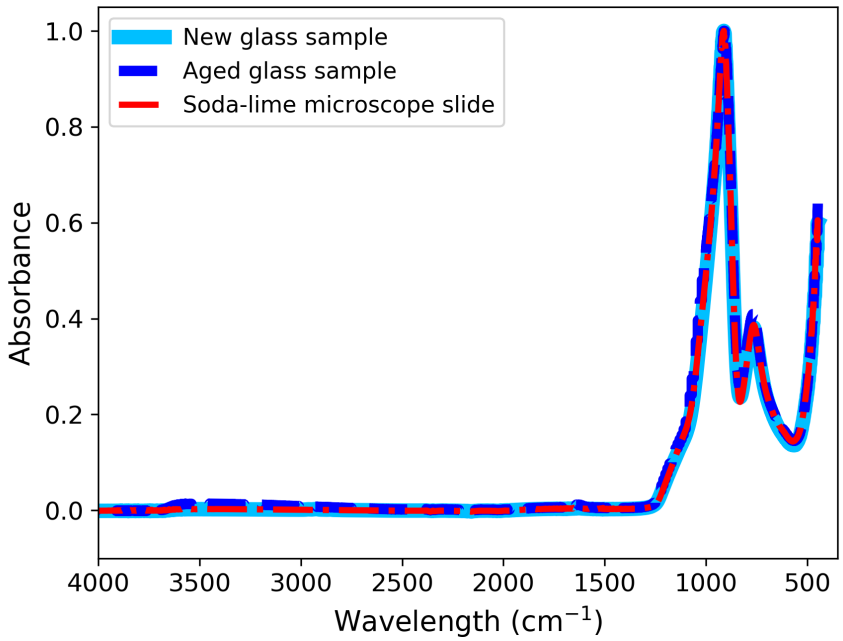

Fig. 3.5 FTIR-ATR spectra of new and aged glasses, compared to that of a reference soda-lime glass

The loading tests were carried out under displacement control. Two series of tests were carried out on the un-coated specimens: one with a low displacement rate, equal to 0.7 µm/s, which corresponds to a stress rate of 0.15 MPa/s, and the other one with a high displacement rate, equal to 14.0 µm/s, which corresponds to a stress rate of 3.0 MPa/s. The low rate caused fracture of the samples within 600-900 s, whereas the high rate within 30-50 s. Therefore, the specimens tested at the high displacement rate are only slightly affected by stress corrosion, as reported in the literature [49], while remaining in the quasi-static regime. It is worth noting that the effects of stress corrosion are negligible only with higher stress rates, which approach the dynamic regime [26]. The stress rate equal to 3.0 MPa/s was used in place of 2.0 MPa/s, which is the stress rate advised by European standards (see e.g. [71]), in order to further limit the test time and, consequently, the effect of stress corrosion. The coated specimens were tested only at the low displacement rate.

The equibiaxial strength, σ_f, was calculated from the failure load, F, by means of the following equation, provided by ASTM C1499-19 [68]:

$$\sigma_f = \frac{3F}{2\pi h^2}\left[(1-\nu)\frac{D_S^2 - D_L^2}{2D^2} + (1+\nu)ln\frac{D_S}{D_L}\right] \tag{3.1}$$

where: F is the failure load, h is the nominal thickness of the specimen, D_S and D_L are the diameters of the supporting and loading rings, respectively, D is the diameter of the glass specimen, and $\nu = 0.22$ is the Poisson's ratio of glass. For a rectangular test specimen, D is the diameter of a circle that expresses the characteristic size of the plate as follows:

$$D = \frac{l}{0.90961 + 0.12652\frac{h}{D_S}0.00168ln\frac{l - D_S}{h}} \tag{3.2}$$

where:

$$l = 0.5(l_1 + l_2) \tag{3.3}$$

and l_1 and l_2 are the lengths of the edges.

3.2.2 Statistical analysis of strength data

The Weibull distribution is traditionally thought to be the best method for statistically characterizing the strength of brittle materials [72]. In particular, the glass strength distribution, σ_f, can be represented by a two parameter Weibull distribution function (see Fig. 3.6a):

$$P_f = 1 - \exp\left[-\left(\frac{\sigma_f}{\theta}\right)^{\beta}\right] \tag{3.4}$$

where P_f is the cumulative distribution function of failure, and β and θ are the Weibull shape and scale parameters, obtained by the best-fitting of experimental data.

The Weibull distribution function can be linearized by taking the logarithm twice (see Fig. 3.6b):

$$\ln\left(\ln\left(\frac{1}{1-P_f}\right)\right) = \beta\ln(\sigma_f) - \beta\ln(\theta) \tag{3.5}$$

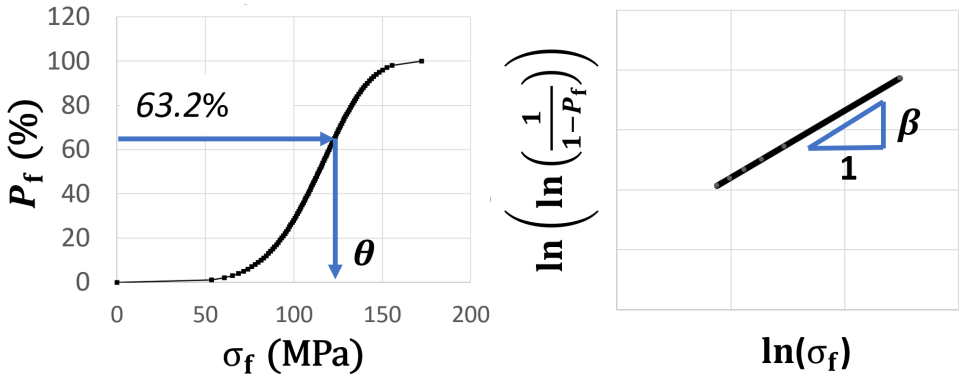

(a) (b)

Fig. 3.6 (a) Weibull cumulative distribution function; (b) Linearised Weibull cumulative distribution function

According to EN 12603 [73], β and θ parameters were calculated with the good linear unbiased estimators method:

$$\hat{\beta} = \frac{nk_{\mathrm{n}}}{\frac{s}{n-s}\sum_{i=s+1}^{n} \ln\sigma_i - \sum_{i=1}^{s} \ln\sigma_i} \tag{3.6}$$

$$\hat{\theta} = \exp\left[\frac{1}{n}\sum_{i=1}^{n} \ln\sigma_i + 0.5772\frac{1}{\hat{\beta}}\right] \tag{3.7}$$

where: n is the sample size, s is the largest integer less than $0.84n$, and the values of k_n, estimated as a function of the sample size n, are listed in Table 3 of EN 12603 [73].

Strength data, σ_{f}, were ranked in ascending order (i = 1 to n) to build an Ordered Sample. Then, a probability of failure was assigned to each value σ_i of the Ordered Sample by means of probability estimators $\hat{G}_i$:

$$\hat{G}_i = \frac{i-0.3}{n+0.4} \tag{3.8}$$

Finally, each point (σ_{f}, $\hat{G}_i$) was plotted into the Weibull diagram, which relates the probability of failure (%) to the failure stress (MPa).

3.3 Results and discussion

3.3.1 Experimental results

The experimental bending strength values σ_f are listed in ascending order in Table 3.2 for all the types of glass samples: (*i*) new un-coated glass samples tested at low stress rate (0.15 MPa/s) (NU low rate), (*ii*) new un-coated glass samples tested at high stress rate (3.0 MPa/s) (NU high rate), (*iii*) new coated glass samples tested at low stress rate (NC low rate), (*iv*) naturally aged un-coated glass samples tested at low stress rate (AU low rate), (*v*) naturally aged un-coated glass samples tested at high stress rate (AU high rate), and (*vi*) naturally aged coated glass samples tested at low stress rate (AC low rate).

3.3.2 Weibull analysis of the glass bending strength

The Weibull diagrams for new and aged un-coated specimens tested at low stress rate (0.15 MPa/s) are shown in Fig. 3.7. Both sets of data are well fitted by a straight line, proving that they can be appropriately interpreted with the Weibull statistics. The curve that best fit the data points of AU specimens (rhombus markers) is characterized by $\hat{\beta} = 5.25$ and $\hat{\theta} = 46.83$ MPa, while that for NU specimens (square markers) has $\hat{\beta} = 5.16$ and $\hat{\theta} = 68.25$ MPa. As expected, the parameter $\hat{\beta}$, which represents the slope of the linearised Weibull diagram and therefore is indicative of the strength scatter, is almost the same for new and aged glass. The obtained values are within the range of values reported in the literature for flat glass, namely 3–7 [74]). On the contrary, the parameter $\hat{\theta}$, which is the bending strength associated to a probability of failure of 63.2%, is lower in the case of aged glass, because of the presence of larger surface defects. Graphically, the increase of strength is represented by a shift of the curve towards higher values of failure stress.

The Weibull diagrams for new un-coated specimens tested at low and high stress rates, and for new coated specimens tested at low stress rate are shown in Fig. 3.8. Again, all the three sets of data are well fitted by the Weibull distribution function. The increase of the imposed stress rate reduces the effect of the stress corrosion, thus leading to a shift of the data points toward higher values of strength (triangles). Such a strengthening effect can be clearly quantified by the parameter $\hat{\theta}$, which increases from 68.25 MPa to 85.34 MPa. The effectiveness of the developed coating

Table 3.2 Strength data σ_f in MPa for each type of glass

Specimen	NU low rate	NU high rate	NC low rate	AU low rate	AU high rate	AC low rate
1	30.66	46.25	75.59	25.67	37.42	35.69
2	35.32	54.30	83.80	31.21	46.99	37.56
3	40.34	55.62	93.99	32.02	48.35	62.62
4	44.65	57.83	96.03	34.33	48.89	66.45
5	46.32	63.63	100.27	34.70	48.99	70.63
6	55.93	65.03	102.58	37.86	50.08	73.21
7	56.64	69.10	106.96	38.03	51.71	81.53
8	58.03	69.17	108.42	38.13	52.46	84.01
9	59.70	70.63	109.24	39.08	53.37	87.0
10	62.51	71.75	109.99	39.32	53.88	88.29
11	63.87	74.20	114.91	40.51	55.34	93.79
12	64.14	77.35	117.93	40.58	58.09	94.26
13	68.18	78.64	119.26	41.80	59.79	101.02
14	70.77	84.38	129.03	43.57	59.96	103.33
15	71.0	86.66	136.27	43.94	64.61	109.44
16	72.97	88.25	143.02	45.54	71.74	112.97
17	73.58	89.88	148.70	45.98	72.73	114.67
18	73.75	91.17	-	46.86	78.67	115.42
19	77.52	92.12	-	46.89	82.20	-
20	78.03	93.99	-	47.57	84.68	-
21	78.75	94.23	-	50.80	85.09	-
22	83.67	97.01	-	51.55	86.49	-
23	84.96	98.23	-	54.36	88.49	-
24	-	100.51	-	56.47	91.27	-
25	-	105.44	-	62.11	91.82	-

in preventing stress corrosion is evident from the results shown in Fig. 3.8. The set of points representing the probability of failure of NC specimens at low stress rate (circles) is the most shifted rightwards, being characterized by $\hat{\theta} = 121.83$ MPa. The parameter $\hat{\beta}$ has very similar values in the three cases. In the same diagram a horizontal dashed line is drawn to indicate the probability $P_f = 0.8\%$, which corresponds to a commonly used probability of failure for glass design [75] and adopted by the American National Standard 'Standard Practice for Determining Load Resistance of Glass in Buildings' ASTM E1300-16 [5]. The selection of the design probability of failure intends to quantify the performance improvement of coated glass compared to uncoated glass, rather than define a specific design glass strength for all the glass typologies tested. Therefore, probability of failure

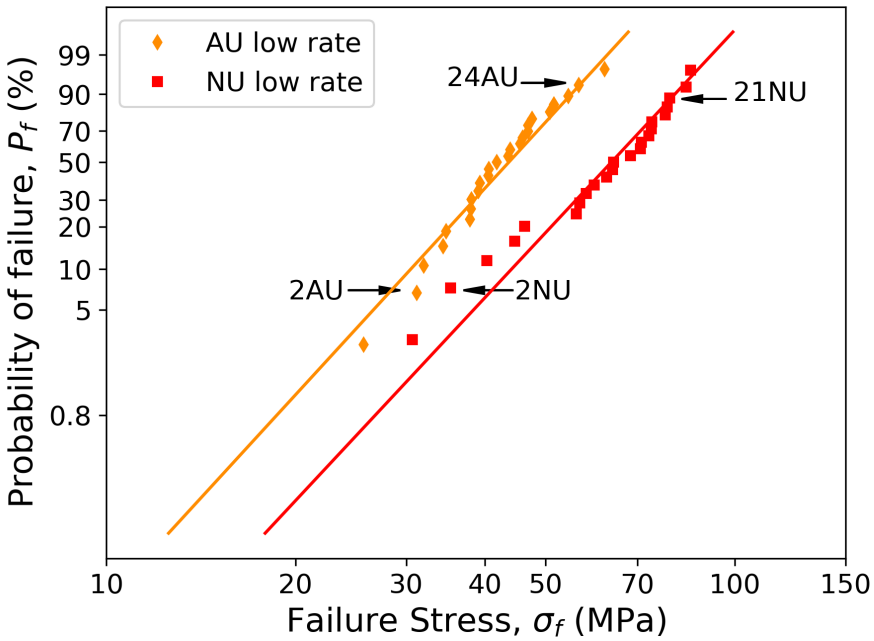

Fig. 3.7 Weibull distribution function of the probability of failure for new (NU) and naturally aged (AU) un-coated glass samples tested at low stress rate. The specimens subjected to microscopy inspection after the test are identified by a label

lower than 0.8 % could be also selected by aiming to compare the performance of coated and uncoated glass. By extrapolating the experimental data points through the best fitting Weibull distribution functions, the following design bending strengths are obtained: 26.8 MPa for NU low rate specimens, 37.3 MPa for NU high rate specimens, and 51.4 MPa for NC specimens. Therefore, we can conclude that the coating allows to increase of about 92% the design bending strength.

Very similar results were obtained in the case of naturally aged glass specimens. The Weibull diagrams for aged un-coated specimens tested at low and high stress rates, and for aged coated specimens tested at low stress rate are shown in Fig. 3.9. The data points referred to AU low rate and AC sets of specimens are well approximated by the Weibull distribution, except for two points of the set AC, which are out of trend, whereas the results of the set AU high rate are more departed from the straight line representative of the Weibull distribution. As obtained in the case of new glass specimens, the un-coated aged glass tested at low stress rate exhibited the lowest strength, $\hat{\theta} = 46.83$ MPa, followed by the un-coated aged glass tested at

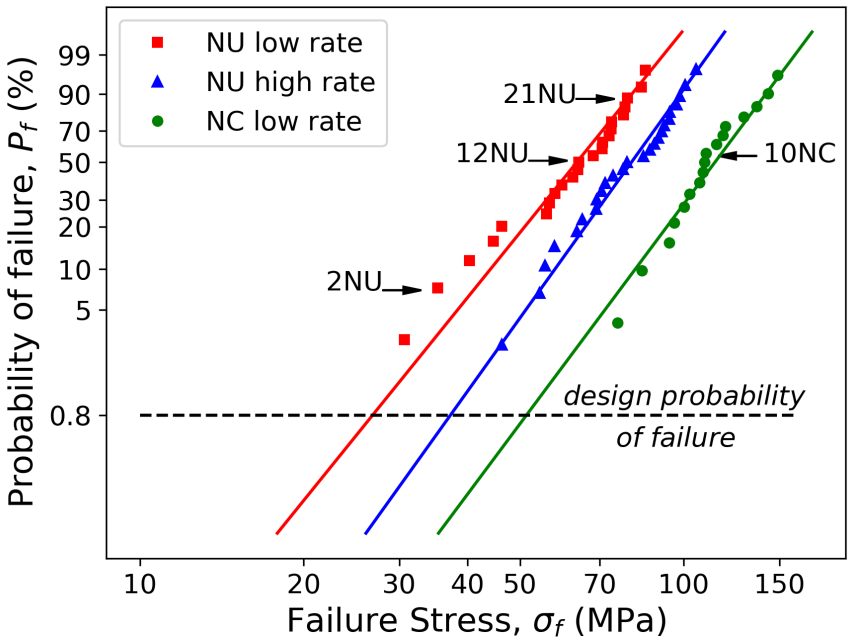

Fig. 3.8 Weibull distribution function of the probability of failure for coated (NC) and un-coated (NU) new glass samples. The specimens subjected to microscopy inspection after the test are identified by a label

high stress rate, $\hat{\theta} = 71.95$ MPa, and the coated specimens, $\hat{\theta} = 92.71$ MPa. With reference to the design probability of failure of 0.8%, the application of the coating to aged glass leads to an increase of the design bending strength of about 62%, being the design strength of coated glass equal to 30.2 MPa, and that of un-coated glass equal to 18.7 MPa.

All the results of the statistical analysis carried out on the experimental data are summarized in Tab. 3.3. They include, for each series of tests, the number of specimens that failed in an acceptable way, the Weibull shape parameter $\hat{\beta}$, the Weibull scale parameter $\hat{\theta}$, the coefficient of variation $\hat{CV}$, and the design bending strength $\hat{\sigma}_{f,0.008}$.

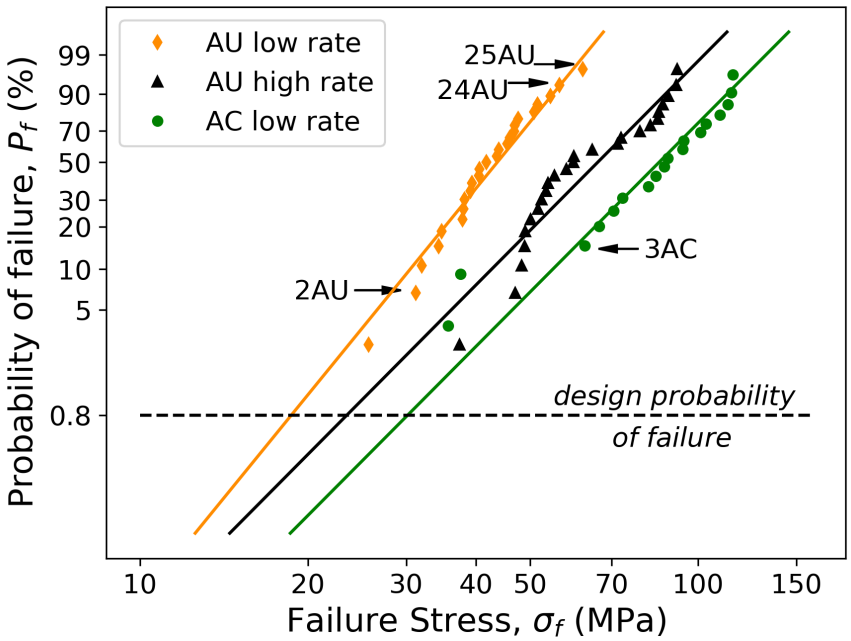

Fig. 3.9 Weibull distribution function of the probability of failure for coated (AC) and uncoated (AU) naturally aged glass samples. The specimens subjected to microscopy inspection after the test are identified by a label

Table 3.3 Statistical data of the experimental results

Id. code	Type of glass	Coating	Loading rate (MPa/s)	No. of valid specimens	Weibull param. $\hat{\beta}$	Weibull param. $\hat{\theta}$ (MPa)	$\hat{CV}$ (%)	$\hat{\sigma}_{f,0.008}$ (MPa)
NU low rate	new	un-coated	0.15	23	5.2	68.3	24.2	26.8
NU high rate	new	un-coated	3.00	25	5.8	85.3	20.6	37.3
NC low rate	new	coated	0.15	17	5.6	121.8	17.7	51.4
AU low rate	aged	un-coated	0.15	25	5.3	46.8	19.6	18.7
AU high rate	aged	un-coated	3.00	25	4.3	72.0	25.7	23.4
AC low rate	aged	coated	0.15	18	4.3	92.7	28.2	30.2

3.3.3 Comparison between Weibull, Normal and Log-Normal distributions

Comparisons with the Normal, Log-Normal and Weibull distributions are made with the Anderson Darling goodness-of-fit test, that is commonly used during the assessment of glass strength data [69].

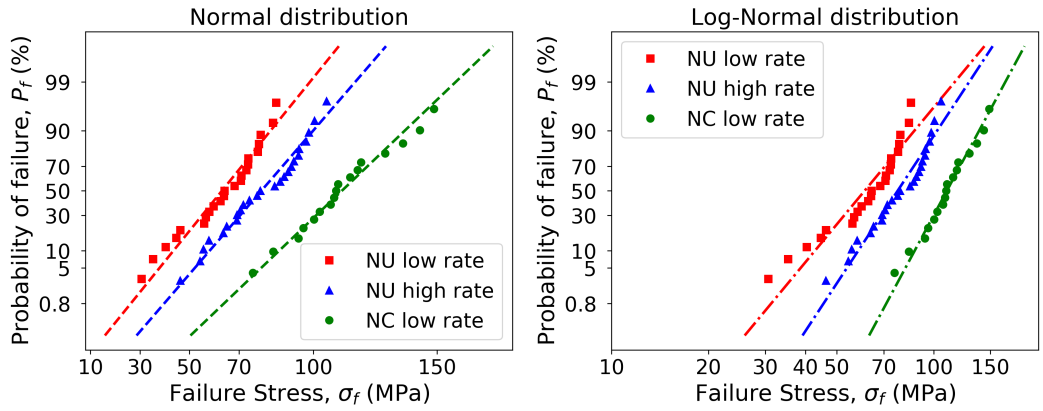

(a) (b)

Fig. 3.10 (a) Normal and (b) Log-normal probability plots for the experimental failure stress values of new glass

The data listed in Table 3.2 were interpreted through the three different distribution functions. The results were compared in order to determine which distribution best fits the experimental data. The data are correlated to the best fits for Normal and Log-Normal distributions in the linearised graphs shown in Figs. 3.10 and 3.11. The graphs allow for a visual assessment of data fitting, to have a good fit, the plots should be a straight line.

The parameters of the Gaussian and Log-Normal distribution are estimated according to the moments method. The mean μ and variance s^2 of the Normal distribution are obtained from the sample mean and variance:

$$\hat{\mu} = \frac{1}{n}\sum_{i=1}^{n} \sigma_{\mathrm{f}(i)} \tag{3.9a}$$

$$\hat{s}^2 = \frac{1}{n-1}\sum_{i=1}^{n} (\sigma_{\mathrm{f}(i)} - \hat{\mu})^2 \tag{3.9b}$$

being n the sample size and $\sigma_{\mathrm{f}(i)}$ the sample data.

The Log-normal distribution is related to the Normal distribution. If a variable is log-normally distributed, then the logarithm of that variable is normally distributed. Thus, taking the logarithm of the observations, the log-normal parameters estimation

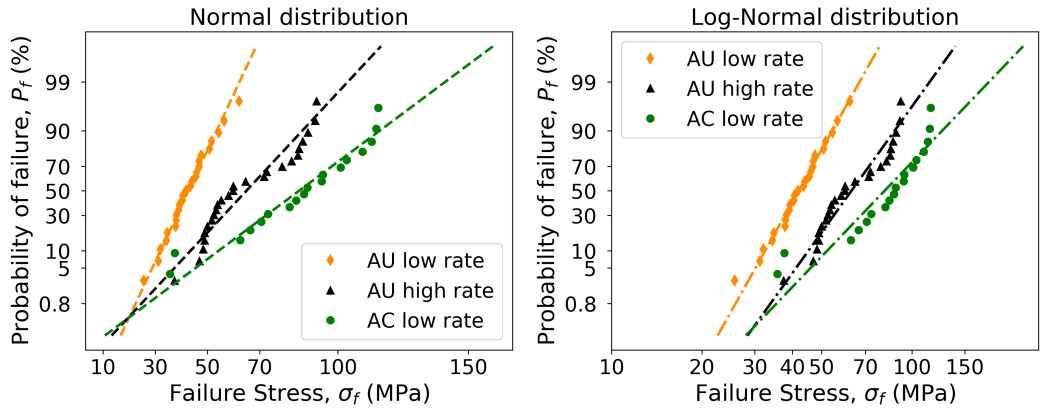

(a) (b)

Fig. 3.11 (a) Normal and (b) Log-normal probability plots for the experimental failure stress values of aged glass

can be performed using a normal analysis procedure:

$$\hat{\mu} = \frac{1}{n}\sum_{i=1}^{n} \ln\left(\sigma_{\mathrm{f}(i)}\right) \tag{3.10a}$$

$$\hat{s}^2 = \frac{1}{n-1}\sum_{i=1}^{n} [\ln\left(\sigma_{\mathrm{f}(i)}\right) - \hat{\mu}]^2 \tag{3.10b}$$

The Anderson-Darling (AD) test is used to determine whether the set of data can be adequately represented by a distribution function. The test compares the cumulative Normal, Log-normal and Weibull distribution functions, that fit the observed data best, with the cumulative distribution functions of the observed data.

The Anderson-Darling test is performed according to references [76] and [77]. The AD test statistic for Weibulness is:

$$AD = -n + \sum_{i=1}^{n} \frac{1-2i}{n}\left\{\ln\left[1-\exp\left(-\left(\frac{\sigma_{\mathrm{f}(i)}}{\theta}\right)^{\beta}\right)\right] - \left(\frac{\sigma_{\mathrm{f}(n+1-i)}}{\theta}\right)^{\beta}\right\} \tag{3.11}$$

and the observed significance level is calculated as:

$$p_{AD} = 1/\{1+\exp[-0.10+1.24\ln(AD^*)+4.48(AD^*)]\} \tag{3.12}$$

where

$$AD^* = \left(1+0.2/n^{1/2}\right)AD \tag{3.13}$$

The p_{AD} is a measure of the goodness of fit of the two-parameter Weibull distribution to the data. The greater the p_{AD} value, the closer the experimental cumulative distribution and the Weibull distribution are. If $p_{AD} \leq 0.05$, it is possible to conclude (at 5% risk of being wrong) that the population from which the sample was drawn is not a two-parameter Weibull population. Otherwise, the hypothesis that the population is a 2-parameter Weibull population is not rejected.

The Anderson-Darling test statistic for Normality is:

$$AD = -n + \sum_{i=1}^{n} \frac{1-2i}{n} \left\{ \ln \left[F_0 \left(\frac{\sigma_{f(i)} - \hat{\mu}}{\hat{s}} \right) \right] + \ln \left[1 - F_0 \left(\frac{\sigma_{f(n+1-i)} - \hat{\mu}}{\hat{s}} \right) \right] \right\} \tag{3.14}$$

where F_0 is the standard normal distribution function. The observed significance level is calculated as:

$$p_{AD} = 1/\{1 + \exp[-0.48 + 0.78\ln(AD^*) + 4.58(AD^*)]\} \tag{3.15}$$

where $AD^* = \left(1 + 4/n - 25/n^2\right) AD$.

Finally, in order to test the goodness of fit of the Log-normal distribution, the Anderson-Darling test for normality can be performed on the data $\ln\left(\sigma_{f(i)}\right)$.

To summarize all the results, the observed significance levels p_{AD} and the 0.8% fractiles associated with the various statistical models are listed in Tab. 3.4, where the lowest 0.8% fractile and the highest goodness-of-fit index, p_{AD}, are indicated in bold for each type of glass.

Based on the results of Tab. 3.4, the Weibull distribution does not always produce the best goodness-of-fit, however, on average, it is the most accurate method to statistically represent the failure stress of the various type of glass. Moreover, it worth noticing the Weibull statistic is the most conservative, as in five out of six cases, it returns the least 0.8% fractiles. In conclusion, it is important to remark that the sampling distribution of the naturally aged un-coated glass samples (AU high rate) can not be properly represented by the Normal, Log-Normal and Weibull distributions as shown in Tab. 3.4 and in Figs. 3.11 and 3.9. The experimental results could be more accurately interpolated by a bilinear and bimodal Weibull distributions in accordance with the findings of Ballarini *et al.* [78]. Otherwise, the

Table 3.4 Comparison between the three statistical distributions

Type of glass	Normal		Log-Normal		Weibull	
	$\sigma_{f,0.008}$ (MPa)	p_{AD}	$\sigma_{f,0.008}$ (MPa)	p_{AD}	$\sigma_{f,0.008}$ (MPa)	p_{AD}
NU low rate	26.3	0.22	31.30	0.02	**26.8**	**0.31**
NU high rate	39.8	0.35	45.50	0.17	**37.3**	**0.47**
NC low rate	63.9	0.64	71.26	**0.71**	**51.4**	0.29
AU low rate	22.5	0.74	25.87	**0.75**	**18.7**	0.30
AU high rate	24.7	0.01	33.82	0.04	**23.4**	0.01
AC low rate	**27.1**	0.34	35.41	0.01	30.2	**0.35**

Anderson-Darling test shows that the experimental results for the other typologies of glass can be realistically represented by the Weibull distribution. As a result, the effectiveness of the coating can be effectively quantify by comparing the Weibull distributions for coated and un-coated glass tested at low stress rate.

3.3.4 Microscopy inspection

After each test, the crack pattern was carefully analysed by naked eye to identify the position of the flaw that caused the specimen failure (see, for example, Figs. 3.12a and 3.13a, where the critical flaw is pinpointed by a black arrow) and to discard possible invalid tests, i.e., those with origin of failure located outside the loading ring. Moreover, an inspection with an optical stereo microscope Nikon SMZ18 was carried out on selected specimens to investigate the relation between flaw size and failure stress and the effect of the coating. Starting from the identification of the likely origin of failure (Fig. 3.12a), a first magnification of the lateral face of the fragment has permitted to identify the different regions of crack propagation that develop around the origin, i.e., mirror, mist and hackle zones, and Wallner lines (Fig. 3.12b). Finally, a further magnification permitted to reveal and measure the size of the critical flaw (Fig. 3.12c).

The microscopy inspections shown in Figs. 3.12 and 3.13 refer to a new un-coated specimen, identified with the id. number 21NU, and an aged un-coated specimen, identified with the id. number 24AU, respectively. These two specimens had the same kind of critical defect, namely a pit, and a similar probability of failure, being $P_f = 88.5\%$ for 21NU and $P_f = 93.3\%$ for 24AU (see Fig. 3.7). However,

different values of failure stress, $\sigma_f = 78.7$ MPa for 21NU and $\sigma_f = 56.5$ MPa for 24AU, correspond to the same probability of failure because of a different distribution of defect size for new and aged glasses. In fact, the depth of the critical flaw is about 35 µm for specimen 21NU and 60 µm for specimen 24AU. In this case, the difference in the failure stress can be easily interpreted on the base of the relationship between failure stress and crack size derived from linear elastic fracture mechanics:

$$\sigma_f = \frac{K_{IC}}{Y\sqrt{\pi a}}, \tag{3.16}$$

where: Y is a geometry and loading factor, a is the crack depth, and K_{IC} is the fracture toughness. Moreover, given a fracture toughness for soda-lime glass K_{IC} = 0.75 MPa $m^{\frac{1}{2}}$ and, considering the shape of the cracks (see Figs. 3.12 and 3.13), a geometry factor Y = 0.94 (which is between Y = 0.713, that holds for half-penny shaped cracks, and Y = 1.12, that holds for straight-fronted edge cracks in a semi-infinite solid [14]), Eq. (3.16) gives the failure stresses of $\sigma_f = 76.1$ MPa for specimen 21NU, and $\sigma_f = 58.1$ MPa for specimen 24AU. These two values are very close to the experimental ones.

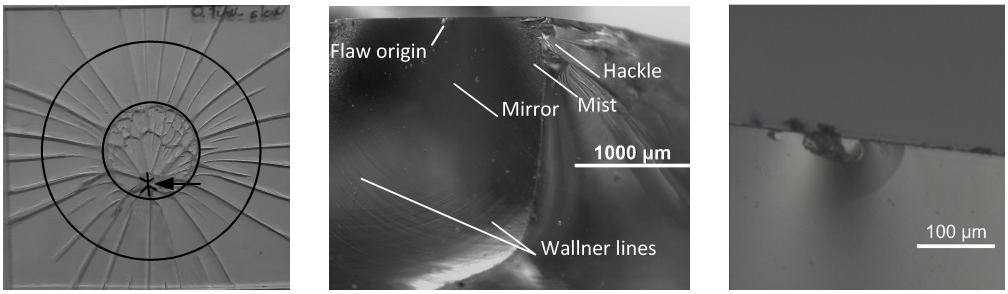

(a) (b) (c)

Fig. 3.12 Fractography of sample 21NU, $\sigma_f = 78.7$ MPa: (a) location of the likely origin of failure; (b) mirror, mist and hackle zones, Wallner lines; (c) critical flaw

The critical flaws shown in Fig. 3.14 refer again to two un-coated specimens, namely 2NU and 2AU, which have a similar probability of failure, placed on the left tail of the Weibull diagram (see Fig. 3.7). In this case, the two defects have a similar depth, equal to about 100 µm, although a different shape: the specimen 2NU has a pit, whereas the specimen 2AU has a scratch.

The pictures shown in Fig. 3.15 allow to compare the critical flaw of an aged un-coated specimen, 25AU, with that of an aged coated specimen, 3AC. The two samples have critical flaws with the same shape –half-penny shape– and depth equal

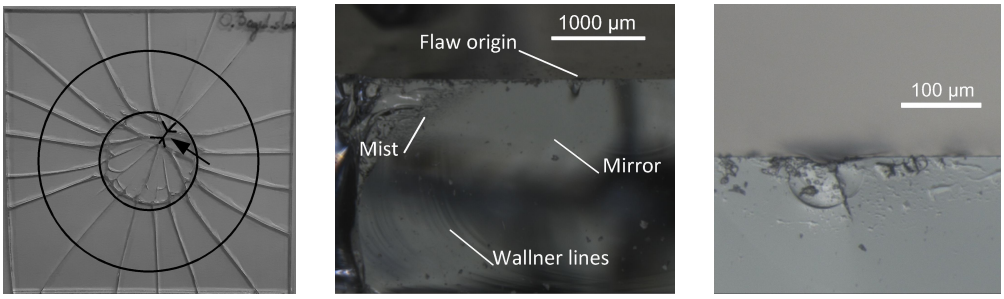

(a) (b) (c)

Fig. 3.13 Fractography of sample 24AU, $\sigma_f = 56.5$ MPa: (a) location of the likely origin of failure; (b) mirror and mist zones, Wallner lines; (c) critical flaw

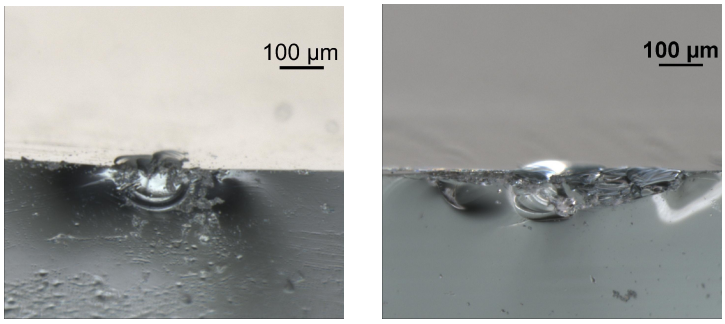

(a) (b)

Fig. 3.14 Critical flaw: (a) sample 2NU, $\sigma_f = 35.3$ MPa; (b) sample 2AU, $\sigma_f = 31.2$ MPa

to about 50 µm. Both failed under a bending stress of about 62 MPa. The critical flaw of specimen 25AU is the smallest we found for the set of aged un-coated specimens, whereas that of specimen 3AC is one of the largest within the set of aged coated specimens (see Fig. 3.9). Since un-coated and coated samples belonged to the same set of aged glass panes, and there was no reason for having larger defects in un-coated samples, we can infer that the original critical flaw in specimen 25AU was smaller than that in specimen 3AC and it grew during the test because of stress corrosion up to the size shown in Fig. 3.15a. Moreover, since defects with the same shape and size gave the same failure stress in un-coated and coated conditions, we may suppose that the coating does not exert any mechanical strengthening. However, such a conclusion cannot be drawn based on only two specimens. A final statement on this aspect would require further investigations, which include also the comparison of the bending stiffness of un-coated and coated specimens.

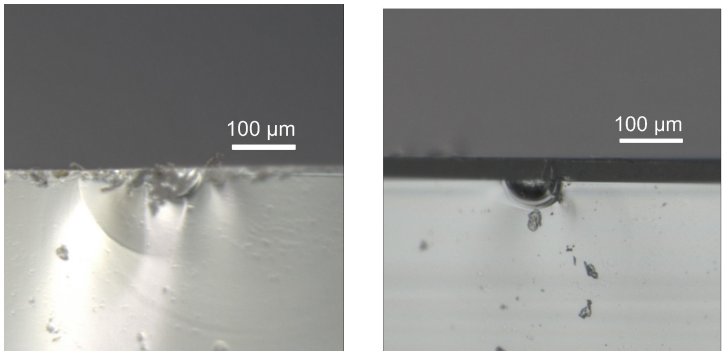

(a) (b)

Fig. 3.15 Critical flaw: (a) sample 25AU, $\sigma_f = 62.1$ MPa; (b) sample 3AC, $\sigma_f = 62.6$ MPa

Furthermore, Figs. 3.12c and 3.15a, that refer to uncoated and low stress rate tested glass specimens, both show the semi-elliptical line which is left by the slow crack growth [79–81].

Finally, Fig. 3.16 shows the critical flaw of a new un-coated specimen, 12NU, and that of a new coated specimen, 10NC. The failure stress of such samples is close to the mean strength ($P_f = 50\%$) of the corresponding set of specimens. The size of the two defects is very different, thus confirming the effectiveness of the coating in inhibiting stress corrosion.

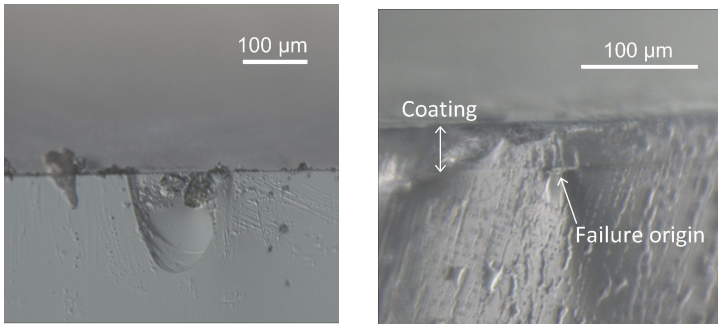

(a) (b)

Fig. 3.16 Critical flaw: (a) sample 12NU,$\sigma_f = 64.1$ MPa; (b) sample 10NC, $\sigma_f = 110$ MPa

3.4 Conclusions

A UV-curable polymeric coating has been tested as a barrier layer to prevent glass stress corrosion. Its performance has been assessed by comparing the failure stress of un-coated and coated specimens, tested with the coaxial double ring setup. The results reported in Section 3.3.2 prove that the proposed formulation is highly effective for both new and naturally aged glass. The increase of the bending strength corresponding to a probability of failure of 0.8% is equal to 92% for new glass and 62% for aged glass. Besides the very good performance against stress corrosion, the developed coating has some advantages compared to other strengthening techniques and coatings: it is solvent free, it has a very fast curing time, it is low-energy consuming, and it can be easily included in the continuous production systems of flat glass as well as it is available for in-situ applications.

While the effectiveness of the coating in preventing stress corrosion within few days after its application on the glass substrate has been proven, its durability will be discussed in Chapter 4. In this context, three scenarios will be investigated: (*i*) artificial weathering carried out by exposing coated specimens to fluorescent UV lamps, heat and water, following standardized cycles such as those proposed by [82]; (*ii*) natural weathering carried out by exposing coated specimens to atmosphere agents; (*iii*) mechanical ageing by subjecting coated samples to cyclic loads in order to stress repeatedly the coating and evaluate the appearance of possible micro-cracking in the coating that can reduce the water vapour barrier effect.

Chapter 4

Durability analysis of the coating[1]

4.1 Introduction

A functional polymeric coating prepared with an UV-curable resin, a fluorinated methacrylate co-monomer, and a co-reactive silane primer has been developed. According to the study reported in Chapter 3, the application of the coating leads to an increase of the bending strength corresponding to a probability of failure of 0.8% equal to 92% for new glass and 62% for aged glass. Besides the very good performance against stress corrosion, the developed coating has some advantages compared to other strengthening techniques and coatings: it is solvent free, it has a very fast curing time, it is low-energy consuming, and it can be easily included in the continuous production systems of flat glass as well as it is available for in-situ applications. Therefore, it could find applications in the production of new structural elements that will be subjected to significantly high long-term loads and in the strengthening of existing elements.

While the effectiveness of the coating in preventing stress corrosion within few days after its application on the glass substrate was proven in Chapter 3, the analysis of its durability is the main objective of the present Chapter. In this context, three scenarios were analysed to consider most of the possible sources of ageing a glass structural element might be subjected to: (i) cyclic loading, obtained by subjecting

[1]Part of the work described has been previously published in:
G. Mariggiò, S. Dalle Vacche, R. Bongiovanni, C. Louter, M. Corrado. A durable coating to prevent stress corrosion effects on the surface strength of annealed glass. Glass Struct. Eng. 6, 449-462 (2021).

coated samples to cyclic loads in order to stress repeatedly the coating and evaluate the appearance of micro-cracking that can reduce the water vapour barrier effect; (ii) natural weathering, performed by exposing coated samples to atmospheric agents; (iii) artificial weathering, carried out by exposing coated specimens to fluorescent UV lamps, heat and water.

4.2 Experimental programme

The experimental programme consisted in the preparation of a set of coated glass specimens for each type of ageing. The ageing of the specimens and their mechanical testing aim to assess the durability of the coating through the evaluation of its residual effectiveness in preventing stress corrosion. The materials and the procedures for ageing and testing are explained in the present section.

4.2.1 Materials

The details of the formulation of the coating were discussed in Chapter 2. The formulation was developed to give the coating compositionally graded properties, assuring a good barrier to water vapor, hydrophobicity, transparency, and adhesion to the substrate in a single layer, as required for preventing stress corrosion of glass. The physical-mechanical properties of the coating are summarised in Table 4.1. In particular, Table 3.1 lists the water vapor transmission rate, $WVTR_{25}$, the water contact angle, θ_{water}, and the adhesion strength, τ, of the coating.

Table 4.1 Summary properties of the coating

$WVTR_{25}$ ($g/m^2/24h$)	θ_{water} ($^\circ$)	Adhesion strength τ (MPa)
87.1 ± 15.8	103.2 ± 1.6	24.9 ± 2.8

Square soda-lime silica plates were employed for preparing the specimens. In particular, the glass samples examined in this Chapter, as well as the glass designated as "New" in Chapter 3, are all from the same batch.

4.2.2 Preparation of test specimens

The procedure for preparing the specimens is described in Section 3.1 and summarized below:

1. Silanization in aqueous solution of the glass specimens;
2. Coating mixing and application with a steel spiral bar;
3. Curing of the coating using a 5000-EC UV flood lamp system.

A transparent solid film with a thickness of around 50 µm was obtained after irradiation. The coating was applied to the air side of the flat glass specimens, with a self-adhesive film applied to the tin side to keep the fragments together after the specimens were fractured.

4.2.3 Cyclic loading

A set of 22 coated square glass samples having edge length $l = 120$ mm and nominal thickness $h = 4$ mm were subjected to cyclic equi-biaxial bending loadings by means of the coaxial double ring setup. This setup, as shown in Fig. 3.3, consists of two steel rings of different diameters: the largest one supports the specimens, while the smallest one is used to apply a force normal to the upper surface of the sample, thus resulting in a bi-axial bending stress state in the square sample. The diameters of the support and load rings, D_S and D_L, respectively, have been defined as a function of the dimensions of the specimens, in accordance to the ASTM C1499-19 standard [68]. In detail, they were $D_S = 90$ mm and $D_L = 40$ mm for $l = 120$ mm and $h = 4$ mm.

Cyclic loading was defined by a saw-tooth wave with minimum load equal to 1031 N, maximum load equal to 1915 N and frequency of 3 Hz (see Fig. 4.1). The force controlled cyclic loading was performed for 20,000 cycles. The cyclic load parameters are summarised in Table 4.2.

The biaxial tensile stress, $\sigma_1(t)$, occurring in the central portion of the specimens, on the coating side, was calculated from the load, $Q(t)$, by means of the following

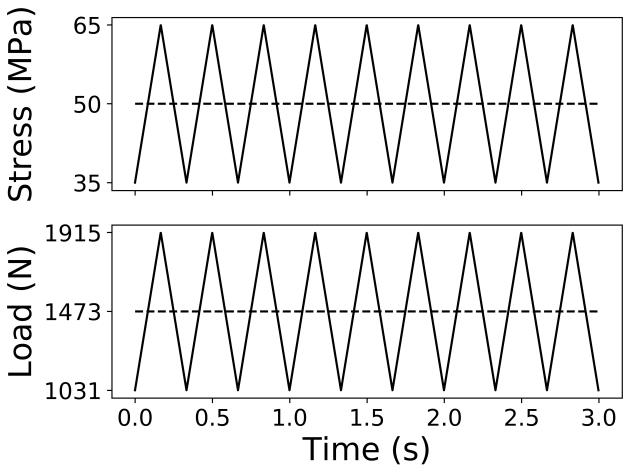

Fig. 4.1 Schematic diagrams of the cyclic loadings.

Table 4.2 Cyclic loading parameters (load and stress amplitude are defined as $\Delta Q = Q_{max} - Q_{min}$ and $\Delta\sigma = \sigma_{max} - \sigma_{min}$, respectively)

Frequency (Hz)	Mean load $\overline{Q}$ (N)	Load amplitude ΔQ (N)	Mean stress $\overline{\sigma}$ (MPa)	Stress amplitude $\Delta\sigma$ (MPa)	Number of cycles (-)
3	1473	884	50	30	20,000

equation, provided by ASTM C1499-19 [68]:

$$\sigma_1(t) = \frac{3Q(t)}{2\pi h^2}\left[(1-\nu)\frac{D_S^2 - D_L^2}{2D^2} + (1+\nu)ln\frac{D_S}{D_L}\right] \tag{4.1}$$

where: $Q(t)$ is the time varying load, h is the nominal thickness of the specimen, D_S and D_L are the diameters of the support and load rings, respectively, $\nu = 0.22$ is the Poisson's ratio of glass, and D is the diameter of the glass specimen which is obtained by Eq. (3.2).

The fatigue load parameters were chosen to maximise the stretching of the coating without reaching the fracture of the specimen by fatigue or even by simple static loadings. The mean value of $\sigma_1(t)$ and the stress amplitude are computed by applying Eq. (4.1), and reported in Table 4.2. A large value of the mean stress and a low stress amplitude have been chosen to maintain a high level of tensile stress on

the coating side during the entire cyclic load testing, a condition needed to activate the stress corrosion. Furthermore, in order to reproduce an environmental condition as harsh as possible, the support ring and the specimen were immersed in water for the entire duration of the test (see Fig. 3.3b). The pH of the water was monitored using full range pH strips (1-14) to verify that the solution was neutral. The cyclic loading tests were conducted at room temperature.

4.2.4 Natural weathering

A set of 15 coated square glass samples having $l = 120$ mm and $h = 4$ mm were exposed to atmospheric agents for 510 days (17 months), from February 4th 2019, to June 30th 2020, to assess the durability of the coating against natural weathering. The samples were mounted on a frame placed horizontally on the roof of a building of Politecnico di Torino, Corso Duca degli Abruzzi, 24, Torino (Lat: 45.0628, Long: 7.6621, Alt: 254 m. a.s.l) (see Fig. 4.2). The actual peak to peak variations in temperature and maximum irradiance (SRmax) were between 38.8°C (summer) and -1.5°C (winter) and between 1256 W/m^2 (summer) and 33 W/m^2 (winter), respectively. Throughout the monitored period, the average relative humidity amounted to 63.46 %, while the precipitation peaked at 92.66 mm. The daily variations of the weathering conditions to which the specimens were exposed are reported in Fig. 4.3. The number of days of exposure per season and the average weathering parameters are summarised in Table 4.3.

Fig. 4.2 Set of 15 coated glass specimens exposed to atmospheric agents.

The data about the environmental conditions were taken from the Meteorological Station of Atmospheric Physics at the Department of Physics of the University of Turin, Via Pietro Giuria, 1, Torino (Lat: 45.0521, Long: 7.6814). At the end of

Table 4.3 Natural weathering parameters: average relative humidity (ARH), average maximum temperature (ATmax), average maximum irradiance (AImax).

Days of exposure	Season	ARH (%)	ATmax °C	AImax W/m^2
0 - 41	winter	52.27	15.63	582.85
42 - 134	spring	57.63	21.38	887.57
135 - 227	summer	63.22	29.55	866.26
228 - 317	autumn	79.73	14.98	379.52
318 - 407	winter	61.76	13.08	456.21
408 - 500	spring	60.90	21.41	873.65
501 - 510	summer	58.4	30.13	987.7

the weathering period, all the specimens were removed from the roof, analysed and tested with the coaxial double ring setup.

4.2.5 Artificial weathering

A set of 19 coated square glass samples having $l = 75$ mm and $h = 3$ mm were artificially weathered to establish the long-term effects of light, heat and moisture on the mechanical, chemical and physical properties of the coating. Weathering was carried out using a UV accelerated weathering equipment made available by the Cromology Italia S.p.A laboratories (Porcari, Italy). Due to the lacking of a specific standard, the weathering was done following the procedure provided by [82], which is the reference Standard for testing the durability of paints and varnishes exposed to outdoor environmental conditions. This Standard was chosen in place of those for structural silicones and sealants (see ETAG 002-5.1.4.2.1 [83] and EN ISO 11431 [84]), because the surface of contact for coatings, that strongly influences chemical reactions, is comparable to that for paints, and it is commonly wider than that for adhesives and sealants. However, the Standards for paints and those for sealants specify quite similar weathering conditions.

Weathering cycles lasted 8 h each, and consisted of two exposure periods: (i) 4 h of UV radiation and drying at 60 °C and (ii) 4 h of UV radiation and condensation at 50 °C. The irradiance of the UV lamp was 0.83 W/m^2/nm, at 340 nm. Condensing humidity is considered the best way to simulate outdoor moisture attack because

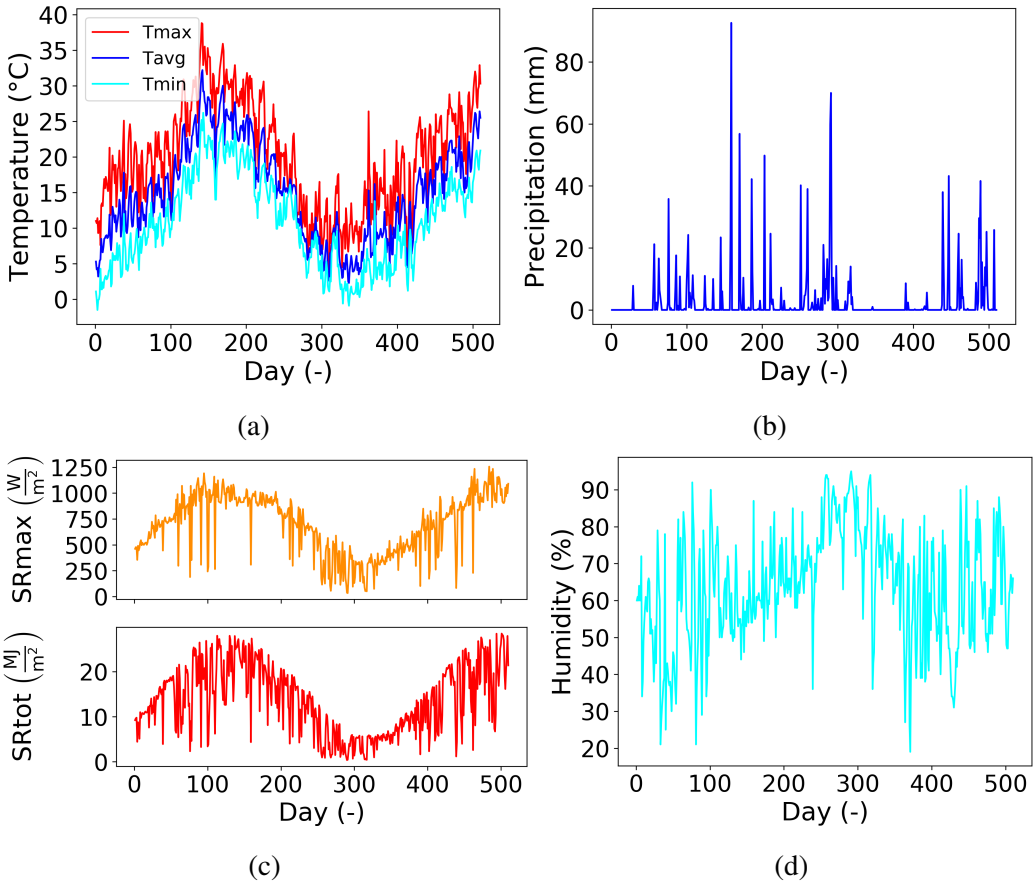

Fig. 4.3 Natural weathering conditions: (a) maximum, average and minimum daily temperatures; (b) daily precipitation heights; (c) maximum solar irradiance (SRmax) and daily solar irradiation (SRtot) ; (d) average daily relative humidity.

most of this moisture is the result of dew. The artificial weathering conditions are summarised in Table 4.4 for convenience.

The weathering cycles were conducted for 7 weeks (1176 h), which is twice as long as EN ISO 11431 [84] specifies for sealants. The samples were then removed from the ageing machine, analysed and tested with the coaxial double ring setup. In order to track the evolution of the ageing, a specimen was taken every week of exposure to artificial weathering and analysed through visual inspection.

Table 4.4 Artificial weathering conditions per cycle

step	Exposure period	Irradiance	Temperature	Relative humidity
1	4 h dry	0,83 W/m^2/nm at 340 nm	60±3 °C	Not controlled
2	4 h condensation	0,83 W/m^2/nm at 340 nm	50±3 °C	Not controlled

4.2.6 Characterisation methods

After the ageing processes, the coated surface of all the glass samples was visually inspected to identify and localise defects in the coating. Then, different analyses were carried out depending on the ageing process.

Static contact angle measurements were carried out to assess the surface properties of the coated glass samples, before and after the natural weathering. The results have been compared to those of un-coated glass. A Krüss DSA100 instrument (KRÜSS GmbH, Hamburg, Germany) was used, equipped with video camera and image analysis software, with the sessile drop technique. Water was used as testing liquid, and the drops were of 10 µl. Five measurements were taken on un-coated glass specimens, seven on freshly coated glass specimens and ten on naturally weathered coated glass specimens which had been washed with water and soap and rinsed with distilled water after exposure. It is to be noted that the label "freshly coated glass specimens" identifies the samples tested within few days after the application of the coating.

The transparency of the naturally weathered coated glass samples was also assessed, by means of a JENWAY 6850 UV/Vis (Cole-Parmer, Stone, UK) UV-visible spectrophotometer.

FTIR-ATR spectroscopy was used to track the evolution of the coating ageing for the artificially weathered coated samples. At that purpose, this analysis was carried out to specimens exposed for 1, 2, 3, ... up to 7 weeks of ageing. A specimen has been taken out from the weathering machine each week and stored in dark and dry conditions up to the end of the seventh week, when the FTIR-ATR spectroscopy was applied to all the specimens. For this reason, only the 13 specimens, out of the initial 19 ones, that reached the seventh week of ageing were mechanically tested to assess the performance of the aged coating.

After the aforementioned non-destructive investigations, mechanical tests were carried out on all the coated glass samples to evaluate the residual effectiveness of the aged coating in protecting the glass surface from stress corrosion. The coaxial double ring set-up was used (see Fig. 3.3) in accordance to the ASTM C1499-19 standard [68]. The dimension of support and load rings for specimens having edge size $l = 120$ mm and thickness $h = 4$ mm, were $D_S = 90$ mm and $D_L = 40$ mm as already explained in Section 4.2.3, whereas D_S and D_L for specimens having $l = 75$ mm and $h = 3$ mm were 60 mm and 30 mm, respectively. During the loading tests, the specimens and the support ring were placed into a tank filled with water to create a harsh environment with a steady humidity level. The mechanical tests were carried out by means of a servo-hydraulic MTS universal testing machine with a load cell capacity of 10 kN. A constant displacement rate was applied to induce in the specimens a stress rate equal to 0.15 MPa/s, until failure. A low loading rate was chosen instead of a constant load to have certain and reasonably limited testing times and to facilitate a quantitative comparison between un-coated and coated glass samples. In case the stress corrosion is completely prevented by the coating, in fact, the coated glass samples would never break under a constant load. The value of 0.15 MPa/s, which caused fracture of the samples within 6–14 min, was chosen based on evidences that such a rate is low enough to reveal the effects of stress corrosion as shown in Chapter 3 and in ref. [49]. The bending strength, σ_f, was calculated from the fracture load, Q_f, by means of Eq. (4.1) and the results were compared to those of freshly coated and un-coated glass samples, reported in Chapter 3. Examples of the crack pattern typically obtained with the coaxial double ring test are shown in Fig. 4.4 for two extreme values of bending strength: the higher is the bending strength, the smaller is the average fragments size. It is worth noticing that the test is valid only if the origin of fracture is located inside the footprint of the loading ring.

4.2.7 Statistical analysis of strength data

The randomly distributed micro-cracks on the glass surface and their randomly distributed geometry and depth cause a very strong scattering of the glass bending strength. Therefore, a statistical inference of the strength data was performed in accordance to the Section 3.2.2.

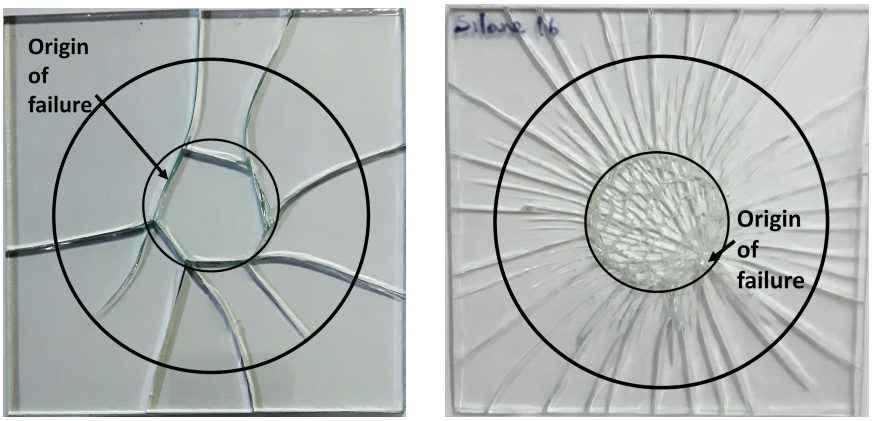

(a) (b)

Fig. 4.4 Crack patterns obtained from: (a) an un-coated specimen, which exhibited a bending strength of 35 MPa, and (b) a coated specimen, which developed a bending strength of 110 MPa

4.3 Results and discussion

In the present section, the results of the tests carried out to evaluate the effects of ageing on the performance of the coating against stress corrosion are presented and discussed. The performance of the aged specimens has been assessed against the performance of un-coated specimens and freshly coated specimens, i.e. samples tested within few days after the application of the coating, whose results can be found in Chapter 3.

After the ageing processes, all the specimens were cleaned and inspected by naked-eye to localize defects in the coating. The surface damage was visually examined with the specimen placed on a table under regular ceiling-lighting conditions. No evident imperfections were detected on the coated surfaces of cyclically aged and naturally weathered samples, whereas artificially weathered specimens exposed for six and seven weeks exhibited cracking and delamination of the coating (see Fig. 4.5).

4.3.1 Experimental results

The experimental bending strength values σ_f, that were assessed using the coaxial double ring set-up, are listed in ascending order in Table 4.5 for the following types

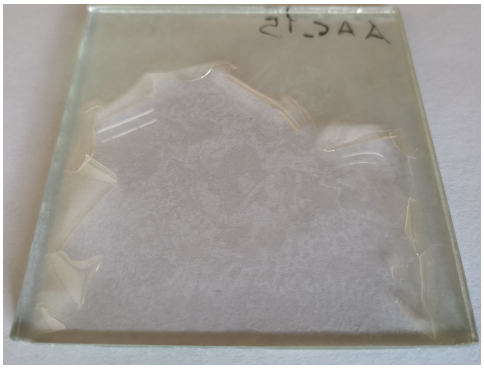

Fig. 4.5 Qualitative assessment, by visual inspection, of coating deterioration after seven weeks of exposure to artificial weathering

of glass samples: (*i*) cyclic loaded coated (CLC); (*ii*) naturally weathered coated (NWC); (*iii*) artificially weathered coated (AWC); (*iv*) 75 mm wide uncoated glass (UC75).

4.3.2 Effects of cyclic loading

The bending strength of each cyclic loaded coated specimen was evaluated by means of the coaxial double ring test directly after the cyclic loading procedure, to avoid possible crack healing effects. The Weibull diagram obtained from the set of specimens is shown in Fig. 4.6, where it is compared to the Weibull diagrams of the bending strength of un-coated and freshly coated samples.

A first qualitative analysis of the experimental data points suggests that the coating has a high durability against cyclic loading since the distribution of the probability of failure of cyclic loaded coated specimens is very close to that of freshly coated specimens. Straight lines, which represent the linearised Weibull distribution function, fit well the experimental data sets, indicating that the Weibull distribution can be used to interpret them correctly. The curve that best fits the data points of cyclic loaded coated specimens (purple triangular markers) is characterised by $\hat{\beta} = 4.34$ and $\hat{\theta} = 109.99$ MPa, that of un-coated specimens (red square markers) is defined by $\hat{\beta} = 5.16$ and $\hat{\theta} = 68.25$ MPa, while that of freshly coated specimens (green circular markers) by $\hat{\beta} = 5.60$ and $\hat{\theta} = 121.80$ MPa. The effectiveness of the coating can be quantified by the scale parameter $\hat{\theta}$, which represents the strength associated to a probability of failure of 63.2%.

Table 4.5 Strength data σ_f in MPa by glass type

Specimen	CLC σ_f (MPa)	NWC σ_f (MPa)	AWC σ_f (MPa)	UC75 σ_f (MPa)
1	60.44	35.65	22.63	30.08
2	71.95	56.71	51.38	33.28
3	73.52	63.84	55.64	35.41
4	80.41	74.03	67.89	37.0
5	84.21	79.46	74.27	38.60
6	91.0	84.79	78.53	40.7
7	94.91	84.89	82.26	41.26
8	98.47	85.57	84.39	49.25
9	98.51	92.97	92.38	55.64
10	99.63	105.60	99.30	59.90
11	101.70	111.89	108.88	62.60
12	102.21	122.92	114.74	70.0
13	104.82	123.26	132.84	73.20
14	109.17	130.05	-	74.30
15	130.77	132.77	-	74.27
16	132.87	-	-	79.60
17	140.58	-	-	98.23
18	-	-	-	104.10

Furthermore, the comparison between the Weibull shape parameters, $\hat{\beta}$, allows to derive very interesting insights on the behaviour of cyclic loaded coated specimens. As expected, the parameter $\hat{\beta}$, which represents the slope of the linearised Weibull diagram and thus describes the strength scatter as well as the dispersion of the size of the critical surface defects, is almost the same for freshly coated and un-coated glass samples, whereas it differs for cyclic loaded samples. In particular, the data points of cyclic loaded coated and freshly coated samples are almost paired for a probability of failure $P_f > 70\%$, whereas they diverge for low values of P_f. It is opinion of the authors that the variation of $\hat{\beta}$ is not sign of a deterioration of the coating. On the contrary, it is a proof of a very good performance of the coating during the ageing process. Let us assume that the coating is able to completely prevent stress corrosion (static fatigue) during the ageing process. In that case, the specimen is subjected only to dynamic fatigue, which can be described by a classical Paris-Erdogan's law [85]. However, as it is well known, the sub-critical propagation of cracks by fatigue occurs only when the stress intensity factor at the crack tip overcomes a threshold, which is

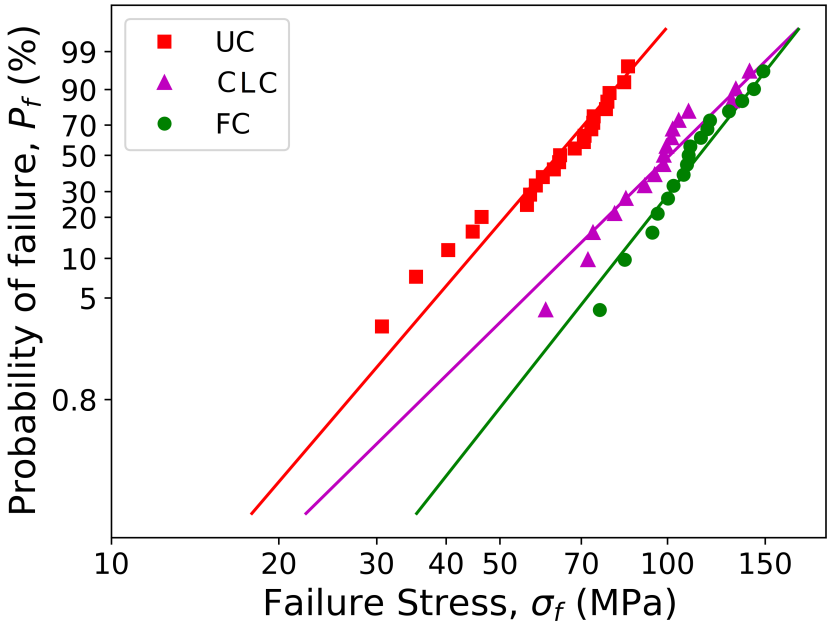

Fig. 4.6 Weibull distribution functions for the bending strength of un-coated (UC), freshly coated (FC) and cyclic loaded coated (CLC) glass samples

a material property. Since the mean stress and the stress amplitude were the same for all the specimens, only the largest critical surface flaws propagated by fatigue, whereas the smallest ones were not sufficiently stressed. Consequently, the scatter of the size of the critical defects increased, leading to a decrease of the parameter $\hat{\beta}$. In that regard, it has to be remarked that five specimens broke during the cyclic loading, after a number of cycles in the range 4,000 to 15,000, probably due to the fact that the critical flaws were large enough to propagate by dynamic fatigue up to reaching the condition of unstable crack propagation.

In the absence of coating, or in the case of a fast deterioration of the coating, the specimen would be subjected to both static and dynamic fatigue. In such a circumstance, the effect of stress corrosion (static fatigue) prevails by far on the effect of dynamic fatigue, especially for small defects. This is consistent with the results of Lü [86], who indicated that the cyclic fatigue life of soda-lime glass is solely dependent on the cumulative time for static fatigue, and Schneider and Hilcken [87], who found that the existing models for static fatigue used in linear elastic fracture mechanics can be adopted for the lifetime prediction of cyclically loaded annealed glass. The crack propagation per cycle can be described by the

Evans' law [88]:

$$\frac{da}{dN} = \lambda g A \overline{K}_{\mathrm{I}}^{n} \tag{4.2}$$

where g and the crack velocity parameters A and n depend on the loading conditions, the material, the temperature and the environment, λ is the period of the cyclic loading, and $\overline{K}_{\mathrm{I}}$ is the average stress intensity factor per cycle:

$$\overline{K}_{\mathrm{I}} = \overline{\sigma} Y \sqrt{\pi a} \tag{4.3}$$

being $\overline{\sigma}$ the average stress, Y a geometry and loading factor, and a the crack depth. Therefore, the crack propagation rate strongly depends on the initial crack depth, since it varies directly as $a^{(n/2)}$, the deeper the initial surface defect, the faster the crack propagation rate.

An example is herein provided to highlight the fact that most of the cyclic loaded glass samples would have fractured during cyclic loading had they not been covered by the developed coating. The cyclic loaded coated and freshly coated samples were prepared with glass plates coming from the same batch and, therefore, we can reasonably assume that they had the same initial surface defects density and size. Now, assuming that freshly coated glass samples were not affected by stress corrosion, the size of the critical surface defect, i.e., the one that lead to fracture, can be obtained by the relationship between fracture stress and crack size derived from linear elastic fracture mechanics:

$$a_{\mathrm{cr}} = \frac{1}{\pi} \left(\frac{K_{\mathrm{IC}}}{Y \sigma_{\mathrm{f}}} \right)^{2} \tag{4.4}$$

where the value of the fracture toughness K_{IC}, ranging from 0.72 to 0.82 MPa $\mathrm{m}^{1/2}$ for soda-lime glass, is set for this example to 0.75 MPa $\mathrm{m}^{1/2}$, and the geometry and loading factor Y is equal to 1.12 for straight front plane edge cracks in a semi-infinite solid [14]. The bending strength of the freshly coated glass referred to a probability of failure $P_{\mathrm{f}} \leq 63.2\%$ is $\sigma_{\mathrm{f}} \leq \hat{\theta}_{\mathrm{FC}} = 121.80$ MPa and, therefore, by Eq. (4.4) it can be inferred that the 63.2% of the statistical population of the critical surface defects has an initial depth $a_{\mathrm{cr}} \geq 9.62$ μm. For constant environmental conditions, the parameter A in Eq. (4.2) may be expressed as [10]:

$$A = \frac{v_0}{K_{\mathrm{IC}}^{n}} \tag{4.5}$$

where $v_0 = 30$ mm/s and $n = 16$ are representative of glass permanently immersed in water [26]. Evans and Fuller [88] showed that, for a saw-tooth stress wave, g parameter in Eq. (4.2) may be approximated as:

$$g \simeq \left(\frac{2^n}{n+1}\right) \frac{\exp\left[\frac{(n-1)}{4}\frac{\Delta K_\mathrm{I}}{\overline{K}_\mathrm{I}}\right]}{\exp\left[\frac{(n-1)}{2}\right]} \tag{4.6}$$

being ΔK_I the stress intensity factor amplitude per cycle. Setting the initial depth of the critical surface flaw $a_\mathrm{cr} = 9.62$ μm and the period $\lambda = 1/3$ s, the implementation of Eq. (4.2) in a numerical algorithm shows that a glass sample would fail within 13 cycles, as shown in Fig. 4.7, if subjected to cyclic loading conditions as described in Section 4.2.3 and summarised in Table 4.2. This example illustrates that much more than five samples would have fractured within 20,000 cycles had stress corrosion occurred on the covered glass specimens.

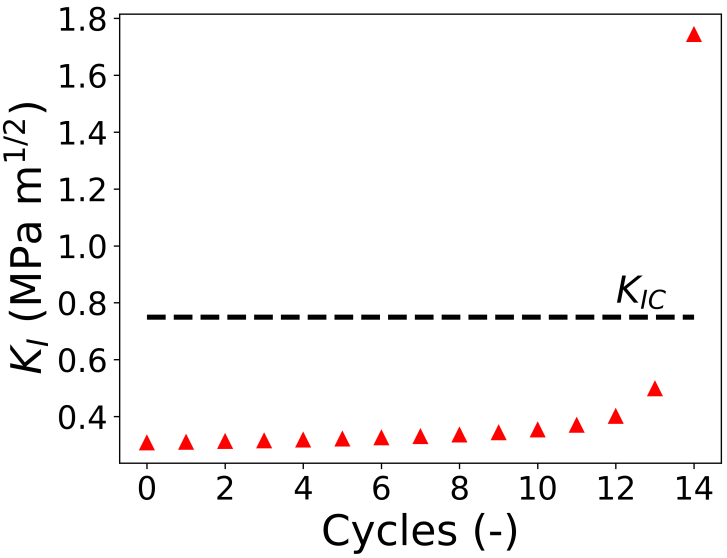

Fig. 4.7 Trend of the stress intensity factor K_I under cyclic loading in the presence of both static and dynamic fatigue: initial depth of the critical surface flaw $a_\mathrm{cr} = 9.62$ μm, mean stress $\overline{\sigma} = 50$ MPa, stress amplitude $\Delta\sigma = 30$ MPa

Certainly, Eq. (4.2) can be applied only when the stress intensity factor overcome the threshold for sub-critical crack growth, $K_{\mathrm{I,th}}$, which can be assumed equal to 0.25 MPa m$^{1/2}$ as per [26]. The dimension of the initial surface flaw for which

sub-propagation does not occur can be calculated through Eq. (4.4), by substituting K_{IC} with $K_{I,th}$ and σ_f with the mean stress of the cyclic loading $\overline{\sigma} = 50$ MPa. It is obtained $a_{th} = 6.34\,\mu m$ for the present example. Therefore, in case the coating had not been applied, only the glass samples having $a_{cr} \leq a_{th} = 6.34\,\mu m$ would have survived to the cyclic loading.

In conclusion, besides being durable to cyclic loading, the coating can be used to derive the pure dynamic fatigue behaviour of glass.

4.3.3 Effect of natural weathering

Visible spectra analysis was performed on the naturally weathered coated samples in order to evaluate the transparency, one of the most peculiar and appreciated property of glass, also in structural applications. The percentage of transmittance of wavelengths in the range of visible light is shown in Fig. 4.8, where it is compared to those of un-coated glass and freshly coated glass. The transmittance is higher than 60% in the visible range for all the glass samples, which means that the transparency of glass, equal to about 90% in absence of coating, is sensibly reduced, but still remains above the value of the minimum acceptable glazing transmittance that, according to a study carried out by [89], falls within the range 25% to 38%.

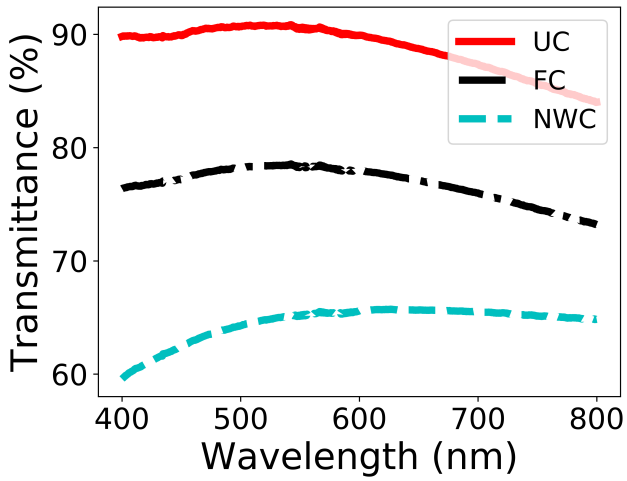

Fig. 4.8 Visible spectra of un-coated (UC), freshly coated (FC) and naturally weathered coated (NWC) glass samples

The wettability of the coated surface of the glass samples was estimated through water static contact angle measurements. As the contact angle of the droplets with the surface rises, the hydrophobicity increases [90]. The average water contact angles for un-coated glass, freshly coated glass and naturally weathered coated glass specimens are reported in Table 4.6. While the glass is quite wettable by water and shows a contact angle of 23.9° after a simplified cleaning protocol is applied on the tested surface, the freshly coated glass exhibits a contact angle of 103.2°: largely exceeding 90°, the value indicates that the surface is quite hydrophobic as expected by a gradient coating where the fluorine component is preferentially concentrated at the surface. After 510 days of natural weathering, the coating wettability increases and the contact angle value is found as low as 60°. This value is similar to that measured on a coating made of the pure resin without the addition of the fluorinated comonomer [58], thus it means that the surface composition has changed due to outdoor exposure. This is in agreement with recent studies assessing the rearrangements of polymers in dependence of the environment. When coatings containing a low amount of a fluorinated component are prepared and maintained in dry air, the fluorinated chains segregate at the coating surface, and assure hydrophobicity. When the coating is in contact with a polar solvent such as water, the fluorinated moieties can easily rearrange and cause an increase of wettability [91].

Table 4.6 Water static contact angles

Glass samples	θ_{water} (°)
un-coated glass	23.9 ± 1.8
freshly coated glass	103.2 ± 1.6
naturally weathered coated glass	60.0 ± 8.5

The Weibull diagrams for un-coated, freshly coated and naturally weathered coated glass specimens are shown in Fig. 4.9. The data points of naturally weathered coated specimens (light blue triangles) are well fitted by a Weibull distribution function having $\hat{\beta} = 3.63$ and $\hat{\theta} = 102.54$ MPa. Although the $\hat{\theta}$ value for naturally weathered coated samples is greater than that for un-coated samples and very close to that for freshly coated samples, the decrease of the $\hat{\beta}$ value has a quite negative effect, especially on the evaluation of the design bending strength, i.e. a characteristic value having a probability of failure lower than 5%. Our conjecture is that the decrease of $\hat{\beta}$ is again due to a variation of the critical defect size distribution, rather than a consequence of a reduced performance of the coating. In the latter case, in fact,

the Weibull curve should undergo a simple translation with respect to the reference ones, without any change in slope. Although the coating applied on the naturally weathered coated samples was not visibly damaged after weathering, hail and other contaminants impacts may have resulted in new and larger flaws on the surface of the glass samples [92, 93]. As a result, the dispersion of the defect population in naturally weathered coated glass increased, leading to a decrease in the $\hat{\beta}$ value.

A more consistent comparison should have been done with naturally weathered un-coated glass specimens, subjected to the same weathering conditions. Unfortunately, such a set of specimens was not included in the present study. However, for the sake of clarity, an hypothetical Weibull distribution for the bending strength of naturally weathered un-coated glass specimens is shown in Fig. 4.9 (dashed blue line). Given that naturally weathered un-coated and coated samples should have similar surface defect density and size, the two distributions have the same $\hat{\beta}$ value. The parameter $\hat{\theta}$ for the hypothetical distribution was determined by assuming that the naturally weathered un-coated and coated probability distributions are spaced apart as well as the un-coated and freshly coated distributions are. Under this hypothesis, the beneficial effect of the coating, also for low values of probability of failure, is evident.

4.3.4 Effect of artificial weathering

Figure 4.10 shows the ATR-FTIR spectra collected on the coating surface at different weathering time. All along the weathering process, there is a steady increase of the 3700-3100 cm^{-1} band (region A) and of the shoulder at 1640 cm^{-1} (region C): the signals are related to the vibrations of -OH groups and may indicate water adsorption onto the coating [94]. The broadening of the C=O peak in the 1850-1650 cm^{-1} region (region B) may be associated to oxidation phenomena, i.e. degradation of the coating in the presence of air under light. Interesting information can be gathered observing the doublet band at 1634 cm^{-1} and 1618 cm^{-1} (peaks D and E) and the band at 810 cm^{-1} (peak F) present for freshly coated glass and disappearing after one week of exposure. These signals are due to the double bond of the methacrylate group characterising the oligomer used for the preparation of the coating and subjected to curing through the double bonds' reaction. Therefore, the coating is not completely crosslinked at the end of the curing process (presence of the above-mentioned bands);

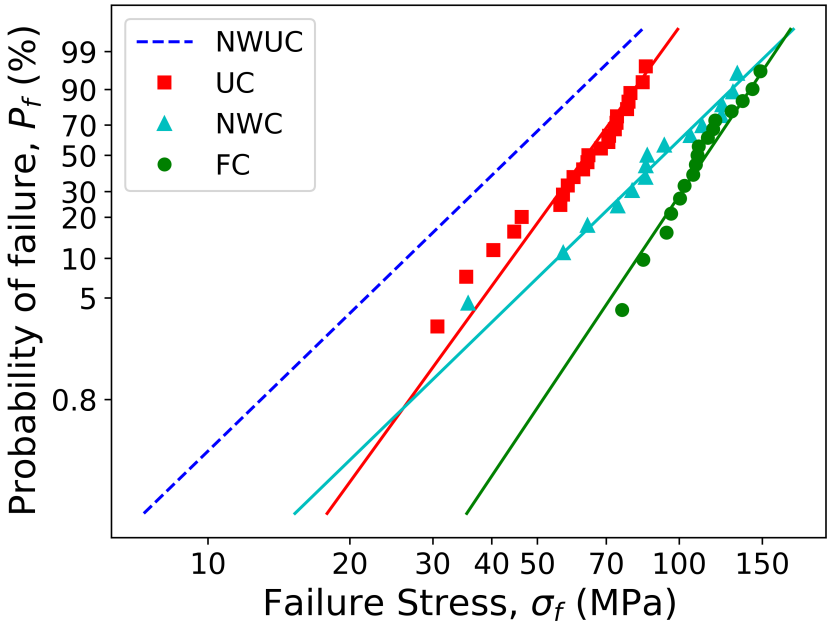

Fig. 4.9 Weibull distribution functions for the bending strength of un-coated (UC), freshly coated (FC), and naturally weathered coated (NWC) glass samples

while, after the first two ageing weeks, when these peaks disappear, the conversion is complete [58, 95].

As explained in Section 4.2.5, the specimens used to analyse the effects of artificial weathering had edge length $l = 75$ mm and thickness $h = 3$ mm, instead of 120 mm and 4 mm, respectively. A comparison with the probability of failure of specimens having $l = 120$ mm and $h = 4$ mm would have not been coherent and, therefore, a set of 18 un-coated specimens with size 75 mm was tested with the coaxial double ring setup. The Weibull diagrams for the bending strength of un-coated specimens having size of 75 mm and artificially weathered coated glass specimens are shown in Fig. 4.11. In order to highlight the aforementioned inconsistency between specimens of different size, the Weibull distribution function of un-coated specimens having $l = 120$ mm is also shown in Fig. 4.11 (red dashed line).

The parameters of the Weibull distribution functions that best fit the data points are: $\hat{\beta} = 3.0$ and $\hat{\theta} = 91.9$ MPa for artificially weathered coated specimens (gray triangles), $\hat{\beta} = 2.8$ and $\hat{\theta} = 67.5$ MPa for artificially weathered un-coated specimens (orange square). As shown in Fig. 4.11 the UC75 series rather follows a truncated

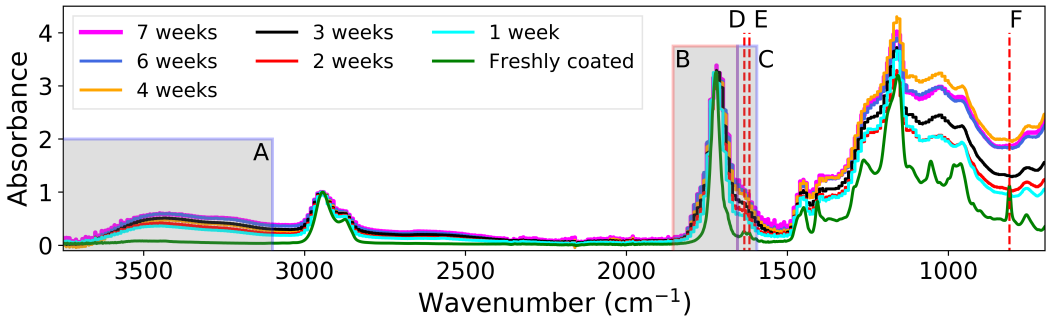

Fig. 4.10 FTIR-ATR spectra taken on the surface of freshly coated glass and coated glass that had been artificially weathered for 1, 2, 3, 4, 6, and 7 weeks.

Weibull function [78, 96], whereas the AWC series more likely follows a regular two parameter Weibull function. The increase of bending strength is evident, although it was quite unexpected after the initial visual inspection of the specimens, which revealed an almost complete detachment of the coating after seven weeks of exposure to artificial weathering (see Fig. 4.5). A plausible explanation is that the silane coupling agents used to improve the adhesion of the coating on the substrate reached the tips of the surface defects, increasing the hydrophobicity of the glass in the spots where the stress corrosion reaction can occur. The property of the silane to alter the wettability of glass by inducing the surface hydrophobicity has already been proven by several studies [58, 97, 98].

The statistical data of all the sets of specimens analysed in this study are reported in Tab. 4.7. They include, for each series of tests, the number of specimens that fractured in an acceptable way, the Weibull shape parameter $\hat{\beta}$, the Weibull scale parameter $\hat{\theta}$ and the coefficient of variation $\hat{CV}$.

Table 4.7 Statistical data of the experimental results

Id. code	Edge size (mm)	Type of samples	No. of valid samples	Weibull param. $\hat{\beta}$	Weibull param. $\hat{\theta}$ (MPa)	$\hat{CV}$ (%)
UC	120	un-coated	23	5.2	68.3	24.2
FC	120	freshly coated	17	5.6	121.8	17.7
CAC	120	cyclically aged coated	17	4.3	110.0	22.1
NWC	120	naturally weathered coated	15	3.6	102.5	31.0
UC75	75	un-coated	18	2.8	67.5	38.1
AWC	75	artificially weathered coated	13	3.0	91.9	35.6

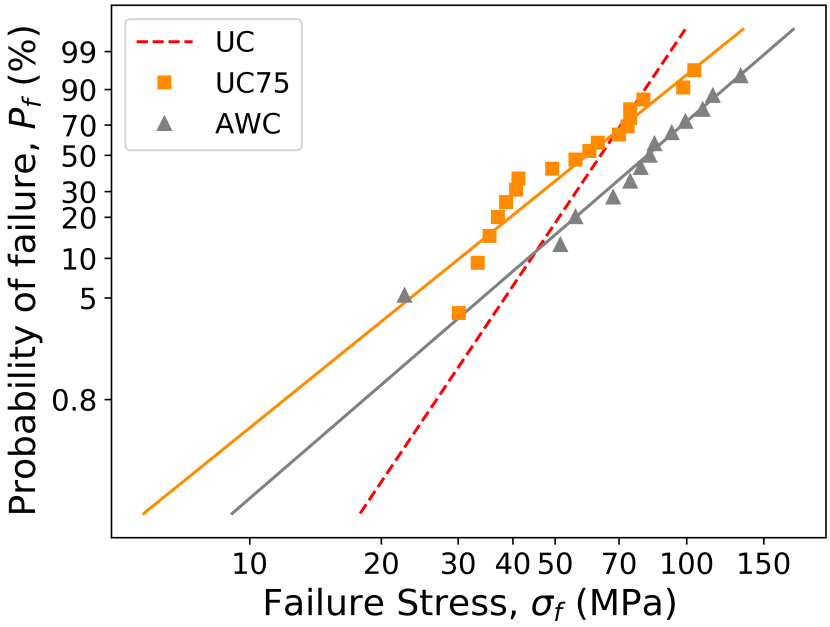

Fig. 4.11 Weibull distribution functions for the bending strength of artificially weathered coated glass samples (AWC) and un-coated glass samples (UC75) with edge size $l = 75$ mm

4.4 Conclusions

The durability of an UV-cured polymeric coating optimized to prevent glass stress corrosion has been examined. Concerning the cyclic loading, the coating resulted to be insensitive to repetitive loads, being its performance in preventing stress corrosion remained almost intact. However, the coating cannot hinder the dynamic fatigue taking place in case a sufficiently high level of stress is achieved at the tip of the surface flaws, as it was in the cyclic tests carried out in this study. The sub-critical growth of the critical surface flaws by fatigue has been evidenced by a reduction of the $\hat{\beta}$ parameter of the Weibull distribution for the bending strength, which, therefore, is not related to a reduced performance of the coating.

The natural weathering had its main effect on the optical properties of the coating, in the sense that it caused a reduction of the transparency, although it remained on acceptable values. On the other hand, the effectiveness of the coating in preventing stress corrosion was almost fully preserved. Also in this case, the reduction of the $\hat{\beta}$ parameter of the Weibull distribution for the bending strength has to be associated

to a variation in the distribution of the critical defect size due to the impact of hail stones and other particles.

Finally, the effect of the artificial weathering on the durability of the coating is more pronounced. There was no evidence of damage in the coating until five weeks of exposure, whereas it was almost completely detached after seven weeks of exposure. It has to be remarked that the conditions applied for the artificial weathering were very severe in terms of temperature, humidity and UV-light. Nevertheless, a not-negligible residual capacity to prevent stress corrosion was observed. A possible explanation is that the silane used to pre-treat the surface of the glass reached the tips of the surface defects, increasing the hydrophobicity of the glass in the spots where the stress corrosion reaction might occur.

In conclusion, even though only the application on the air side has been investigated so far and slight modifications in the formulation of the coating can be brought to further improve its durability, the current formulation has already shown a very good performance, which makes it very promising for future practical applications. Further studies will be carried out to assess the resistance of the coating to abrasions and scratches, to better evaluate its optical band gap, and to analyse its performance when applied on the cut edges of glass plates.

Chapter 5

A probabilistic FEM approach for structural integrity assessment of glass components

5.1 Introduction

The fracture stress of glass varies widely between 20 and 200 MPa [30], depending on a variety of factors such as the load history [99], the surface condition (new or weathered glass) [100], the element's size [101], the environmental conditions [102], the point of the origin of failure (on the edge or on the surface), the type of edge processing [103, 104]. Griffith flaws cause the brittle failure in glass [23], their random distribution results in a large scatter in fracture strength and location. Flaws and scratches occur during the manufacturing process, as well as during handling, assembly, everyday use and maintenance [24]. As a result, not only across plates from various production batches, but even within the same batch, flaw characteristics and failure stress magnitudes vary dramatically. The glass flaws typically range from 20 μm to 200 μm [105]. However, accidental impacts or vandalism might result in more serious damage and much deeper flaws in glass components.

Despite the strong scattering of the glass strength, several design methods for structural glass components have been proposed. They can be divided into two groups for simplicity: the method adopted in the European design standards and that used in the North American design standards.

The European standards EN16612:2019 [4] and CEN/TS 19100-1:2021 [31] are based on the deterministic design approach, for which the structural integrity is assessed by comparing the maximum bending stress, σ_{max}, with a design value of bending strength $f_{g;d}$:

$$\sigma_{max} \leq f_{g;d} \tag{5.1}$$

According to EN16612:2019 [4], for annealed glass of any composition, the design value of bending strength is:

$$f_{g;d} = \frac{k_e k_{mod} k_{sp} f_{g;k}}{\gamma_{M;A}} \tag{5.2}$$

where $f_{g;k} = 45$MPa is the characteristic value of the bending strength for annealed glass (5% fractile) ; $\gamma_{M;A}$ is the material partial factor that ranges from 1.6 to 1.8; k_e, k_{sp} and k_{mod} are the strength reduction factors. k_e and k_{sp} take into account the edge and surface finishing, while k_{mod} the load duration. An experimental campaign, involving 741 panes of 6 mm float glass, was conducted according to EN 1288-2 [71] to provide the characteristic glass strength $f_{g;k}$ [4]. The 741 failure stress measurements σ_f were treated statistically, and the $f_{g;k}$ value was derived using the two-parameters Weibull distribution for a probability of failure P_f = 5%, as shown in Fig. 5.1. The sampling distribution is clearly non-linear, indicating that it does not fit a Weibull distribution well. As a result, the confidence intervals of the Weibull parameters are rather broad, and the prediction of extremely low risk levels is uncertain [4].

The deterministic approach is widely used mostly because of its outstanding simplicity, but it has some drawbacks. The first weakness is that it relies on the glass strength parameter which is not a true material property, as it depends on the flaws size distribution, the fracture toughness, the test setup, as well as the specimen size and geometry [34]. Secondly, when using a deterministic approach, large safety factors need to be introduced for a safe design. However, it is worth noticing that a high safety factor does not necessarily imply a low level of risk, as its influence might be offset by the presence of greater uncertainties in the design environment [106]. In addition, the stress-based design approach assumes that the point of origin of failure coincides with the point of maximum stress, condition that rarely happens in glass [27]. Because of the large scatter in fracture strength and failure origin, a probabilistic approach should be adopted for the design and structural optimization of

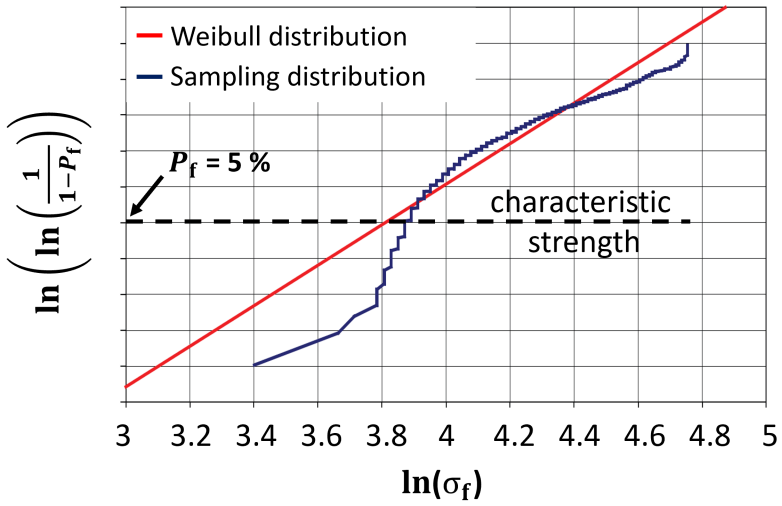

Fig. 5.1 Cumulative Weibull distribution of the failure stress. Adapted from EN16612:2019 [4]

glass components. Recently, the semi-probabilistic (level I) method for the design of glass components has been enhanced in reliability by some studies. As for example, the findings by Ballarini *et al.* [96] have contributed to reduce with confidence the partial safety factors for the structural design of glass by using a generalized distribution of the Weibull type. However, the obtained results are restricted to be used when the maximum tensile stress acts far from the edges. In addition, the findings by Lamela *et al.* [107] showed that the Weibull distribution functions of the glass strength are quite similar under different types of testing. In particular, for annealed glass the shape parameter of the Weibull distribution function takes approximate values to 4.

The American National Standard 'Standard Practice for Determining Load Resistance of Glass in Buildings' ASTM E1300-16 [5] adopts the glass failure prediction model proposed by Beason and Morgan [108, 109] for the prediction of the load-carrying capacity of glass components. ASTM E1300-16 only applies to vertical and sloped glazing of rectangular shape exposed to a uniform lateral load, such as wind load, snow load and self-weight with a total combined magnitude less than or equal to 10 kPa. The standard shall not apply to other applications including, balustrades, glass floor panels, aquariums, structural glass members and glass shelves. Unlike in the European design methods, the structural integrity assessment is based on loads rather than stresses. In fact, the structural integrity in ASTM E1300-16 is evaluated by comparing the uniform lateral load q with the load resistance LR which is the

load associated with a breakage probability less than or equal to 0.8%:

$$q \leq LR = NFL \cdot GTF \tag{5.3}$$

being NFL the non-factored load and GTF the glass type factor. While the GTF factors are listed in tables in which the glass type and the load duration are considered, the NFL values can be obtained by the charts reported in ASTM E1300-16. For a sake of clarity, one of the non-factored load charts is presented in Fig. 5.2. The

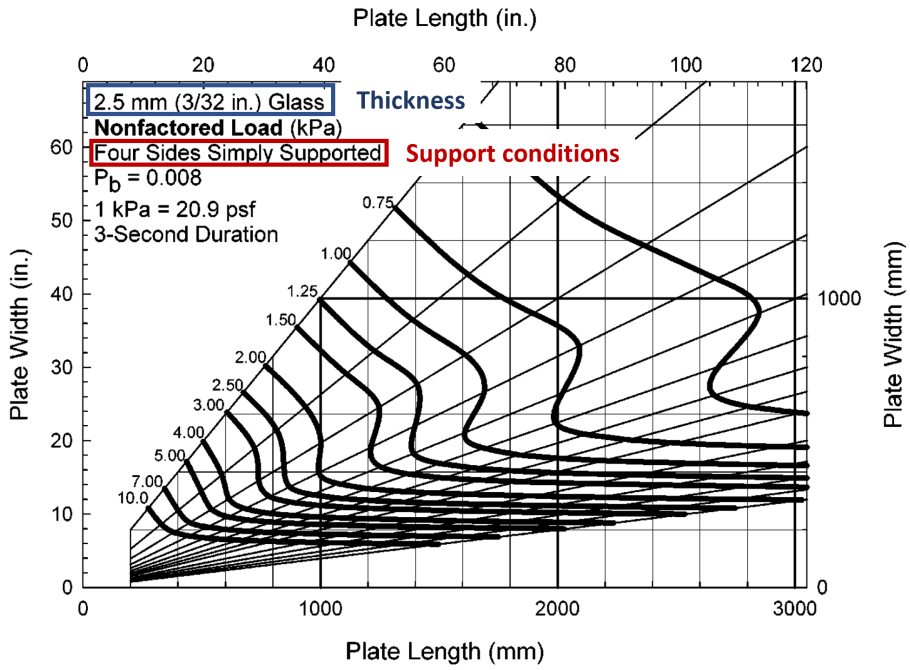

Fig. 5.2 Non-factored load chart. Adapted from [5]

NFL parameter is obtained for a load duration of 3 s and depends on the support conditions, as well as the plate size and thickness. The NFL charts were developed using the glass failure prediction model of Beason and Morgan [108, 109], who used the Weibull statistics [110] to represent the probability of failure P_{f} for glass:

$$P_{\mathrm{f}} = 1 - e^{-B} \tag{5.4}$$

According to Beason and Morgan [109], B reflects the risk of failure, and depends on the magnitude and duration of the surface tensile stresses in the plate, the surface area of the plate exposed to tensile stress, and the geometries and orientations of the

surface flaws. For general cases, B is written as follows:

$$B = \breve{k} \int_A \left[\breve{c}\sigma_{\text{eq,max}}(q,x,y)\right]^{\breve{m}} \mathrm{d}A \tag{5.5}$$

where $\sigma_{\text{eq,max}}(q,x,y)$ is the maximum equivalent principal stress as a function of the lateral load q and the coordinates (x,y) of the point on the glass surface; $\breve{c}$ is the 'biaxial stress correction factors' which is a function of the minimum to maximum principal stress ratio; A is the surface area of the plate; $\breve{k}$ and $\breve{m}$ are the so called 'surface flaw parameters' which reflect the character of glass plate surface flaws. The non-factor load NFL can be obtained by Eq. (5.4) once the probability of failure, the support and load conditions, the plate size and thickness, and the surface flaw parameters $\breve{k}$ and $\breve{m}$ have been defined. In ASTM E1300-16 it was assumed that $\breve{m}$ is equal to 7 and $\breve{k}$ is equal to 2.86×10^{-53} $\mathrm{N}^{-7}\,\mathrm{m}^{12}$. These flaw parameters represent the surface strength of weathered window glass that has undergone in-service conditions for approximately 20 years [5]. The narrow range of application of the standard is due to the fact that the parameters $\breve{m}$ and $\breve{k}$ have been obtained, and therefore considered reliable, only for the case of vertical or sloped glazing in buildings. To summarize, in ASTM E1300-16 the load-carrying capacity of glass plates is evaluated taking into account the actual surface flaw condition and the effect of the plate's size, however, the acceptable probability of failure cannot be set, and the field of application is restricted to vertical and sloped glazing in buildings subjected to uniform lateral load.

Because of the narrow range of application of ASTM E1300 and the weaknesses of the deterministic approach, new models, more flexible and suitable to be applied for several load and support conditions, should be developed. These models should account for a variety of glass surface scenarios, so that severe surface cracking or specific surface conditions detected by quality control procedures may be included. A reliable and less conservative design method would reduce costs and emissions involved in manufacturing glass components. However, the models should be robust, intuitive and easy to use, with few parameters which had a clear physical meaning. Additionally, they should be based on the real physical mechanism determining the strength of glass, i.e. the micro-cracks distribution, which is independent of both the test configuration and the element size. For this reason, this distribution should be provided after the manufacturing process, and its evolution should be predicted and monitored during the storage, assembly, and service stages of glass. However,

additional efforts are needed in order to detect and measure the crack size along the edges and on the surface of glass components. Recently, some methods for the crack and scratch detection have been developed, such as those based on thermal stress-induced light scattering techniques [21] and deep learning techniques [22].

In addition, special attention should be paid to the edge flaw condition, since it is one of the main parameters influencing the strength of glass [111], with particular regard to in-plane loaded structural elements, such as glass beams and façade mullions. The edge strength is also relevant in the structural integrity assessment of secondary construction elements, such as windows, that may be subjected to significant tensile stress along the edges as result of thermal actions [112], and bolted connections which are subjected to stress amplifications along the hole's edge.

A new numerical methodology to assess the edge strength of annealed glass is proposed and tested in Chapters 5, 6 and 7. The method can be used on any flat glass component under in-plane static loads, and it adopts the stress intensity factor -based fracture criterion for the prediction of the failure load. This method assumes that edge cracks are Pareto distributed, and relies on the extended finite element method (XFEM) for the explicit introduction of cracks in computational models and calculation of the stress intensity factors at the tip of each crack. In addition, Monte Carlo simulation is used to obtain the probability density function of the failure load. The model takes into account the size effect on the glass strength and the interaction among cracks for the evaluation of the stress intensity factors, whereas it does not consider the stress corrosion effect.

5.2 State of the art

Glass is a brittle material that fails when the critical value of the stress intensity factor is achieved at the tip of any flaw. The achievement of the failure condition is determined by a complex interplay between the flaw-size distribution and internal stress distribution, such that the critical crack, i.e. the one having the maximum value of the stress intensity factor, is not always placed in the point exhibiting the maximum tensile stress. For a crack subjected to Mode I, the fracture criterion is expressed as follows:

$$K_{\mathrm{I}} = K_{\mathrm{IC}} \tag{5.6}$$

where K_{I} is the Stress Intensity Factor (SIF) and K_{IC} denotes the value of the critical stress intensity factor, also known as fracture toughness [113]. Unlike the bending strength $f_{g;k}$, K_{IC} is a material property, and its value for soda-lime glass is estimated to be around 0.75 MPa $\mathrm{m}^{1/2}$ [114].

Let us consider a deformable body with a crack of size a, and subjected to a remote uniform stress state σ_{yy} applied normally to the plane of the crack, as shown in Fig. 5.3. The relationship between the fracture toughness K_{IC}, the failure stress $\sigma_{yy,\mathrm{f}}$ and the crack size a is derived from the linear elastic fracture mechanics:

$$K_{\mathrm{IC}} = Y \sigma_{yy,\mathrm{f}} \sqrt{\pi a} \tag{5.7}$$

where Y is a positive dimensionless geometrical factor depending on the the aspect ratios of the structural element wherein the crack is placed, the location of the crack (inner or edge cracks), and the flaw shape. For instance, Y approaches 1.12 for isolated straight-fronted edge cracks, remotely applied tensile stress (i.e. $H/W \geq 2$), and very small crack length (i.e. $a/W \leq 0.03$), as results from the handbook by Tada *et al.* [115].

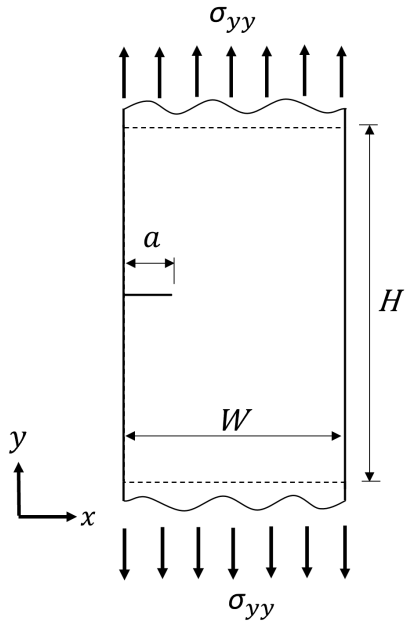

Fig. 5.3 Edge crack under Mode I loading

Yankelevsky [29] developed a numerical method to predict the surface strength of rectangular glass plates under bending for an arbitrary acceptable probability of

failure. To fully exploit the bending strength of the glass plate, Yankelevsky [29] included a flaws population on the plate's surface, from which the failure stress distribution could be derived. According to the method, the surface of the glass plate is divided into 1 cm^2 unit cells, and a crack is placed in each cell. The crack size a is chosen randomly from a truncated exponential probability distribution. Following, the failure stress $\sigma_{yy,f}$ on the plate side under tension is calculated according to Eq. (5.7) for each crack. As a result, the surface strength of a single plate is represented by the minimum failure stress. A Monte Carlo simulation should be run on a large sample of thousands of virtual specimens to acquire the probability distribution of both the point of origin of failure and the surface strength of annealed glass for arbitrary stress states.

Kinsella and Persson [20, 30] extended the method developed by Yankelevsky [29] to consider multiple flaw populations, arbitrary crack plane orientations and a mixed mode fracture criterion. Due to the results presented in literature works [116–118], Kinsella and Persson [20] adopted for their model the Pareto distribution to describe the statistical population of the depth of surface cracks. The same assumption has been done in the present study.

5.3 The FEM approach

As previously mentioned, the objective of this study is to provide a tool which is able to predict the edge strength of any annealed flat glass component, with arbitrary in-plane static load and support conditions. As the glass strength is highly sensitive to the presence of cracks, the approach is based on the critical stress intensity factor fracture criterion (Eq. (5.6)) and on probabilistic considerations. The procedure consists of the following four steps:

- Modelling the structural element through the finite element method (FEM);
- Randomly applying to the FE model a population of edge flaws, which is extracted from a pre-defined statistical distribution function;
- Computing the related stress-intensity factors;
- Evaluating the load carrying capacity by equating the maximum stress-intensity factor to the fracture toughness.

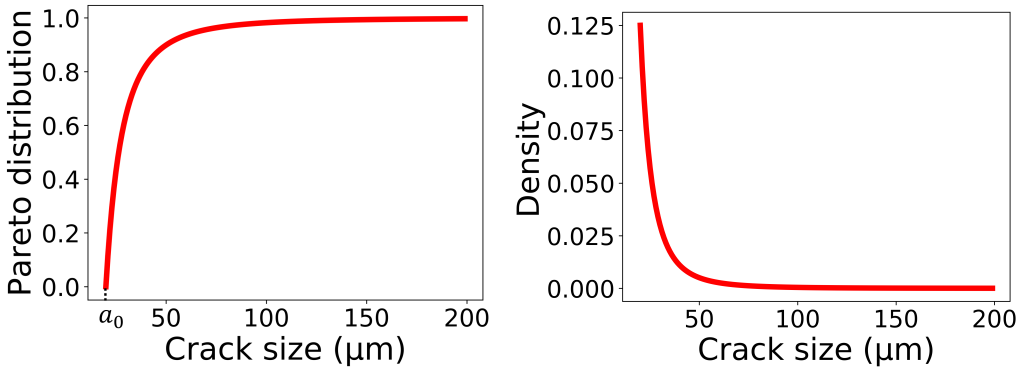

(a) (b)

Fig. 5.4 Pareto distribution: (a) cumulative distribution function (CDF); (b) probability density function (PDF)

Because of the stochastic nature of the problem, where the size of the edge flaws is the random variable, the Monte Carlo method must be used to obtain the distribution function of the failure load. Finally, the critical load referred to a chosen probability of failure can be derived.

5.4 Edge cracks and critical edge cracks distributions

The population of the size a of edge cracks can be realistically represented by a single Pareto distribution (Fig. 5.4a - CDF, Fig. 5.4b - PDF), that is described as [119]:

$$F(a) = 1 - \left(\frac{a_0}{a}\right)^c \tag{5.8}$$

with $a_0 \leq a < \infty$, $a_0 > 0$ and $c > 0$. c is the shape parameter, whilst a_0 is the scale parameter, which represents the smallest edge crack size.

Let us consider a glass plate subjected to uniaxial tensile loading, with just an edge crack of size a and no sub-critical crack growth (for example, see Fig. 5.3). The survival probability of the plate is expressed as the probability that the size a is smaller than the critical crack depth a_c:

$$P(a < a_c) = F(a_c) = 1 - \left(\frac{a_0}{a_c}\right)^c \tag{5.9}$$

Supposing that the glass plate has a random number i of isolated cracks, because a_c is constant for uniaxial tensile loading, the survival probability of the plate is the product of the survival probabilities of all cracks:

$$P(a < a_c) = \left[1 - \left(\frac{a_0}{a_c}\right)^c\right]^i \tag{5.10}$$

Considering that the real number of cracks x in glass plates follows a Poisson distribution with mean m [26]:

$$F(x) = \sum_{i=0}^{x} \frac{e^{-m} m^i}{i!} \tag{5.11}$$

the survival probability of a random glass plate is now obtained by multiplying the probability $F(x)$ from Eq. (5.11) by the survival probability from Eq. (5.10):

$$P(a < a_c) = \sum_{i=0}^{x} \frac{e^{-m} m^i}{i!} \left[1 - \left(\frac{a_0}{a_c}\right)^c\right]^i \tag{5.12}$$

For all possible numbers of cracks the survival probability is:

$$P(a < a_c) = \sum_{i=0}^{\infty} \frac{e^{-m}}{i!} \left\{m \left[1 - \left(\frac{a_0}{a_c}\right)^c\right]\right\}^i \tag{5.13}$$

Introducing the definition of the exponential function as an infinite series:

$$e^{\xi} = \sum_{i=0}^{\infty} \frac{1}{i!} \xi^i \tag{5.14}$$

the survival probability of a glass plate with average number of cracks equal to m becomes:

$$P(a < a_c) = F(a_c) = e^{-m a_0^c a_c^{-c}} \tag{5.15}$$

Finally, by substituting:

$$\lambda = m a_0^c \tag{5.16a}$$

$$\alpha = c \tag{5.16b}$$

in Eq. (5.15) yields the Fréchet cumulative distribution function of the critical edge crack size:

$$F(a_c) = e^{-\lambda a_c^{-\alpha}} \tag{5.17}$$

In the same way, Haldimann *et al.* [10] showed that the strength of glass under uniaxial tensile loading σ_f follows the Weibull distribution (Eq. (5.18)) if the cracks population is represented by a single Pareto distribution:

$$F(\sigma_f) = 1 - \exp\left[-\left(\frac{\sigma_\mathrm{f}}{\theta}\right)^{\beta}\right] \tag{5.18a}$$

$$\theta = \frac{K_{IC}}{m^{\frac{1}{\beta}} Y \sqrt{\pi}\sqrt{a_0}}, \quad \beta = 2c \tag{5.18b}$$

The Weibull parameters θ and β, for instance can be obtained by uniaxial tensile tests using small scale glass specimens. Once the parameters θ and β have been evaluated and the size of the smallest flaw a_0 has been assumed, the parameters m and c can be estimated by means of Eq. (5.18b). Finally, the average number of defects m and the size of the glass specimens can be used to calculate the density of the glass defects. The average number of cracks m and the shape parameter c are true material parameters unlike θ and β which depend on the test setup and the element size.

5.5 Crack modelling and stress intensity factor evaluation with XFEM

The extended finite element method (XFEM) was proposed by Belytschko *et al.* [40, 41] for modelling cracks and crack growth in the FE framework, with no remeshing. Karihaloo and Xiao [42] used the XFEM approach to determine the stress intensity factors at the crack tips directly without extra post-processing from the FEM formulation. The XFEM approach allows to introduce crack in FE models without using a mesh conforming with the crack as is the case with the traditional FEM. By using XFEM, as a first step, a standard FE mesh is realized for the problem without taking into account the crack. Following, cracks are introduced independently of the mesh by enriching the standard displacement approximation with both discontinuous displacement fields along the crack faces [120] and the asymptotic displacement fields at nodes surrounding the crack tips [121]. For clarity, illustrative sketches of a conforming FEM mesh and a nonconforming XFEM mesh for modelling cracks are presented in Fig. 5.5.

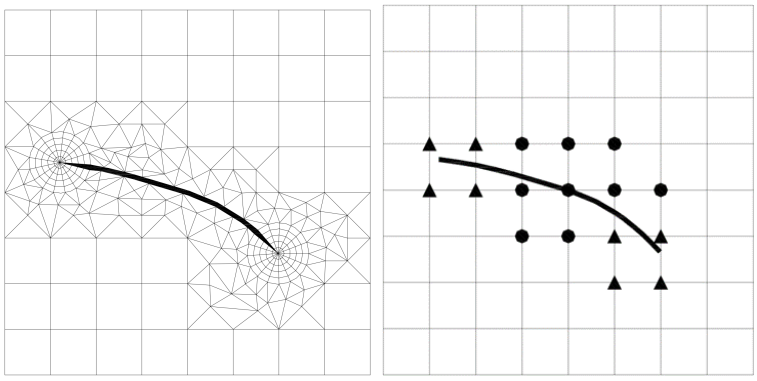

(a) (b)

Fig. 5.5 Illustrative sketches of (a) a conforming FEM mesh and (b) a nonconforming XFEM mesh for modelling cracks in the FE framework. The represented circular nodes are enriched with the discontinuous displacement fields, while the triangular nodes are enriched with the asymptotic displacement fields. Adapted from [6]

Let us consider a deformable body with volume Ω and external boundary Γ as shown in Fig. 5.6, in which Γ_t, Γ_u, Γ_c stand for the traction, displacement and crack boundaries, respectively. The virtual work equation can be written as [122]:

$$\int_{\Omega} \delta\boldsymbol{\epsilon}^{\mathrm{T}}\boldsymbol{\sigma}\,\mathrm{d}\Omega = \int_{\Omega} \delta\mathbf{u}^{\mathrm{T}}\mathbf{b}\,\mathrm{d}\Omega + \int_{\Gamma_t} \delta\mathbf{u}^{\mathrm{T}}\mathbf{t}\,\mathrm{d}\Gamma \tag{5.19}$$

where $\boldsymbol{\sigma}$ is the stress tensor, $\mathbf{b}$ is the body force vector, $\mathbf{t}$ is the external traction vector, $\delta\boldsymbol{\epsilon}$ and $\delta\mathbf{u}$ are the virtual strain tensor and displacement field, respectively.

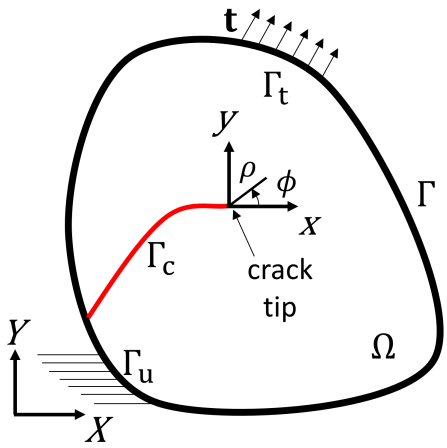

Fig. 5.6 An edge-cracked body under prescribed boundary tractions and displacements

For the discretized cracked body, the displacement field **u** far from the crack can be approximated by the interpolation of the displacements at each node:

$$\begin{Bmatrix} u(X,Y) \\ v(X,Y) \end{Bmatrix} = \sum_{i \in I} N_i \begin{Bmatrix} u_{0i} \\ v_{0i} \end{Bmatrix} \tag{5.20}$$

while, close to the crack tip and along the crack face, the standard local displacement approximation can be enriched with the asymptotic crack tip displacement fields [121], which are discontinuous along the crack face, as shown in Fig. 5.7:

$$\begin{Bmatrix} u(X,Y) \\ v(X,Y) \end{Bmatrix} = \sum_{i \in I} N_i \begin{Bmatrix} u_{0i} \\ v_{0i} \end{Bmatrix} + \sum_{j \in J_k \cap I} N_j \begin{Bmatrix} u_j^{(tip\,k)} \\ v_j^{(tip\,k)} \end{Bmatrix} \tag{5.21}$$

where I is the set of all nodes in the element, (u_{0i}, v_{0i}) are the standard degrees of freedom at node i, N_i and N_j are the finite element shape functions associated with node i or j. J_k is the set of nodes that are enriched around the crack tip k and along the crack face. $(u_j^{(tip\,k)}, v_j^{(tip\,k)})$ are the asymptotic displacement fields at node j for the crack tip k.

A general form of the displacement expansions (truncated to the 1^{th} term) near the fracture tip, excluding the rigid body modes, can be described as follows for a mixed mode crack in a homogeneous, isotropic material [121]:

$$\begin{Bmatrix} u_j^{(tip\,k)} \\ v_j^{(tip\,k)} \end{Bmatrix} = \begin{bmatrix} f_{11} & f_{12} \\ f_{21} & f_{22} \end{bmatrix} \begin{Bmatrix} K_{\mathrm{I}j}^{(tip\,k)} \\ K_{\mathrm{II}j}^{(tip\,k)} \end{Bmatrix} \tag{5.22}$$

where $K_{\mathrm{I}j}$ and $K_{\mathrm{II}j}$ are the Mode I and Mode II stress intensity factors at node j, while f_{11}, f_{12}, f_{21} and f_{22} are the angular functions whose explicit expressions with respect to the polar coordinate system (ρ, ϕ) centered at the crack tip (see Fig. 5.6) are listed below:

$$\begin{Bmatrix} f11 \\ f12 \\ f21 \\ f22 \end{Bmatrix} = \frac{\rho^{1/2}}{2\mu\sqrt{2\pi}} \begin{Bmatrix} (\kappa - \frac{1}{2})\cos\frac{\phi}{2} - \frac{1}{2}\cos\left(-\frac{3}{2}\phi\right) \\ (\kappa + \frac{3}{2})\sin\frac{\phi}{2} - \frac{1}{2}\sin\left(-\frac{3}{2}\phi\right) \\ (\kappa + \frac{1}{2})\sin\frac{\phi}{2} + \frac{1}{2}\sin\left(-\frac{3}{2}\phi\right) \\ -(\kappa - \frac{3}{2})\cos\frac{\phi}{2} - \frac{1}{2}\cos\left(-\frac{3}{2}\phi\right) \end{Bmatrix} \tag{5.23}$$

being μ and ν the shear modulus and Poisson's ratio of the material, and $\kappa = (3-4\nu)$ for plane strain or $\kappa = (3-\nu)/(1+\nu)$ for plane stress. The asymptotic displacement

fields $(u^{(tipk)}, v^{(tipk)})$ are discontinuous on the crack surface Γ_c. For the sake of example, the displacement $v^{(tipk)}$ along the y direction is plotted near the crack tip in Fig. 5.7.

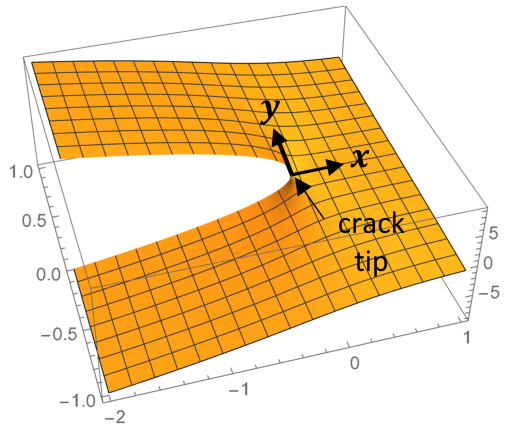

Fig. 5.7 Asymptotic crack tip displacement field $v^{(tipk)}$ close to the crack tip k centered at the origin of the coordinate system x, y

Inserting Eq. (5.22) into Eq. (5.21) yields:

$$\mathbf{u} = \begin{Bmatrix} u(X,Y) \\ v(X,Y) \end{Bmatrix} = \sum_{i \in I} N_i \begin{Bmatrix} u_{0i} \\ v_{0i} \end{Bmatrix} + \sum_{j \in J_k \cap I} N_j \begin{bmatrix} f_{11} & f_{12} \\ f_{21} & f_{22} \end{bmatrix} \begin{Bmatrix} K_{\mathrm{I}j}^{(tipk)} \\ K_{\mathrm{II}j}^{(tipk)} \end{Bmatrix} = \mathbf{Na} \tag{5.24}$$

Using the definition of strain:

$$\boldsymbol{\epsilon} = \begin{Bmatrix} \varepsilon_X \\ \varepsilon_Y \\ \gamma_{XY} \end{Bmatrix} = \begin{bmatrix} \partial/\partial X & 0 \\ 0 & \partial/\partial Y \\ \partial/\partial Y & \partial/\partial X \end{bmatrix} \begin{Bmatrix} u(X,Y) \\ v(X,Y) \end{Bmatrix} = \mathbf{SNa} = \mathbf{Ba} \tag{5.25}$$

and that of stress:

$$\boldsymbol{\sigma} = \mathbf{D}\boldsymbol{\epsilon} \tag{5.26}$$

and substituting Eqs. (5.24), (5.25), (5.26) into Eq. (5.19) yield a system of linear equations:

$$\int_\Omega \mathbf{B}^{\mathrm{T}}\mathbf{DB}\,\mathrm{d}\Omega\,\mathbf{a} = \int_\Omega \mathbf{N}^{\mathrm{T}}\mathbf{b}\,\mathrm{d}\Omega + \int_{\Gamma_t} \mathbf{N}^{\mathrm{T}}\mathbf{t}\,\mathrm{d}\Gamma \tag{5.27}$$

where the **B** matrix contains the derivatives of the shape functions N_i for the finite elements whose nodes are not enriched:

$$\mathbf{B}_i^u = \begin{bmatrix} N_{i,X} & 0 \\ 0 & N_{i,Y} \\ N_{i,Y} & N_{i,X} \end{bmatrix} \tag{5.28}$$

whereas, for the finite elements whose nodes are in the interval J_k, **B** is composed by the standard part $\mathbf{B}^u$ and the enriched one $\mathbf{B}^K$, that is defined as:

$$\mathbf{B}_i^K = \begin{bmatrix} (N_i f_{11})_{,X} & (N_i f_{12})_{,X} \\ (N_i f_{21})_{,Y} & (N_i f_{22})_{,Y} \\ (N_i f_{11})_{,Y} + (N_i f_{21})_{,X} & (N_i f_{12})_{,Y} + (N_i f_{22})_{,X} \end{bmatrix} \tag{5.29}$$

Eq. (5.27) can be written as:

$$\mathbf{a} = \mathbf{K}^{-1}\mathbf{f} \tag{5.30}$$

being **a** the vector of the standard and enriched nodal degrees of freedom, **K** the stiffness matrix, and **f** the external force vector. As a consequence, both $K_{\mathrm{I}j}^{(tipk)}$ and $K_{\mathrm{II}j}^{(tipk)}$ are calculated directly without extra post-processing for each node j within the interval J_k by solving the system of Eq. (5.30).

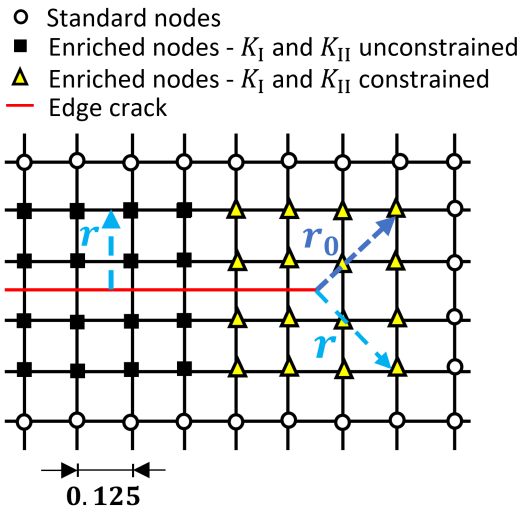

Fig. 5.8 Edge crack on a uniform mesh. The squared and triangular nodes are enriched by the crack tip functions

The extended finite element method has been implemented within the *X3D* FORTRAN finite element code by Benvenuti *et al.* [123, 124]. In addition, *X3D* code has recently been extended by the author to manage multi-cracks and to perform Monte Carlo simulations. In the developed code, the enriched nodes within the interval J_k are defined by means of an enrichment radius r from the crack interface as shown in Fig. 5.8. Furthermore, Liu *et al.* [121] showed that by enriching several layers of nodes around the crack tip, the XFEM solution improves. As a result, more than one layer of nodes surrounding each crack tip is enriched in this study, as shown in Fig. 5.8. As in Reference [121], in order to guarantee the convergence of the numerical solution, a penalty method is employed in *X3D* code such that constrains are enforced on the enriched degrees of freedom. In particular, for each $j-$th enriched node located in the circular region centred at the $k-$th crack tip with radius r_0 (see Fig. 5.8), the system of linear equations (Eq. (5.30)) is forced to return the same value of the stress intensity factor. As a consequence, for each crack tip, a single value of K_{I} and K_{II} is provided. r_0 should be quite small, including solely the nodes closest to the crack tips where the asymptotic fields are expected to dominate the solution.

The procedure has been implemented for 4-node quadrilateral elements. In order to ensure that the stiffness matrix (left-hand side of Eq. (5.27)) is adequately integrated, standard second order Gauss-Legendre quadrature is used in the elements not containing any enriched node, while high order Gauss quadratures (8×8 or 20×20 Gauss points) are used over the finite elements whose nodes are enriched. In fact, since the displacement field over the enriched elements (Eq. (5.24)) is approximated with angular functions (Eq. (5.23)), the stiffness matrix terms are not polynomial. As a result, for any quadrature order, the Gauss-Legendre quadrature will never return the exact value of the integral. The approximation error can be reduced by increasing the number of Gauss points, but it cannot be eliminated.

5.6 Monte Carlo simulation

In order to build the curves of the cumulative distribution function and density function of the failure load of a glass element, Monte Carlo simulation is performed. For thousands of virtual specimens, which are identical in their geometry and boundary conditions, the failure load is calculated.

The length of the cracks varies within a specimen and among specimens, the locations of the cracks, on the other hand, are established at the start of the simulations and stay fixed in the XFEM model. The stress intensity factor $K_{\mathrm{I}}^{(tip\,k)}$ is computed for each crack tip k in each simulation, and the failure load is recorded when K_{I} reaches the fracture toughness value K_{IC} for one of the edge cracks. The failure load is determined for a total of 5,000 virtual specimens in this study, because Yankelevsky [29] showed that the choice of 5,000 specimens assures a reliable convergence and repeatable results; while, a smaller sample may yield different results.

The edge crack lengths can be computed by Eq. (5.8), once the parameters a_0 and c and the value of the probability $0 \leq F(a) < 1$ have been set. A random number generator is employed to provide values for $F(a)$ and to obtain random edge crack lengths which are Pareto distributed. In particular, RANDOM_NUMBER(x) is the FORTRAN function which has been used in *X3D* code. RANDOM_NUMBER returns a single pseudorandom number from the uniform distribution over the range $0 \leq x < 1$.

5.7 Conclusions

A new numerical methodology has been proposed for the structural integrity assessment of glass components. The approach is based on the critical stress intensity factor fracture criterion and on probabilistic considerations. In particular, according to the developed approach, the Griffith flaws, whose size is extracted from a pre-defined statistical distribution, are included within the FE mesh, and the stress intensity factor is then calculated for each flaw by means of the extended finite element method. As a consequence, the load carrying capacity can be evaluated by equating the maximum stress-intensity factor to the fracture toughness. Because of the stochastic nature of the problem, where the size of the flaws is the random variable, the Monte Carlo method is used to obtain the probability density function of the failure load. Finally, the critical load referred to a chosen probability of failure can be derived.

The XFEM formulation was adopted because it allows for a direct evaluation of the stress intensity factors without any post-processing. In addition, unlike the standard FEM, it enables the modelling of an arbitrary number of cracks in any position without the need for local mesh refinement, since the cracks are introduced mathematically, rather than physically, by enriching the standard approximation of

the displacement field. Because a coarse mesh can be adopted along the crack path and at the crack tip, the computational costs are drastically reduced by using XFEM. This is particularly useful when a large number of time-consuming FEM simulations have to be conducted to obtain the statistical distribution of the failure load.

The accuracy of the developed XFEM-based methodology will be assessed using a number of examples in Chapter 6, taking into account the effect of the mesh size, the enrichment radius, the inclination of the cracks, the number of Gauss Points, the stress concentration, and the cracks interaction on the evaluation of the stress intensity factors. In Chapter 7, examples of structural integrity assessment using the provided approach will be presented. The differences between the stress-based design approach and the proposed probabilistic one will also be highlighted, by solving case studies with different boundary and loading conditions.

Chapter 6

Accuracy and reliability of the developed XFEM-based methodology

6.1 Introduction

In this Chapter, several examples are solved to evaluate the accuracy and reliability of the method in assessing the K_{I} and K_{II} values at the crack tips. Different scenarios are investigated. Section 6.2 deals with a single edge notched tension specimen with an angled-crack, aiming to study the influence of the crack inclination angle and the number of Gauss points on the evaluation of K_{I} and K_{II}. In Section 6.3 the accuracy of the XFEM technique in predicting stress intensity factors for micro-cracks using a coarse mesh is assessed. In particular, K_{I} values are calculated for different crack lengths in order to identify the minimum crack length with respect to the mesh size and enrichment radius. Section 6.4 focuses on the effectiveness of the method in evaluating the stress intensity factor of cracks located near stress concentration regions. Finally, in Section 6.5 the reliability of the method in the case of interactive multiple edge cracks is illustrated.

6.2 Single edge notched tension specimen with an angled-crack

The problem under consideration is a single edge notched tension specimen as shown in Fig. 6.1. The specimen length is $L = 20$ units, the width is $W = 10$ units, the thickness is $th = 1$ unit, a is the crack length and ω is the crack inclination angle, $\omega = 0^\circ$ denotes pure mode-I cracking. The material is assumed to be linear elastic isotropic, and the problem is idealized as 2D plane stress. The Young's modulus is chosen as $E = 1$ unit, while the Poisson ratio as $\nu = 0.3$. The bottom edge is fixed in the vertical direction and to prevent rigid body motion, the bottom left node is fixed in the horizontal direction. A uniform stress $\sigma = 1$ unit is applied at the top edge of the specimen. 2D quadrilateral elements are used to mesh the solid model, with an edge size set to 0.125 units.

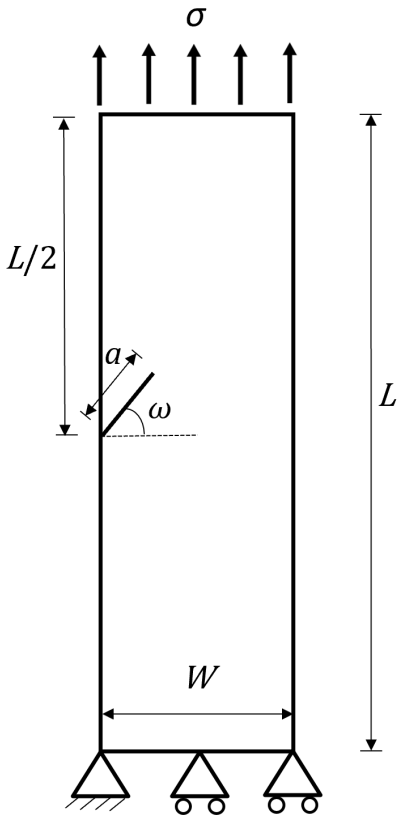

Fig. 6.1 Sketch of the cracked plate under tension

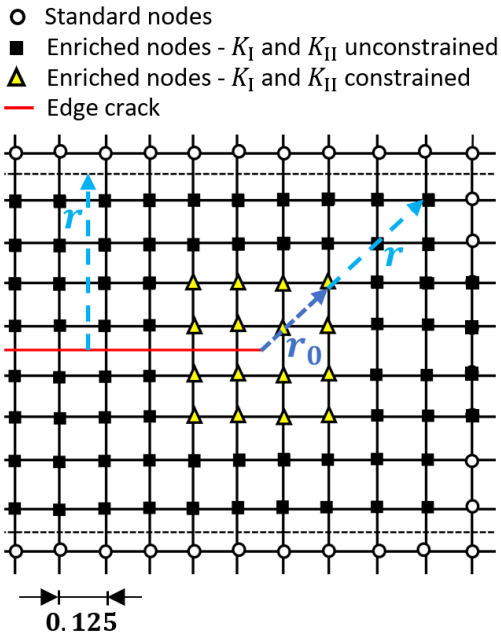

Fig. 6.2 Enriched nodes around the crack. The squared and triangular nodes are enriched by the crack tip functions, at the triangular nodes the stress intensity factor is forced to stay constant

The stress intensity factor is calculated at the crack tip for different crack lengths and for $\omega = 0°$ and $\omega = 45°$. The numerical integration over the enriched finite elements is performed using both 8×8 and 20×20 Gauss points (GP) in the case of $\omega = 45°$, whereas for $\omega = 0°$, only the 8×8 Gauss quadrature rule is adopted. The enriched elements are those whose four nodes are less than or equal to $r = 0.55$ units from the crack path, as shown in Fig. 6.2. However, the stress intensity factor values, returned by the *X3D* code, are those related to the enriched nodes within the radius of $r_0 = 0.27$ units from the crack tip, i.e. the triangular nodes in Fig. 6.2. At the triangular nodes the variables K_I and K_{II} are constrained to remain constant.

The resulting K_I values for $\omega = 0°$ are reported in Tab. 6.1, together with those obtained numerically using finite element analysis by Albinmousa *et al.* [125]. While, Tabs. 6.2 and 6.3 list respectively the K_I and K_{II} values for $\omega = 45°$, both calculated with the *X3D* code and according to Albinmousa *et al.* [125]. In the tables, the error is computed as:

$$Error = \frac{K_{I,X3D} - K_{I,Reference}}{K_{I,Reference}} \tag{6.1}$$

The plots of the ratio between the calculated solutions and the reference solutions are shown in Figs. 6.3 and 6.4. It can be seen that when $\omega = 0^\circ$, an excellent agreement with the reference solution is maintained for the entire range considered for the crack length a. On the contrary, for $\omega = 45^\circ$ differences are observed between the estimated and reference solutions, especially for small crack sizes (see Fig. 6.4). However, the accuracy of the solution improves as the number of Gauss points increases.

The enrichment functions reported in Eq. (5.23), associated with the presence of cracks, bring a non polynomial characteristic to the integrands of the stiffness matrix of the XFEM problem. Thus, the standard Gauss quadrature rule is no longer suitable and therefore a number of quadrature techniques were developed to numerically integrate the weak form over elements cut by crack surfaces [126, 127, 120, 128, 129]. However, the use of a high order quadrature (8×8 GP) results effective in the case of $\omega = 0^\circ$. It is important to remark that what matters is the inclination of the crack with respect to the mesh orientation instead of the inclination with respect to the specimen geometry. When $\omega = 0^\circ$, the crack is parallel to one of the side of the finite element, while if $\omega = 45^\circ$ the crack is inclined with regard to the sides of the finite elements, resulting in the increase of the complexity of the mathematical expressions of the integrands of the stiffness matrix, which are far from polynomial.

Table 6.1 Results for K_I of a horizontal edge crack ($\omega = 0^\circ$) in an isotropic elastic plate under tension - 8×8 Gauss Points

a	$K_{\mathrm{I,X3D}}$	$K_{\mathrm{I,Reference}}$ [125]	$Error$ (%)
0.25	0.94	0.97	-2.7
0.5	1.35	1.4	-3.8
1	2.04	2.10	-2.7
2	3.40	3.44	-1.1
4	7.61	7.46	+1.9
5	11.50	11.15	+3.2

Table 6.2 Results for K_{I} of an inclined edge crack ($\omega = 45^{\circ}$) in an isotropic elastic plate under tension

	8×8 Gauss Points		20×20 Gauss Points		
a	$K_{\mathrm{I,X3D}}$	$Error\ (\%)$	$K_{\mathrm{I,X3D}}$	$Error\ (\%)$	$K_{\mathrm{I,Reference}}$ [125]
0.25	0.74	+22.2	0.68	+12.8	0.60
0.5	0.97	+11.9	0.96	+10.3	0.87
1	1.37	+7.4	1.36	+6.3	1.28
2	2.06	+3.7	2.02	+1.9	1.98
4	3.81	+5.6	3.79	+5.0	3.61
5	5.19	+9.4	5.12	+8.1	4.74

Table 6.3 Results for K_{II} of an inclined edge crack ($\omega = 45^{\circ}$) in an isotropic elastic plate under tension

	8×8 Gauss Points		20×20 Gauss Points		
a	$K_{\mathrm{II,X3D}}$	$Error\ (\%)$	$K_{\mathrm{II,X3D}}$	$Error\ (\%)$	$K_{\mathrm{II,Reference}}$ [125]
0.25	0.15	-51.9	0.25	-19.5	0.31
0.5	0.36	-19.8	0.36	-17.6	0.44
1	0.58	-11.1	0.57	-11.7	0.65
2	0.95	-5.2	0.92	-7.9	0.99
4	1.72	-2.7	1.70	-3.4	1.76
5	2.22	-2.0	2.20	-2.7	2.26

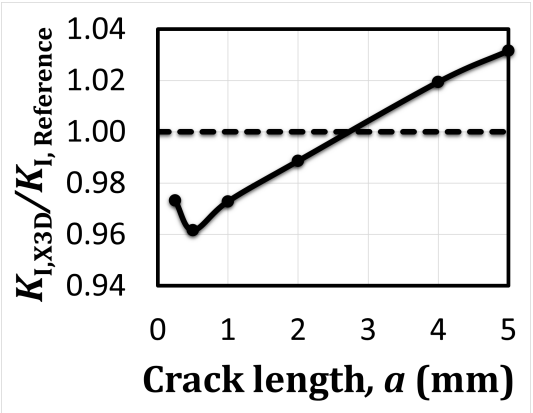

Fig. 6.3 $K_{\mathrm{I,X3D}}/K_{\mathrm{I,Reference}}$ ratio for a horizontal edge crack ($\omega = 0^{\circ}$) in an isotropic elastic plate under tension

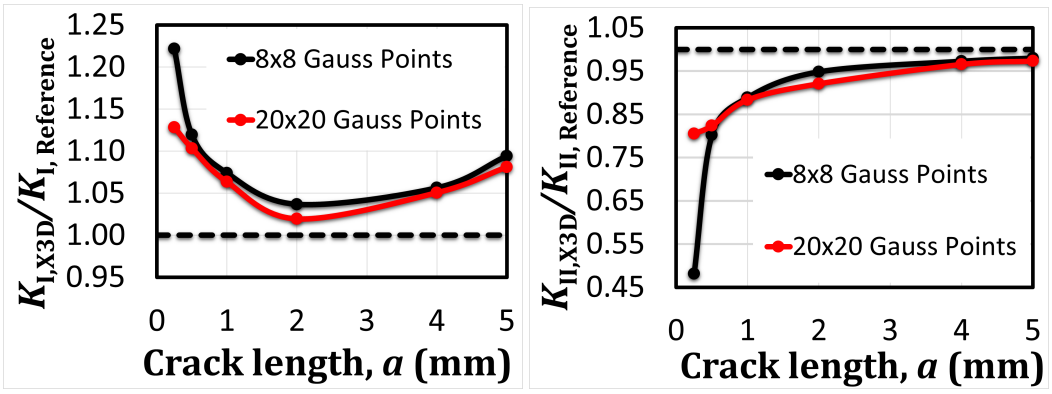

(a) (b)

Fig. 6.4 Ratio between the estimated stress intensity factor and the reference one for an inclined edge crack ($\omega = 45°$) in an isotropic elastic plate under tension: (a) $K_{\mathrm{I,X3D}}/K_{\mathrm{I,Reference}}$; (b) $K_{\mathrm{II,X3D}}/K_{\mathrm{II,Reference}}$

6.3 Stress intensity factor prediction for micro-cracks with coarse mesh

In this Section, the accuracy of the XFEM technique in predicting stress intensity factors for micro-cracks using a coarse mesh is assessed. The examples of three-point bending and uniaxial tensile tests on single edge cracked specimen are analysed. The two examples are calculated with a regular mesh of 4-node quadrilateral elements with an edge size set to 0.25 mm. Young's modulus is chosen as 70,000 MPa and Poisson's ratio is taken as 0.25.

6.3.1 Three-point bending specimen

In this example, the minimum crack length, that provides an accurate solution in terms of K_{I}, is identified in relation to the mesh size l and enrichment radius r. For this purpose, a single edge notch three-point bending specimen is considered, whose sketch is shown in Fig. 6.5.

In the numerical model, plane strain conditions are considered. The applied load is $P = 25$N. The crack a is located at the mid-span of the beam, and its length varies from 0.01 mm to 0.15 mm. In particular, five crack lengths are taken into account: $a = 0.01$, 0.02, 0.05, 0.125 and 0.15 mm. The crack mouths are placed in the middle

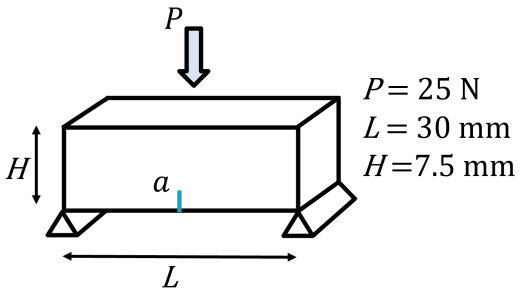

Fig. 6.5 Sketch of the three-point bending test

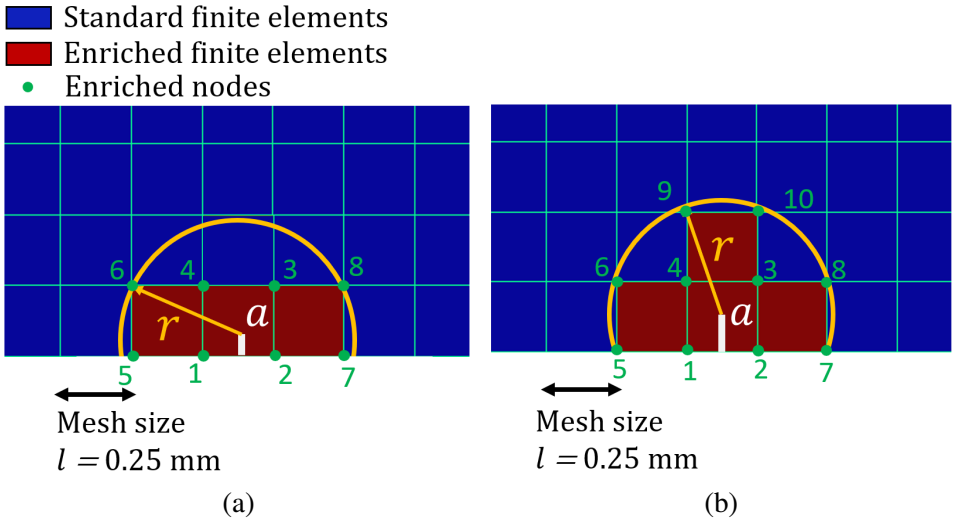

Fig. 6.6 FE mesh and enriched finite elements: (a) $a = 0.01 \div 0.05$ mm and $r = 0.45$ mm; (b) $a = 0.125 \div 0.15$ mm and $r = 0.45$ mm or $a = 0.01 \div 0.15$ mm and $r = 0.51$ mm

of the finite element side (see Fig. 6.6). Since the mesh size is $l = 0.25$ mm, the crack length ranges between 4% and 60% of the mesh size.

To investigate the effect of the number of enriched nodes on the solution, two different enrichment radius r are chosen: $r = 0.45$ mm and $r = 0.51$ mm. As a consequence, three finite elements are enriched for $r = 0.45$ mm and $a = 0.01 \div 0.05$ mm, as illustrated in Fig. 6.6a. Whereas in the case of $r = 0.45$ and $a = 0.125 \div 0.15$ mm or $r = 0.51$ and $a = 0.01 \div 0.15$ mm, four finite elements are enriched (see Fig. 6.6b). Because of the very small extension of the enriched region, the constraint to obtain a constant value for K_{I} (and K_{II}) is applied to all the enriched nodes. The 20×20 Gaussian quadrature rule is adopted for the numerical integration over the enriched finite elements.

The resulting values of K_{I} are listed in Tabs. 6.4 and 6.5 respectively for $r = 0.45$ mm and for $r = 0.51$ mm, together with the known solutions reported in the handbook by Tada *et al.* [115]. In the tables, the error is computed as:

$$Error = \frac{K_{\mathrm{I,X3D}} - K_{\mathrm{I,Handbook}}}{K_{\mathrm{I,Handbook}}} \tag{6.2}$$

Table 6.4 K_{I} values for a single edge notched three-point bending specimen with $r = 0.45$ mm

a (mm)	a/l (-)	nr. enrich. el. (-)	$K_{\mathrm{I,X3D}}$ (MPa mm$^{1/2}$)	$K_{\mathrm{I,Handbook}}$ [115] (MPa mm$^{1/2}$)	$Error$ (%)
0.15	0.6	4	14.24	14.97	-4.85
0.125	0.5	4	13.27	13.73	-3.32
0.05	0.2	3	8.40	8.81	-4.63
0.02	0.08	3	5.34	5.61	-4.73
0.01	0.04	3	4.40	3.97	+10.80

Table 6.5 K_{I} values for a single edge notched three-point bending specimen with $r = 0.51$ mm

a (mm)	a/l (-)	nr. enrich. el. (-)	$K_{\mathrm{I,X3D}}$ (MPa mm$^{1/2}$)	$K_{\mathrm{I,Handbook}}$ [115] (MPa mm$^{1/2}$)	$Error$ (%)
0.15	0.6	4	14.24	14.97	-4.85
0.125	0.5	4	13.27	13.73	-3.32
0.05	0.2	4	8.57	8.81	-2.71
0.02	0.08	4	5.67	5.61	+1.16
0.01	0.04	4	4.78	3.97	+20.35

Tables 6.4 and 6.5 show that in the range $0.08 \leq a/l \leq 0.6$ the error in the estimation of K_{I} is below 5%, whereas for $a/l = 0.04$ the error is about 11% with $r = 0.45$ mm and 20% with $r = 0.51$ mm. In this regard, for $a = 0.01$ mm a worst solution is obtained with $r = 0.51$ mm, likely because the nodes 9 and 10, represented in Fig. 6.6b, don not fall in a region where the solution is dominate by the asymptotic field.

6.3.2 Single edge notched tension specimen

Adopting the mesh size of the previous case, this example aims to evaluate the stress intensity factors and compare them to reference solutions for a number of crack lengths ranging from 20 µm to 100 µm, which are typical sizes for flaws in glass [105]. A single edge notched specimen under tension is analysed, whose geometry, load and boundary conditions are shown in Fig. 6.7. Plane strain conditions are adopted. The specimen has height $H = 30$ mm and width $W = 7.5$. It is subjected to a tensile stress $\sigma = 10$ MPa at the bottom and the top edges.

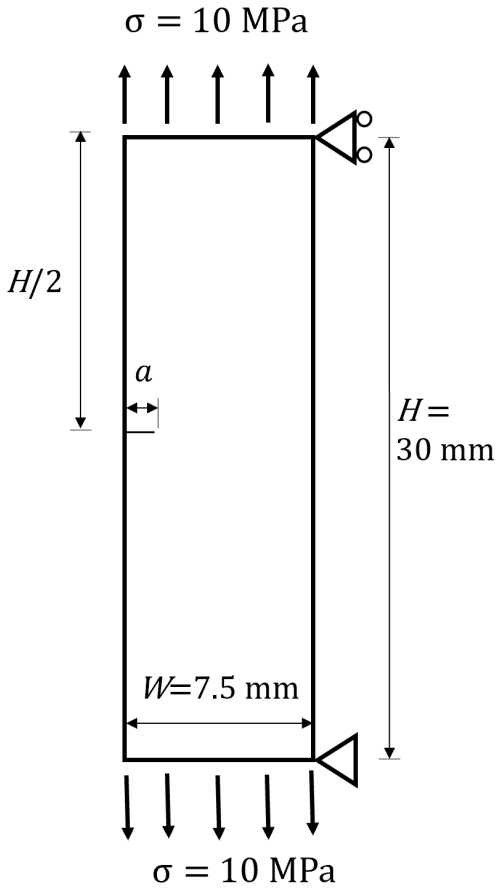

Fig. 6.7 Sketch of the uniaxial tensile test

As previously stated, the specimen includes a crack whose size a ranges from 0.02 mm to 0.1 mm as indicated in Tab. 6.6. The enrichment radius is chosen as $r = 0.45$ mm. Because the mesh size is $l = 0.25$ mm and the crack mouth is located in the middle of the finite element side, only three finite elements are enriched for

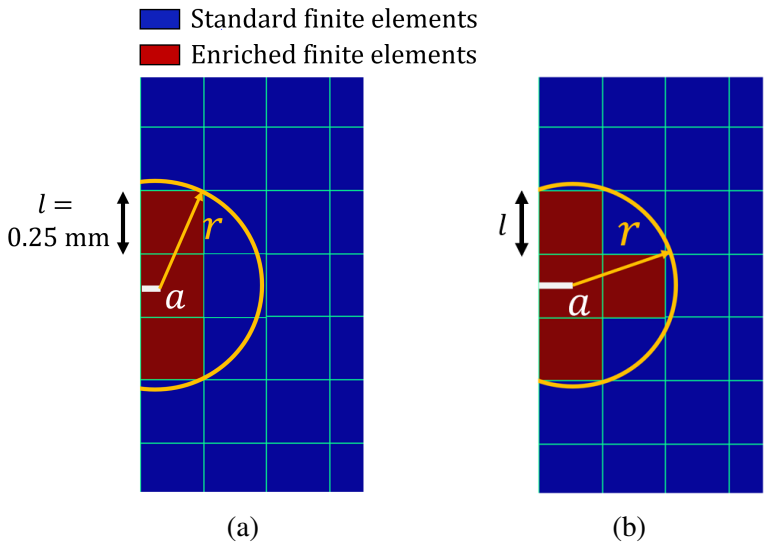

Fig. 6.8 FE mesh and enriched finite elements: (a) $a = 0.02 \div 0.065$ mm, $r = 0.45$ mm; (b) $a = 0.07 \div 0.1$ mm, $r = 0.45$ mm

$a = 0.02 \div 0.065$ mm, as illustrated in Fig. 6.8a. Whereas, for $a = 0.07 \div 0.1$ mm, four finite elements are enriched (see Fig. 6.8b). As in the previous case, given the very small extension of the enriched region, the constraint to obtain a constant value for K_{I} (and K_{II}) is applied to all the enriched nodes. Both 8×8 and 20×20 Gaussian quadrature rules are used for the numerical integration over the enriched finite elements.

The K_{I} values obtained with the numerical simulations are listed in Tab. 6.6, together with the reference solutions calculated as:

$$K_{\mathrm{I}} = \sigma \sqrt{\pi a} F(a/W) \tag{6.3}$$

where $F(a/W)$ is calculated for each single crack length a with accuracy better than 0.5% as according to the handbook by Tada *et al.* [115].

Table 6.6 shows on average that the 20×20 Gauss quadrature yields better results than the 8×8 Gauss quadrature, confirming the findings of Section 6.2. In particular, in the case of 20×20 GP, the error in the estimation of K_{I} is below 5% for any crack length between 0.02 mm and 0.1 mm. For this reason, in the next following examples the 20×20 Gauss quadrature will be adopted.

Table 6.6 K_{I} values for a single edge notched tension specimen

	8×8 Gauss Points		20×20 Gauss Points		Reference Solution
a (mm)	$K_{\mathrm{I,X3D}}$ ($\mathrm{MPa\,mm^{1/2}}$)	$Error$ (%)	$K_{\mathrm{I,X3D}}$ ($\mathrm{MPa\,mm^{1/2}}$)	$Error$ (%)	K_{I} (Eq. (6.3)) ($\mathrm{MPa\,mm^{1/2}}$)
0.02	2.93	+4.2	2.78	-1.1	2.81
0.025	3.25	+3.4	3.10	-1.4	3.14
0.03	3.62	+5.2	3.31	-3.8	3.44
0.035	3.96	+6.5	3.64	-2.1	3.72
0.04	4.19	+5.4	3.88	-2.4	3.97
0.05	4.44	-0.1	4.40	-1.0	4.44
0.06	4.87	+0.1	4.70	-3.4	4.87
0.065	5.22	+3.1	5.03	-0.7	5.07
0.07	5.62	+6.9	5.32	+1.2	5.26
0.075	5.86	+7.7	5.36	-1.5	5.44
0.08	6.0	+6.8	5.57	-0.9	5.62
0.09	6.04	+1.4	5.95	-0.2	5.96
0.1	6.20	-1.3	6.26	-0.3	6.28

6.4 Cracks located near stress concentration region

In the case of arbitrary geometries, load, and boundary conditions, when the solution is not provided by the literature, the extended finite element method is very successful in the evaluation of the stress intensity factor. As for example when cracks are within stress concentration regions or interact with each other. The former case is investigated in the present section.

Although Liu *et al.* [121] have already shown that the XFEM results are nearly independent of the mesh density, in this example, we aim to prove that the mesh size has almost no effect on the K_{I} solution, even when cracks are near stress concentrations. On the other hand, it is well known that the reliability of the allowable stress design approach depends on the accuracy of the FEM model, that is highly dependent on the number of finite elements used to represent the physical domain. Local effects like stress concentrations are not captured by a coarse mesh. Furthermore, mesh refinement does not always result in convergence of the finite element solution, as for example in the case of stress singularities.

In this example, the stress intensity factor is evaluated, by means of the *X3D* code, in the case of an isotropic plate with a circular hole emanating a radial crack

remotely subjected to uniaxial loading. The setup of the test implemented in the finite element code is illustrated in Fig. 6.9. The mechanical properties of the virtual specimen are: Young's modulus $E = 70,000\,\text{MPa}$ and Poisson ratio $\nu = 0.25$.

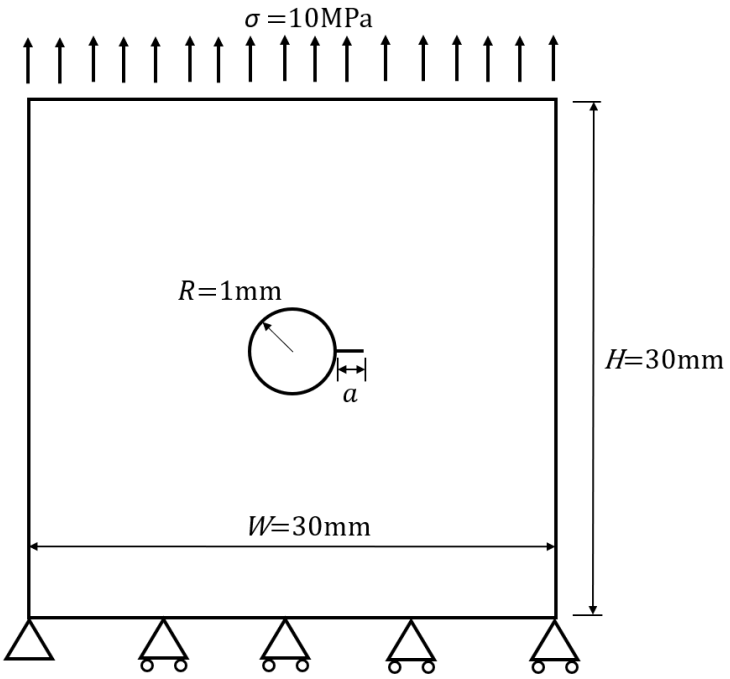

Fig. 6.9 Isotropic plate with a circular hole emanating a radial crack remotely subjected to uniaxial loading

A plane strain FE model is considered with 4-node quadrilateral finite elements for the discretization of the continuum. Three different mesh sizes l are chosen in order to evaluate the effect of the mesh density on the results, as shown in Fig. 6.10. The ratio between the crack length a and the mesh size l is kept constant at 0.5. As in the previous example, only the four finite elements closest to the crack tip are enriched (see Fig. 6.10).

In Tab 6.7, the stress intensity factors $K_{\text{I,X3D}}$ obtained using the *X3D* code are compared to the values estimated according to the handbook by Tada *et al.* [115] in the case of infinite plate. In Table 6.7, the *Error* is calculated as in the previous example (see Eq. (6.2)).

It can be observed that as the mesh size is reduced, the error decreases, however it remains below 10% even if a coarser mesh is used. It is worth noting that the

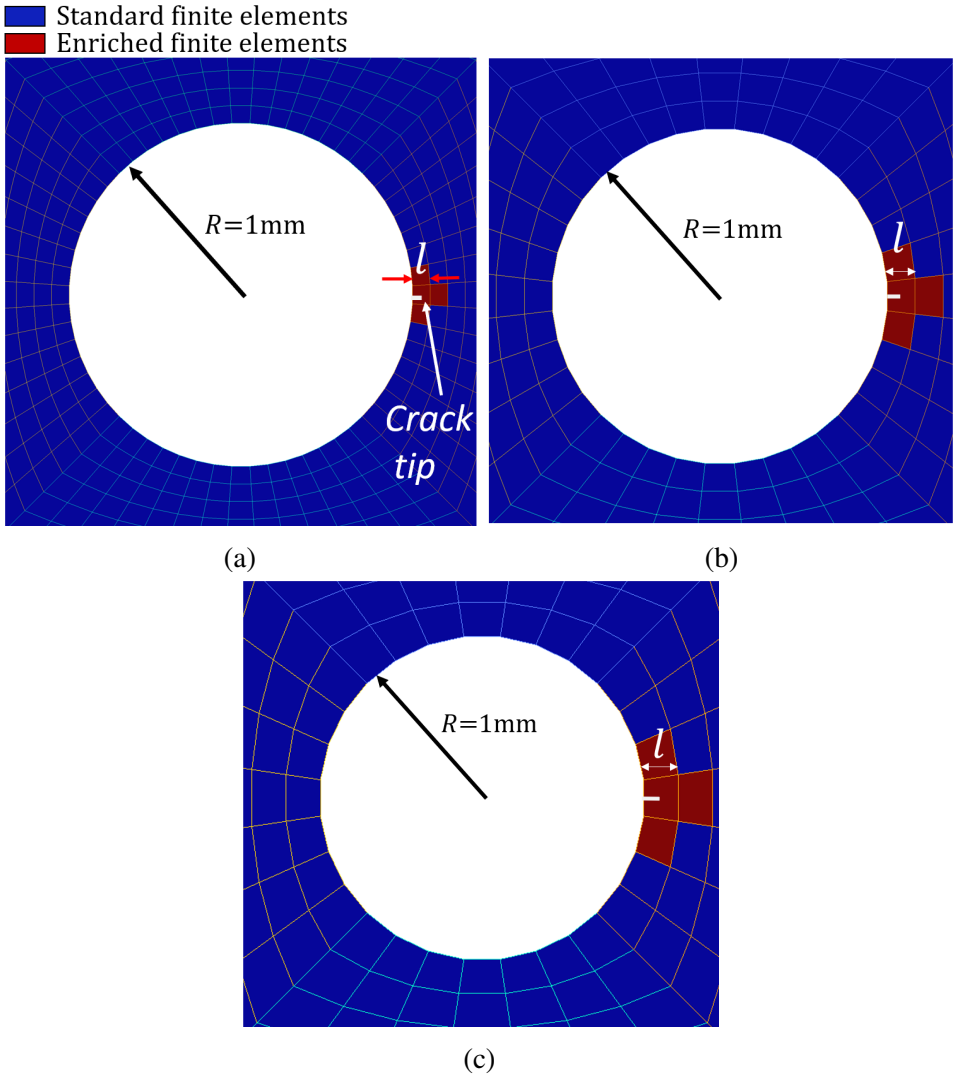

Fig. 6.10 FE mesh and enriched finite elements of a plate with a hole emanating a crack: (a) $a = 0.05$mm, $l \simeq 0.1$mm; (b) $a = 0.075$mm, $l \simeq 0.15$mm; (c) $a = 0.1$mm, $l \simeq 0.2$mm

Table 6.7 Mode I stress intensity factors for a crack emanating from a hole.

a (mm)	mesh size l (mm)	a/l	σ (MPa)	$K_{\mathrm{I,X3D}}$ ($\mathrm{MPa\,mm^{1/2}}$)	$K_{\mathrm{I,Reference}}$ [115] ($\mathrm{MPa\,mm^{1/2}}$)	$Error$ (%)
0.05	0.1	0.5	10	12.50	11.90	+5
0.075	0.15	0.5	10	14.60	13.83	+5.5
0.1	0.2	0.5	10	16.5	15.25	+8.2

reference solution is valid for an infinite plate, therefore an increase in the stress intensity factor in the case of a plate with finite dimensions is reasonable.

The results of these tests show also the suitability of the method for investigating the edge strength of architectural glass with cylindrically formed holes. By including in the FE mesh the actual flaws distribution, the real failure load can be obtained using the stress intensity factor-based failure criterion. The experimental and numerical studies conducted by Sanders *et al.* [130] showed that the stress-based design approach, adopted by the standard NEN 2608:2014 [131], overestimates the failure load of bolted connections, therefore the proposed method could replace or support experiments for a safer design.

6.5 Interaction among cracks

In this Section the example of three interactive parallel edge cracks in a plate subjected to tensile load is analysed.

Auradou *et al.* [132] showed that the presence of neighboring cracks modifies the stress field within the material and induces a shielding of the stress at the crack tips, increasing the lifetime of the material. Due to shielding, the longest crack could not lead to the failure of the sample. In addition, the shielding effect becomes more pronounced when the crack lengths are of the order of the distance separating them. According to Afferrante *et al.* [34], the Weibull parameters θ and β of Eq. (5.18a) would change depending on the distribution of cracks, their distances, and their interaction with the geometry and stress field. The correct Weibull parameters can only be obtained through numerical simulations in which the crack distribution is directly included in the geometry.

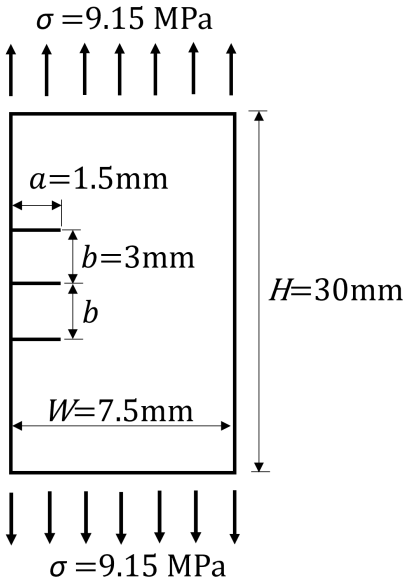

Fig. 6.11 Parallel cracks in a finite plate under uniaxial tensile load

Figure 6.11 shows the setup of the virtual specimen for this example. A tensile stress $\sigma = 9.15$ MPa is applied to a finite plate with three edge cracks, the plate width is $W = 7.5$ mm, while its height is $H = 30$ mm. The length of the three cracks is $a = 1.5$ mm, and they are distant from each other $b = 3$ mm, i.e. twice their length. As in the preceding cases, the mechanical properties are those of glass, i.e., Young's modulus $E = 70,000$ MPa and Poisson ratio $\nu = 0.25$. A regular mesh of 4-node quadrilateral elements is employed with mesh size $l = 0.25$ mm; plane strain conditions are assumed. The radius $r = 0.50$ mm determines which nodes and, therefore, which finite elements, are enriched (see Fig. 6.12), while the radius $r_0 = 0.50$ mm pivoted in the crack tip, establishes for which nodes the K_{I} and K_{II} values are forced to be constant.

The K_{I} results for the central and outer cracks are listed in Tab. 6.8. The results are compared to the numerical solution obtained by Jiang *et al.* [133].

Table 6.8 Stress intensity factors for parallel cracks in a finite plate

crack	a (mm)	σ (MPa)	$K_{\mathrm{I,X3D}}$ ($\mathrm{MPa\,m^{1/2}}$)	$K_{\mathrm{I,Reference}}$ [133] ($\mathrm{MPa\,m^{1/2}}$)	$Error$ (%)
outer	1.5	9.15	0.75	0.76	-1.60
central	1.5	9.15	0.63	0.65	-3.37

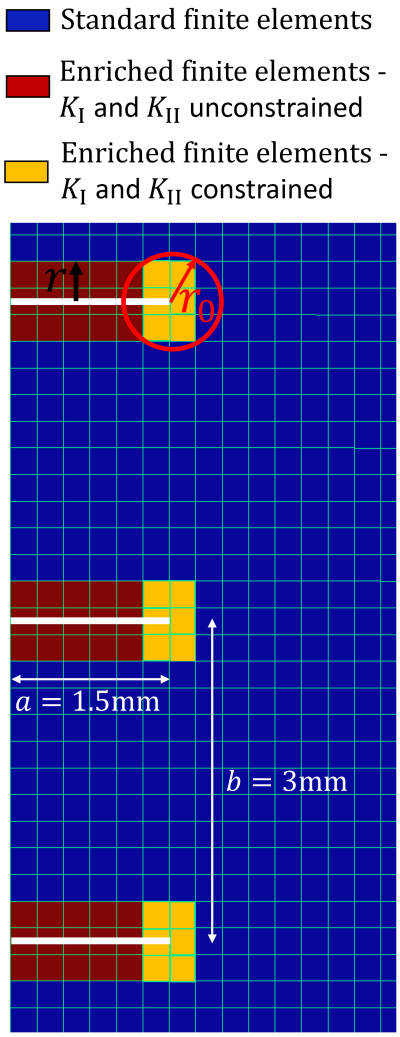

Fig. 6.12 Enriched finite elements around three cracks in a finite plate under tensile load

As indicated in Tab. 6.8, the error in terms of K_I is less than 5%. Furthermore, the stress intensity factor at the tip of the outer cracks coincides with the fracture toughness for glass $K_{IC} = 0.75$ MPa m$^{1/2}$, therefore the chosen tensile stress $\sigma =$ 9.15 MPa corresponds to the failure stress. If the three cracks were isolated there would be no difference between the three stress intensity factors, moreover their values would be $K_I = 0.86$ MPa m$^{1/2}$ for $\sigma = 9.15$ MPa. As a consequence, the failure load for isolated cracks would be $\sigma = 8$ MPa, which is 12.6% lower than that of interactive cracks.

6.6 Conclusions

In this chapter, several examples were solved in order to assess the accuracy of the XFEM method for different scenarios. In particular, it has been proven that the XFEM technique returns an accurate K_{I} value even when the mesh is coarse, unlike the FEM approach which requires a denser mesh to yield a precise stress value in correspondence with stress concentrations and singularities. The accuracy of the method is also provided in the case of interaction among cracks, that produces a shielding effect increasing the resistance of brittle materials. However, strategies should be developed and implemented in the XFEM code to mitigate the effect of the numerical integration of the stiffness matrix on the solutions K_{I} and K_{II} when the crack is inclined. Based on the findings of the tests conducted, the optimal parameters involved in XFEM analysis are given below for accurate results in the case of micro-cracks. For a regular mesh of 4-node quadrilateral elements, the maximum mesh size should be $l_{\max} = 12.5a_0$, being a_0 the minimum crack size adopted. The optimal enrichment radius r should be in the range $(22.5a_0,\ 25.5a_0)$. As a result, at least the three or four finite elements nearest to the crack should be enriched in the case of crack sizes a in the range $(0.08l,\ 0.6l)$. The 20×20 Gauss quadrature rule over the enriched finite elements provided the best solution. In Chapter 7, the above parameters will be adopted to assess the structural integrity of glass components.

Chapter 7

Case studies

7.1 Introduction

In the present Chapter several case studies are solved with the proposed probabilistic FEM approach to demonstrate its accuracy and reliability in assessing the structural integrity of glass components.

All examples reported below are calculated with a regular mesh of 4-node quadrilateral elements. Plane stress conditions are assumed. Poisson's ratio is taken as 0.25, Young's modulus is chosen as 70,000 MPa, and the glass fracture toughness has been set to 0.75 $\mathrm{MPa\,m^{1/2}}$. A 20×20 Gauss quadrature rule is adopted over the enriched finite elements, while a standard 2×2 Gauss quadrature is used over elements which do not contain any enriched node.

The influence of the stress gradient on the load-carrying capacity of glass components is investigated using four different test configurations: a specimen under uniaxial tensile load, a beam under three point bending, a simply supported beam under uniformly distributed load, and a cantilever beam subjected to uniformly distributed load. In addition, a comparative study is carried out to show the differences between the stress-based design approach and the proposed probabilistic one.

7.2 Edge-cracked specimen under uniaxial tensile load

7.2.1 Specimen with 5 edge cracks

Consider an edge-cracked specimen, as shown in Fig. 7.1a, subjected to uniaxial tensile stress, provided by a uniform distributed load, q, applied at the bottom and top edges. The specimen has height $H = 30$ mm, width $W = 7.5$ mm and thickness $th = 1$ mm. At first, the specimen includes only five cracks, which are 5.8 mm apart. The crack size a follows the Pareto distribution:

$$F(a) = 1 - \left(\frac{a_0}{a}\right)^c \tag{7.1}$$

which is defined by the scale parameter $a_0 = 0.020$ mm, that represents the smallest crack size, and the shape parameter $c = 3.0$. The value of the parameter c is chosen based on the findings of the study by Vandebroek *et al.* [112], where the glass edge strength was investigated using a four-point bending configuration. The tests, that involved almost 40 specimens with polished edge finishing, showed that the experimental data could be interpolated by a Weibull distribution with shape parameter $\beta \simeq 6$. As a consequence, the Pareto parameter c can be estimated using Eq. (5.18b) as $c = \beta/2$.

The continuum is discretized using a uniform mesh of 4-node quadrilateral elements (see Fig. 7.1b). The edge size of the finite element is $l = 0.25$ mm, while the enriched finite elements are those located in the circumference centered at the tip of each crack and with a radius $r = 0.45$ mm (see Fig. 7.2), as explained previously in Section 6.3.2.

The failure load $q_{\mathrm{f,i}}$ of the virtual specimen in Fig. 7.1a is calculated for $N = 5,000$ different simulations. In each simulation the size of the cracks varies according to the Pareto distribution. The failure load is obtained for each simulation by equating the maximum value of K_{I} to K_{IC}. Because the crack size follows the Pareto distribution, the statistical population of the failure load, q_{f}, of the glass specimen, can be represented by a two parameter Weibull distribution function:

$$F(q_{\mathrm{f}}) = 1 - \exp\left[-\left(\frac{q_{\mathrm{f}}}{\hat{\theta}}\right)^{\hat{\beta}}\right] \tag{7.2}$$

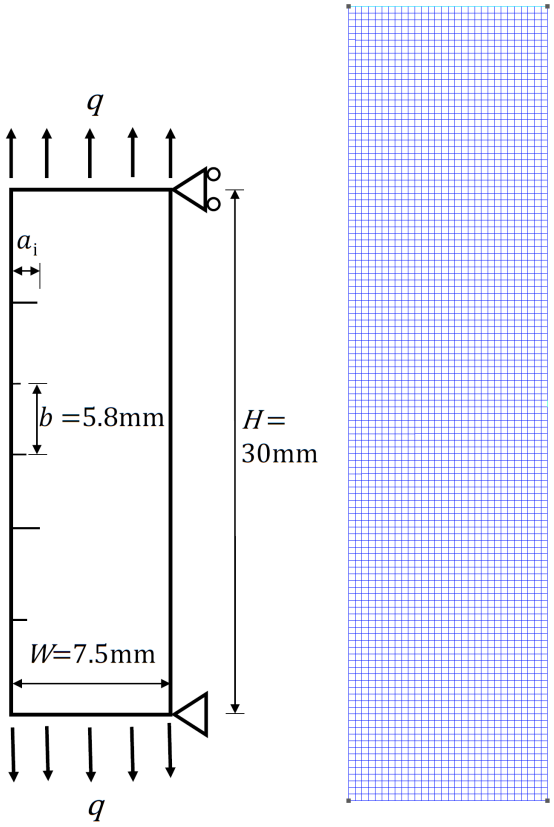

Fig. 7.1 Specimen under uniaxial tensile load: (a) geometry and loads; (b) FE discretization

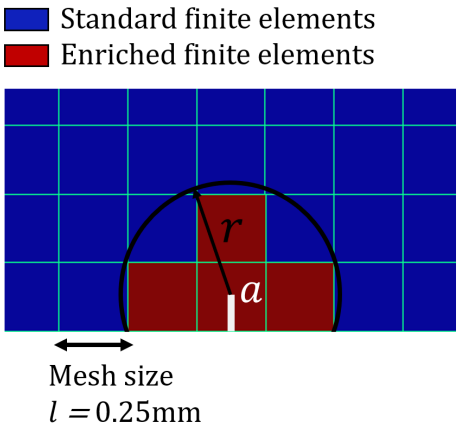

Fig. 7.2 Criterion for the enrichment of nodes and finite elements

where $\hat{\beta}$ and $\hat{\theta}$ are the Weibull shape and scale parameters, which can be estimated with the moments method [134]:

$$\frac{\Gamma\left(1+\frac{2}{\hat{\beta}}\right)}{\Gamma^2\left(1+\frac{1}{\hat{\beta}}\right)}-1=\frac{\hat{s}^2_{q_\mathrm{f}}}{\hat{\mu}^2_{q_\mathrm{f}}} \tag{7.3a}$$

$$\hat{\theta} = \frac{\hat{\mu}_{q_\mathrm{f}}}{\Gamma\left(1+\frac{1}{\hat{\beta}}\right)} \tag{7.3b}$$

being $\hat{\mu}_{q_\mathrm{f}}$ and $\hat{s}^2_{q_\mathrm{f}}$ the sample mean and variance:

$$\hat{\mu}_{q_\mathrm{f}} = \frac{\sum_{i=1}^{N} q_{\mathrm{f,i}}}{N} \tag{7.4a}$$

$$\hat{s}^2_{q_\mathrm{f}} = \frac{\sum_{i=1}^{N} \left(q_{\mathrm{f,i}} - \hat{\mu}_{q_\mathrm{f}}\right)^2}{N-1} \tag{7.4b}$$

Solving Eq. (7.3a), using any of a number of standard iterative root-findings procedures, and Eq. (7.3b), the parameters of the Weibull distribution function of the failure load can be obtained: $\hat{\theta} = 64.90$ N/mm and $\hat{\beta} = 6.13$.

The computed failure loads, $q_{\mathrm{f,i}}$, are ranked in ascending order (i = 1 to N) to build an ordered sample and, then, a probability of failure is assigned to each value $q_{\mathrm{f,i}}$ of the ordered sample by means of probability estimators $\hat{G}_i$:

$$\hat{G}_i = \frac{i-0.3}{n+0.4} \tag{7.5}$$

Finally, the points ($q_{\mathrm{f,i}}$, $\hat{G}_i$) build the sampling cumulative distribution function of the failure load which is plotted into the Weibull diagram of Figs. 7.3a and 7.3b. The Weibull density function is plotted in Fig. 7.3c, where it is compared to the histogram whose bars represent the relative number of observations of the failure load, q_f. In Fig. 7.3c, the histogram has been normalized to reflect the probability density function. A reasonable fit of the numerical results is obtained with the Weibull distribution. However, it is crucial to note that this distribution is the outcome of the analysis and was not assumed a-priori. As a result the histogram is not a smooth function. It is worth noticing that while the numerical results plotted in Fig. 7.3b follow a regular two parameter Weibull distribution function, the experimental results in Fig. 5.1 could be more accurately interpolated by a bilinear and bimodal Weibull distributions in accordance with the findings of Ballarini *et al.* [78]. While for the numerical test the initial cracks were extracted from a single statistical population, the experimental results in Fig. 5.1 reveal that the initial cracks were from different statistical populations, which differ from each other in the crack shape or in the

dispersion of the crack size, or in the two factors combined. In particular, the experimental results indicate that the smallest cracks are more scattered than the biggest ones, which causes the slope of the right tail of the sampling distribution of the failure stress to be lower than the left one.

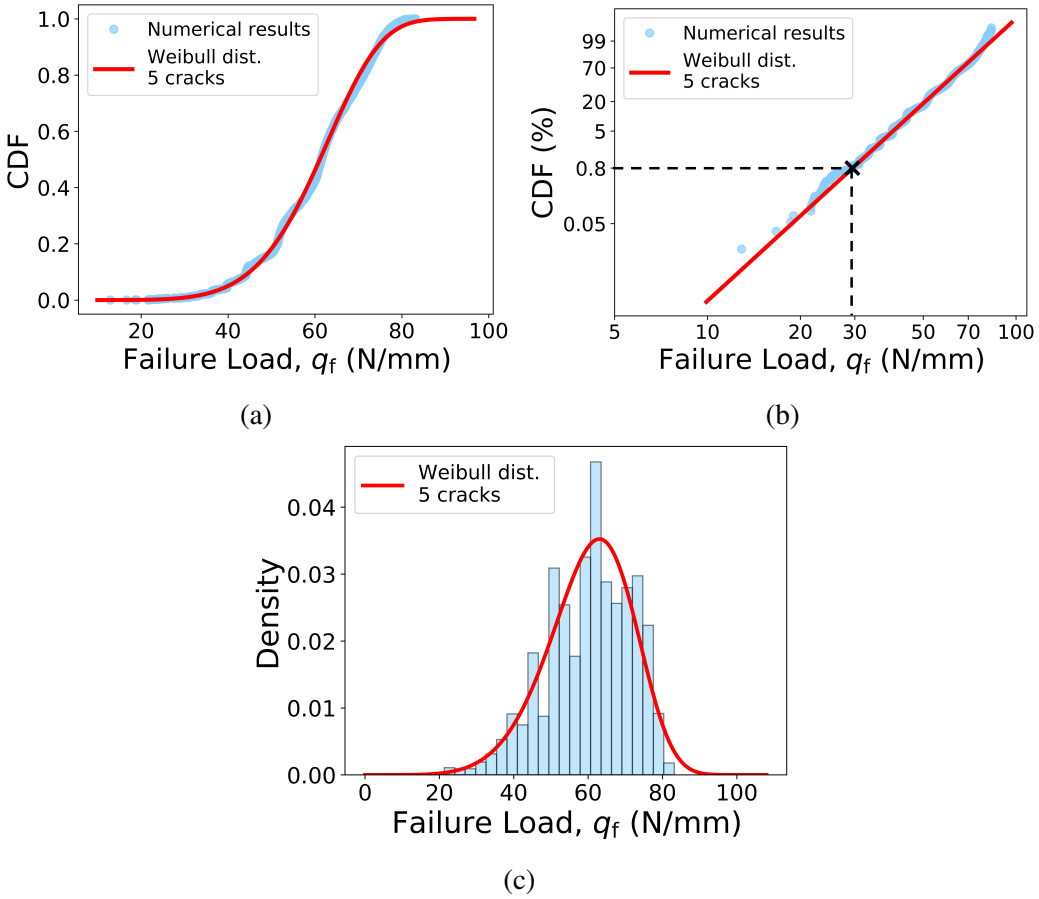

Fig. 7.3 Weibull distribution of the failure load for the glass specimen with 5 cracks under uniaxial tensile load: (a) Cumulative distribution function (CDF); (b) Linearised cumulative distribution function; (c) Probability density function

The statistical distribution of the critical edge crack, which represents the point of origin of failure, has been obtained by the numerical results. As evidently shown in Fig. 7.4a and in Fig. 7.4b, the Fréchet distribution provided by Eq. (5.17) fits the numerical data perfectly. The Fréchet distribution parameters λ and α are calculated by means of the method of moments estimation [135]. The estimator for $\hat{\alpha}$ can be

obtained by solving the following non-linear equation:

$$\frac{\Gamma\left(1-2\hat{\alpha}^{-1}\right)}{\Gamma^2\left(1-\hat{\alpha}^{-1}\right)}-1=\frac{\hat{s}_{a_c}^2}{\hat{\mu}_{a_c}^2} \tag{7.6}$$

The parameter $\hat{\lambda}$ can be obtained by solving:

$$\hat{\lambda}=\frac{\hat{\mu}_{a_c}^{\hat{\alpha}}}{\Gamma^{\hat{\alpha}}\left(1-\hat{\alpha}^{-1}\right)} \tag{7.7}$$

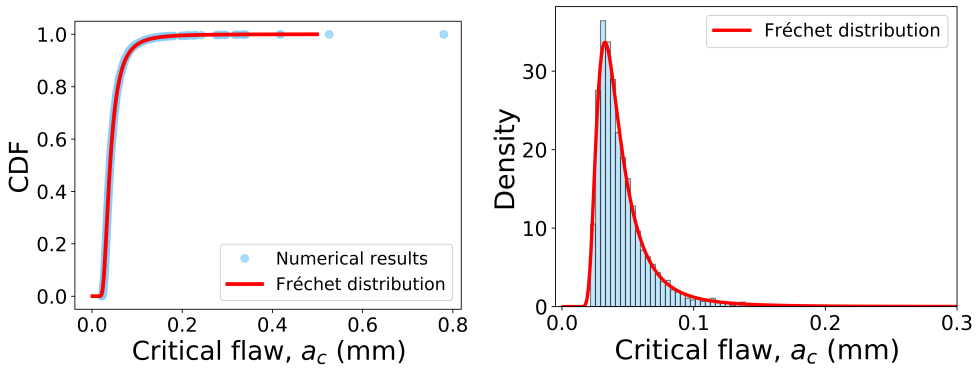

(a) (b)

Fig. 7.4 Fréchet distribution of the critical edge crack size for the glass specimen with 5 cracks under uniaxial tensile load: (a) Cumulative distribution function (CDF); (b) Probability density function

In addition, the statistical position of the point of origin of failure is plotted in Fig. 7.5. As the virtual specimen is subjected to a uniaxial tensile load, each of the five crack locations has the same probability of being the point of origin of the failure.

In conclusion, the Weibull and Fréchet distributions derived from the numerical results are compared to the theoretical ones. In particular, in Tab. 7.1, the estimated Weibull parameters $\hat{\theta}$ and $\hat{\beta}$ are compared to the theoretical ones θ and β calculated according to Eq. (5.18b) adopting $Y=1.12$ and $K_{\mathrm{IC}}=0.75\ \mathrm{MPa\,m}^{1/2}$, whereas the estimated Fréchet parameters $\hat{\alpha}$ and $\hat{\lambda}$ are compared to the theoretical ones α and λ obtained from Eqs. (5.16a) and (5.16b). The data in Tab. 7.1 show a good match between the estimated and theoretical distribution parameters, which is another proof of the accuracy and validity of the proposed methodology.

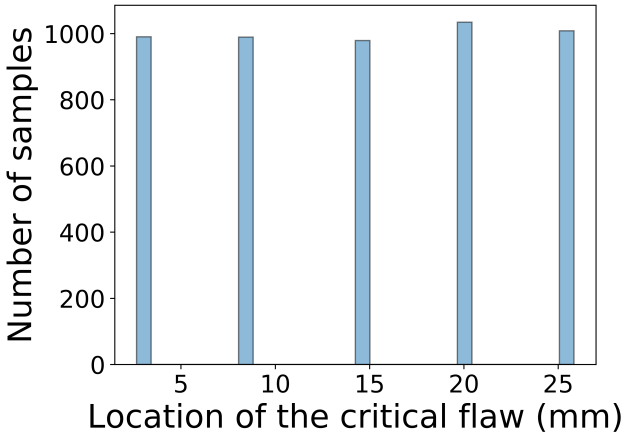

Fig. 7.5 Location of the critical edge crack for the glass specimen under uniaxial tensile load. Case with 5 cracks

Table 7.1 Weibull and Fréchet parameters for the glass specimen under uniaxial tensile load. Case with 5 cracks

n. of cracks	Pareto param.		Weibull parameters				Fréchet parameters			
m	a_0 (mm)	c	$\hat{\theta}$ (N/mm)	$\hat{\beta}$	θ (N/mm)	β	$\hat{\lambda}$	$\hat{\alpha}$	λ	α
5	0.02	3.0	64.9	6.1	64.6	6.0	3E-5	3.1	4E-5	3.0

7.2.2 Specimen with 29 edge cracks

In order to study the effect of the crack density on the glass strength, the number of cracks in the specimen has been increased from 5 to 29 and the Weibull distribution function of the failure load has been obtained.

The geometry and support conditions of the specimen, as well as the FE discretization, the enrichment radius r, and the statistical population of the crack size, are the same as in the previous example. The cracks, on the other hand, are placed every millimetre (see Fig. 7.6a). As in the previous case, the failure load $q_{\mathrm{f,i}}$ of the glass specimen is calculated for 5,000 different simulations in accordance to the K_{I}-based failure criterion. Fig. 7.6b shows the K_{I} values at each of the crack tips for a single simulation.

The sampling probability distributions of the failure load and critical edge crack size are plotted in Figs. 7.7 and 7.8, where they are fitted respectively with the Weibull

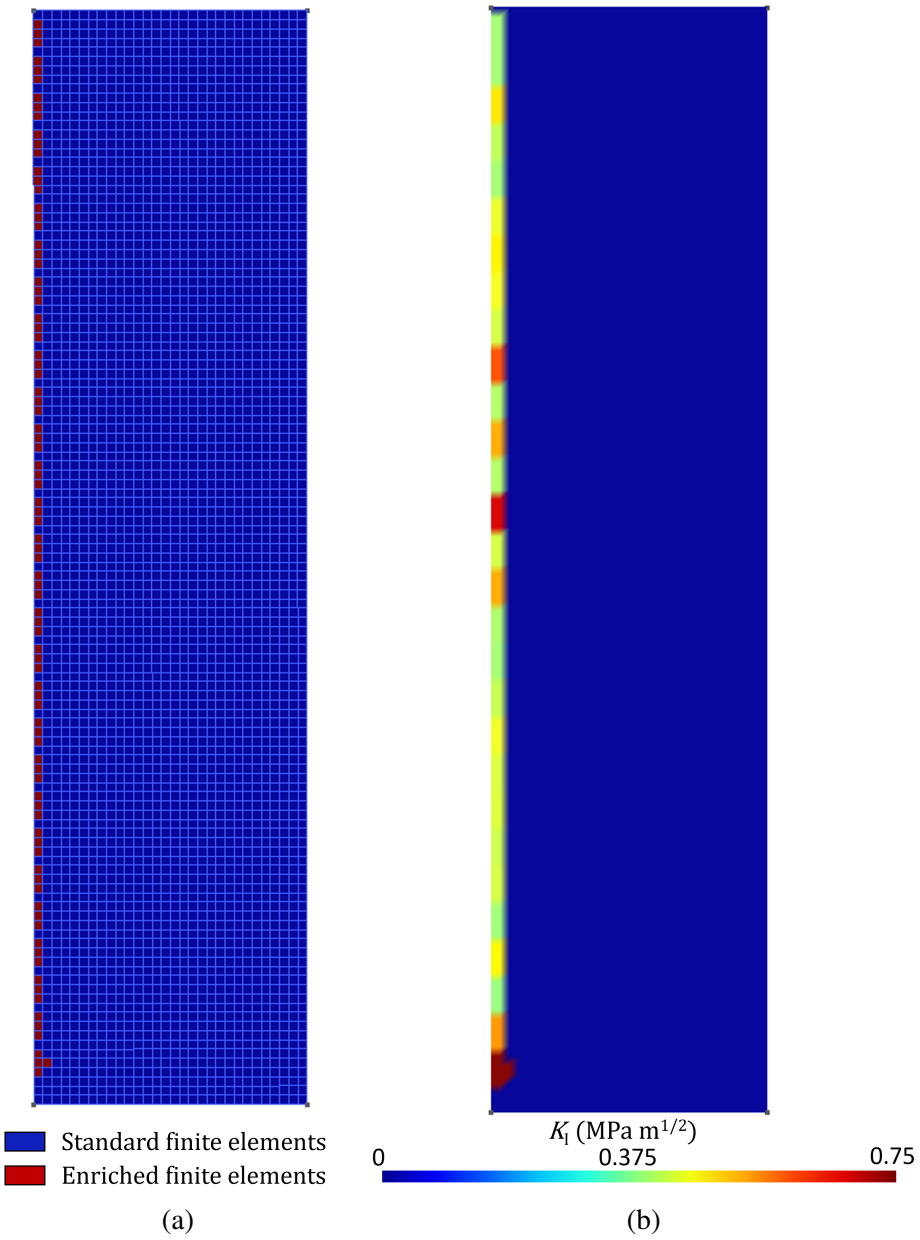

Fig. 7.6 Specimen under uniaxial tensile load: (a) FE discretization and enriched elements; (b) Results in terms of K_I for a single simulation

and Fréchet distributions. The plots show a good match between the sampling probability distribution of the failure load and the Weibull distribution, as well as an excellent fit between the sampling probability distribution of the critical edge crack and the Fréchet distribution. The estimated parameters which define the Weibull and Fréchet distributions are listed in Tab. 7.2.

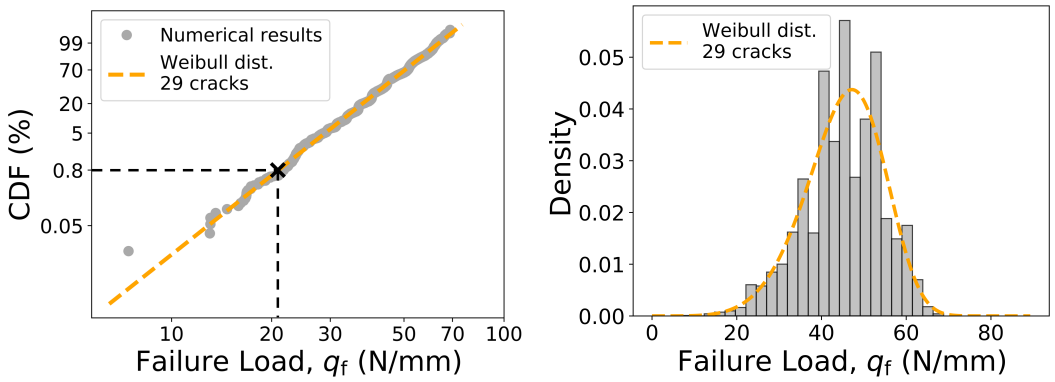

(a) (b)

Fig. 7.7 Weibull distribution of the failure load for the glass specimen with 29 cracks under uniaxial tensile load: (a) Linearised cumulative distribution function; (b) Probability density function

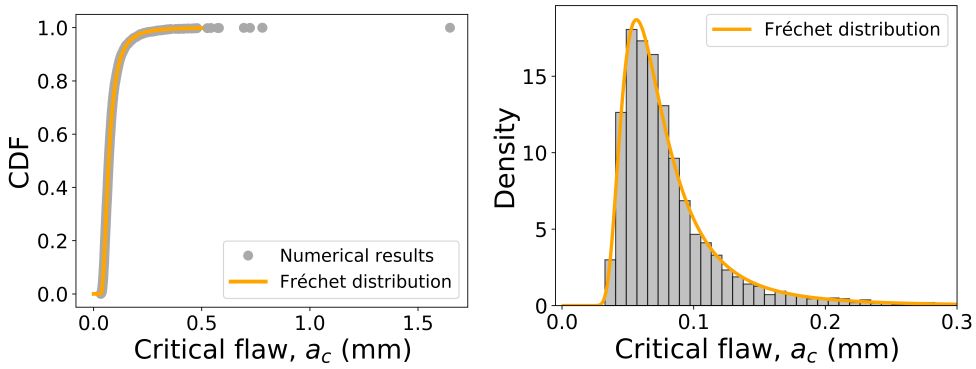

(a) (b)

Fig. 7.8 Fréchet distribution of the critical edge crack size for the glass specimen with 29 cracks under uniaxial tensile load: (a) Cumulative distribution function (CDF); (b) Probability density function

Table 7.2 Weibull and Fréchet parameters for the glass specimen under uniaxial tensile load. Case with 29 cracks

n. of cracks	Pareto param.		Weibull parameters		Fréchet parameters	
m	a_0 (mm)	c	$\hat{\theta}$ (N/mm)	$\hat{\beta}$	$\hat{\lambda}$	$\hat{\alpha}$
29	0.02	3.0	48.8	5.7	2.4E-4	3.0

Like the failure load and the critical edge crack size, the fracture origin point is considered a random variable which is predicted by the model and shown in the graph of Fig. 7.9. As in the previous case, the point of origin of failure is uniformly distributed since the specimen is subjected to a uniaxial tensile load.

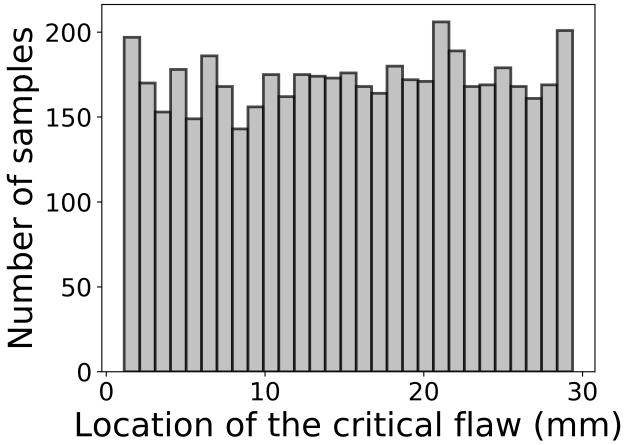

Fig. 7.9 Location of the critical edge crack for the glass specimen under uniaxial tensile load. Case with 29 cracks

Finally, the Weibull distribution functions of the failure load obtained for the specimens with 5 and 29 cracks are compared in Fig. 7.10. The two curves are almost parallel, since the parameter β of the Weibull distribution theoretically depends only on the parameter c of the Pareto distribution of the crack size a (see Eq. (5.18b)), which is the same for both cases. On the other hand, the Weibull distribution of the specimen with 29 cracks is shifted towards lower values of the failure load, which indicates a reduction in glass strength as the crack density increases. In fact, when comparing Fig 7.4a and Fig 7.8a, the specimen with 29 cracks shows larger critical edge cracks a_c than the specimen with only 5 cracks, although the crack sizes a are from the same statistical population in both cases. In accordance to the ASTM E1300-16 [5], the design load-carrying capacity of the glass specimen is chosen to be the load associated with a probability of breakage less than or equal to 0.8%. By interpolating the numerical results through the Weibull distribution functions of the specimen with 5 and 29 cracks, the following load-carrying capacity are obtained (see Figs. 7.3b and 7.7a): $q_{\mathrm{f},0.008} = 29.54$ N/mm for the specimen with 5 cracks and $q_{\mathrm{f},0.008} = 20.96$ N/mm for the specimen with 29 cracks. Therefore, we can conclude that increasing the number of cracks from 5 to 29 results in a reduction of about 29% in load-carrying capacity.

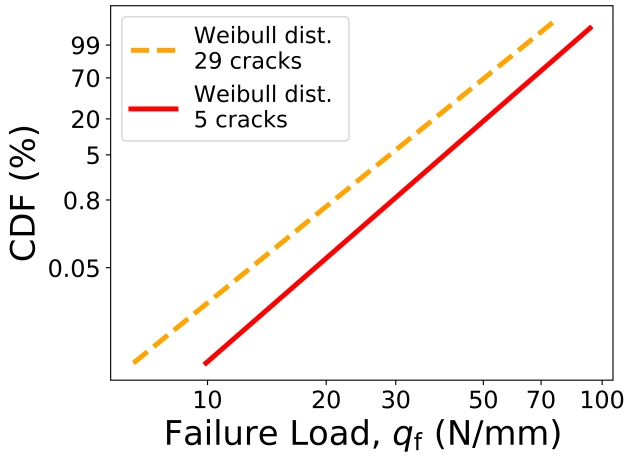

Fig. 7.10 Effect of the crack density on the Weibull distribution function of the failure load

7.3 Edge-cracked beam under three point bending

This example involves the edge cracked beam from Sect. 7.2.2 subjected to three point bending (Fig. 7.11). The beam contains 29 edge cracks, and just like the previous example, the failure load $P_{\mathrm{f,i}}$ is determined for 5,000 distinct simulations. The i-th failure load corresponds to the load for which $K_{\mathrm{I}}^{max} = K_{\mathrm{IC}}$ at one of the 29 edge cracks. For the sake of example, the K_{I} values at each crack tip for a single simulation are plotted in Fig. 7.12. The highest values of K_{I} are obtained near the mid-span of the beam, where the bending moment takes the maximum value.

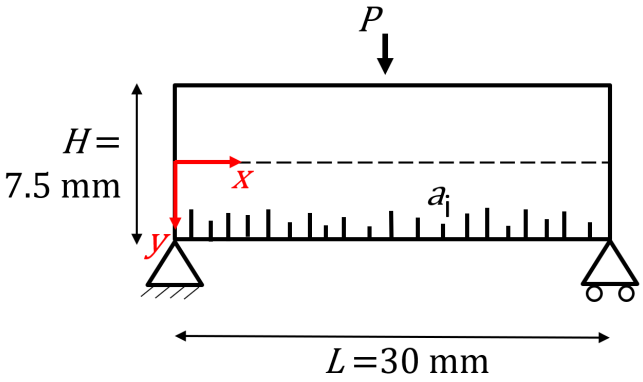

Fig. 7.11 Sketch of the three point bending test

The failure load values, $P_{\mathrm{f,i}}$, are analysed statistically using the Weibull distribution, whereas the critical crack size, a_{c}, using the Fréchet distribution, as discussed

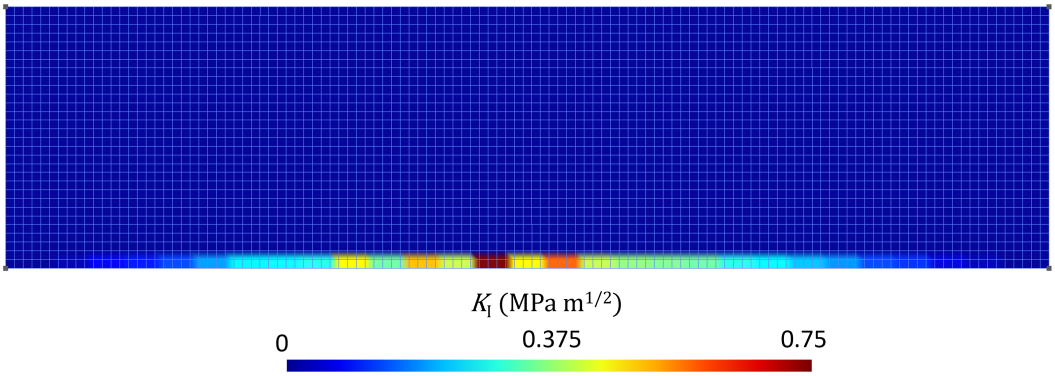

Fig. 7.12 K_I values at the crack tips for one simulation of the beam under three point bending

above. The diagrams in Fig. 7.13 show good agreement between the sampling distribution of the failure load and the Weibull distribution, as well as Fig. 7.13 shows excellent match between the sampling distribution of the critical crack size and the Fréchet distribution. The Weibull and Fréchet parameters, estimated according to the moments method, are reported in Tab. 7.3.

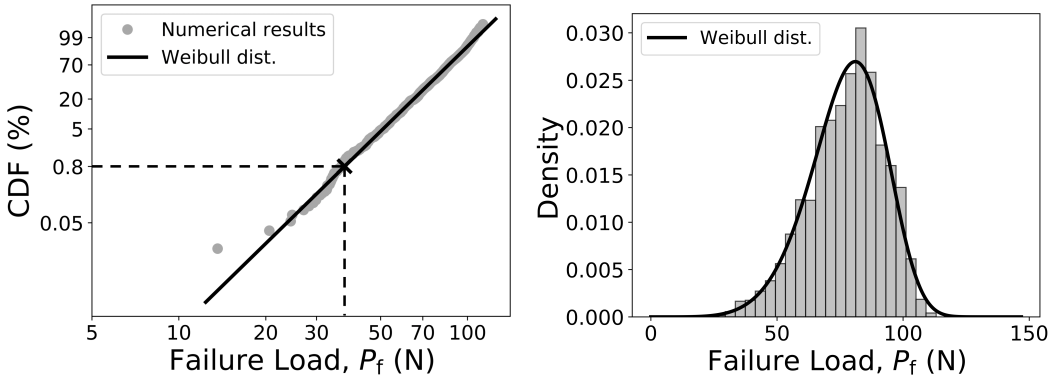

(a) (b)

Fig. 7.13 Weibull distribution of the failure load for the glass beam with 29 cracks under three point bending: (a) Linearised cumulative distribution function; (b) Probability density function

The fracture origin coordinate x is normally distributed around the mean $\bar{x} = 15$ mm (Fig. 7.15) with standard deviation $\sqrt{s_x^2} = 3.25$ mm. It is shown that fracture can occur anywhere between $x = 5$ mm and $x = 25$ mm.

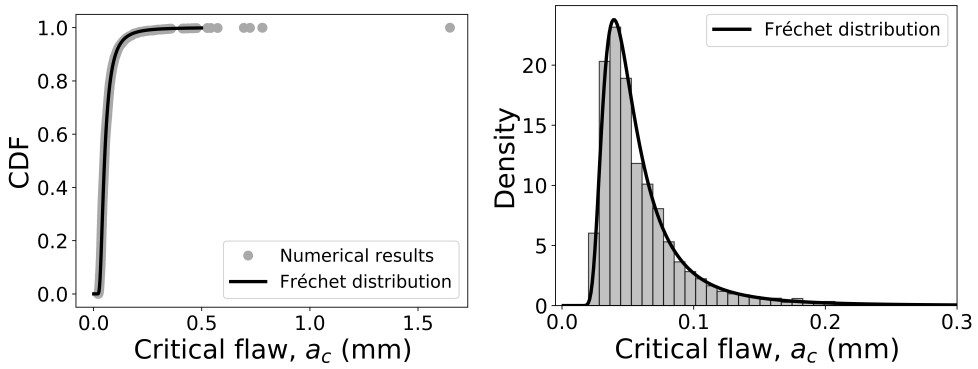

(a) (b)

Fig. 7.14 Fréchet distribution of critical edge crack for the glass beam with 29 cracks under three point bending: (a) Cumulative distribution function (CDF); (b) Probability density function

Table 7.3 Weibull and Fréchet parameters for the glass beam under three point bending. Case with 29 cracks

n. of cracks	Pareto param.		Weibull parameters		Fréchet parameters	
m	a_0 (mm)	c	$\hat{\theta}$ (N)	$\hat{\beta}$	$\hat{\lambda}$	$\hat{\alpha}$
29	0.02	3.0	83.5	6.0	2.3E-4	2.7

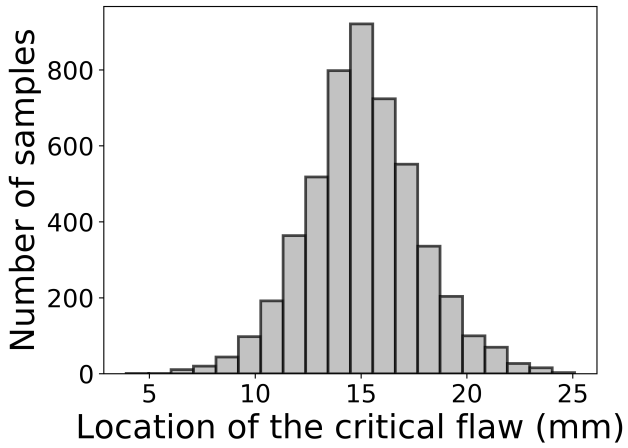

Fig. 7.15 Location of the critical edge crack for the glass beam under three point bending. Case with 29 cracks

By interpolating the sampling cumulative distribution function of the failure load, through the Weibull distribution, the following load-carrying capacity evaluated with a 0.8% breakage probability is obtained: $P_{\mathrm{f},0.008} = 37.55$ N (see Fig. 7.13a).

The design load-carrying capacity is now estimated using a stress-based failure criterion. First of all, the glass tensile strength of the beam with 29 cracks must be defined. Based on the outcomes of the previous example (see Sect. 7.2.2), the glass tensile strength evaluated with a 0.8% breakage probability is $\sigma_{\mathrm{f},0.008} = 20.96$ MPa. As a consequence, the resistant bending moment is:

$$\mathrm{M}_{\mathrm{z;R}} = \frac{\sigma_{\mathrm{f},0.008} I}{y_{\max}} = 196.50 \text{ Nmm} \tag{7.8}$$

being I the second moment of area and $y_{\max}$ is the distance from the neutral axis to the most extreme fibre. Finally, the load-carrying capacity is obtain as follows:

$$P_{\mathrm{R}} = \frac{4\mathrm{M}_{\mathrm{z;R}}}{L} = 26.20 \text{ N} \tag{7.9}$$

Therefore, we can conclude that the load-carrying capacity estimated with the proposed probabilistic FEM approach is 43% greater than the load-carrying capacity evaluated with the stress-based approach. The difference in load-carrying capacity prediction is due to the fact that the stress-based design approach assumes that the point of origin of failure coincides with the point of maximum stress, that, in most of the cases, does not occur [27]. In that regard, the distribution in Fig. 7.15 shows that the point of the origin of failure matches with the point of maximum stress in less than one out of five cases.

7.4 Edge-cracked simply supported beam under uniformly distributed load

The cracked beam of Sect. 7.2.2 is now simply supported and subjected to a uniformly distributed load as shown in Fig. 7.16.

Figs. 7.17 and 7.18 show the sampling probability distributions of the failure load q_{f} and critical edge crack size a_c, which are well fitted by the Weibull and Fréchet distributions, respectively. The Weibull and Fréchet parameters were determined

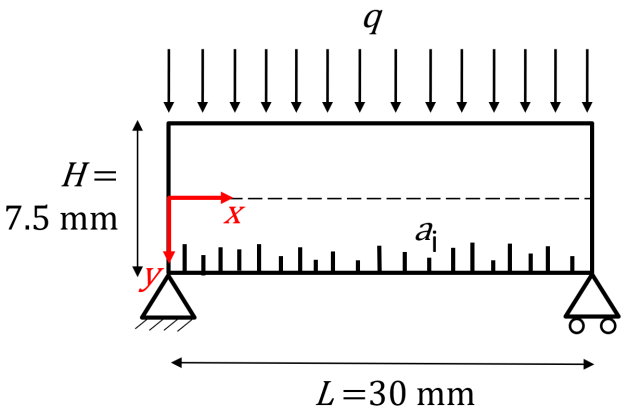

Fig. 7.16 Simply supported beam under uniformly distributed load

using the sample mean and variance by means of the moments method as explained before. Their values are listed in Tab. 7.4.

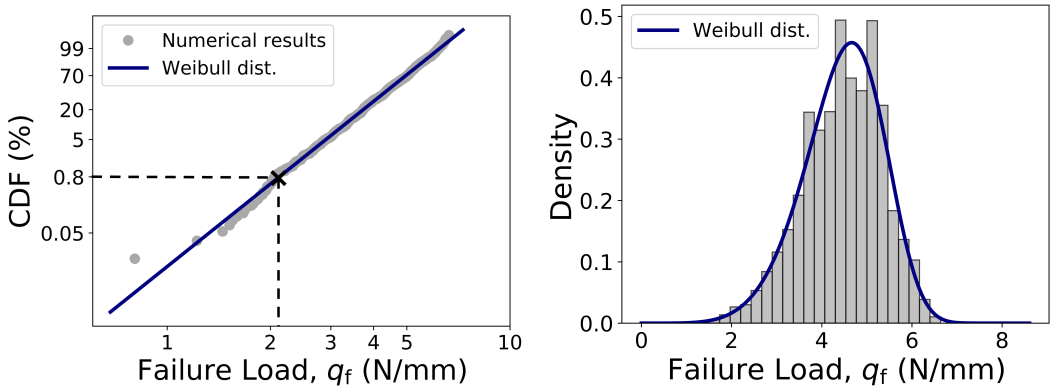

(a) (b)

Fig. 7.17 Weibull distribution of the failure load for the simply supported beam with 29 cracks under uniformly distributed load: (a) Linearised cumulative distribution function; (b) Probability density function

As shown in Fig. 7.19, the coordinate x of the critical crack follows the Gaussian distribution with mean $\bar{x} = 15$ mm and standard deviation $\sqrt{s_x^2} = 7$ mm.

The load-carrying capacity of the beam under uniformly distributed load is obtained from the Weibull diagram (Fig. 7.17) for the 0.8% breakage probability: $q_{f,0.008} = 2.12\,\mathrm{N/mm}$. This value is compared with that estimated using the stress-based failure criterion. As obtained above (see Sect. 7.3), the resistant bending moment of the glass beam shown in Fig. 7.17 is $\mathrm{M_{z;R}} = 196.50$ Nmm Therefore, the

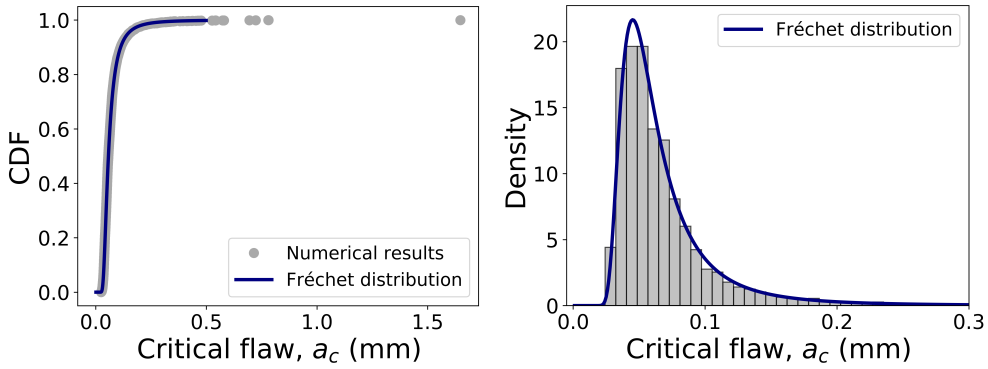

(a) (b)

Fig. 7.18 Fréchet distribution of the critical edge crack size for the simply supported beam with 29 cracks under uniformly distributed load: (a) Cumulative distribution function (CDF); (b) Probability density function

Table 7.4 Weibull and Fréchet parameters for the simply supported beam under uniformly distributed load. Case with 29 cracks

n. of cracks	Pareto param.		Weibull parameters		Fréchet parameters	
m	a_0 (mm)	c	$\hat{\theta}$ (N/mm)	$\hat{\beta}$	$\hat{\lambda}$	$\hat{\alpha}$
29	0.02	3.0	4.8	5.9	2.3E-4	2.8

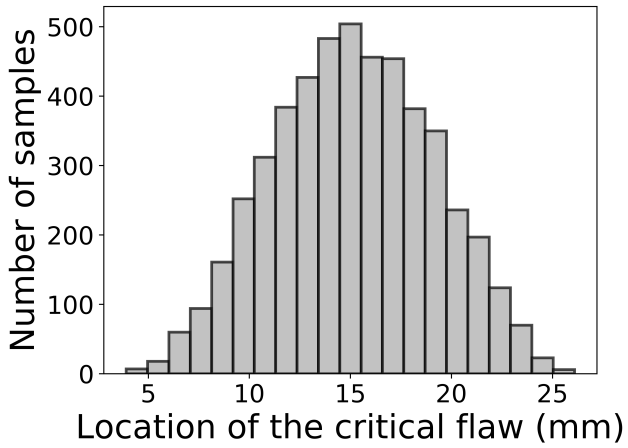

Fig. 7.19 Location of the critical edge crack for the simply supported beam under uniformly distributed load. Case with 29 cracks

load-carrying capacity calculated with the stress-based failure criterion is:

$$q_{\mathrm{R}} = \frac{8\mathrm{M}_{\mathrm{z;R}}}{L^2} = 1.75\ \mathrm{N/mm} \tag{7.10}$$

To conclude, the load-carrying capacity assessed using the suggested probabilistic FEM approach is 21% larger than that obtained using the stress-based failure criterion.

7.5 Edge-cracked cantilever beam under uniformly distributed load

The last example involves a cantilever beam subjected to uniformly distributed load (Fig. 7.20). As in the previous cases, the beam contains 29 cracks, whose size a is Pareto distributed:

$$F(a) = 1 - \left(\frac{0.02}{a}\right)^3 \tag{7.11}$$

The only differences with the previous examples are the support and load conditions of the beam.

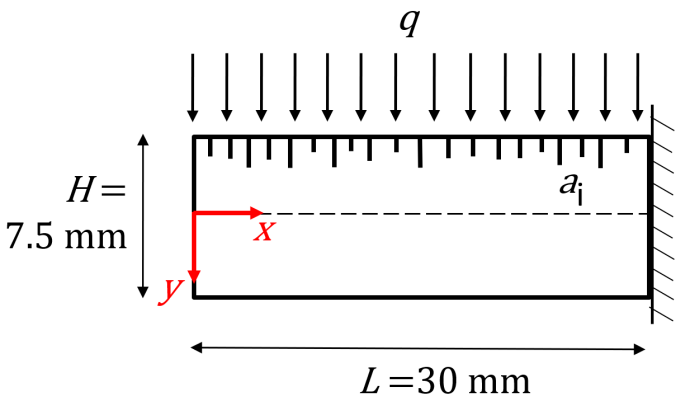

Fig. 7.20 Sketch of the cantilever beam test

The Weibull distribution of the failure load interpolates $N = 5{,}000$ different points $(q_{\mathrm{f,i}}, \hat{G}_i)$ in Fig. 7.22. Each $q_{\mathrm{f,i}}$ value is obtained using the K_{I}-based fracture criterion. Fig. 7.21 depicts the K_{I} distribution along the beam for a single FEM

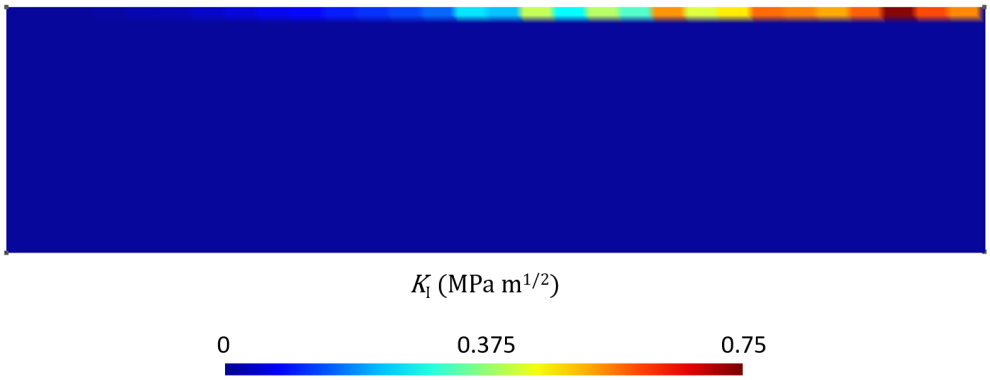

Fig. 7.21 K_I values at the crack tips for a single simulation of the cantilever beam under uniformly distributed load

simulation. Near the fixed end of the beam, where the bending force is greatest, the highest K_I values are found.

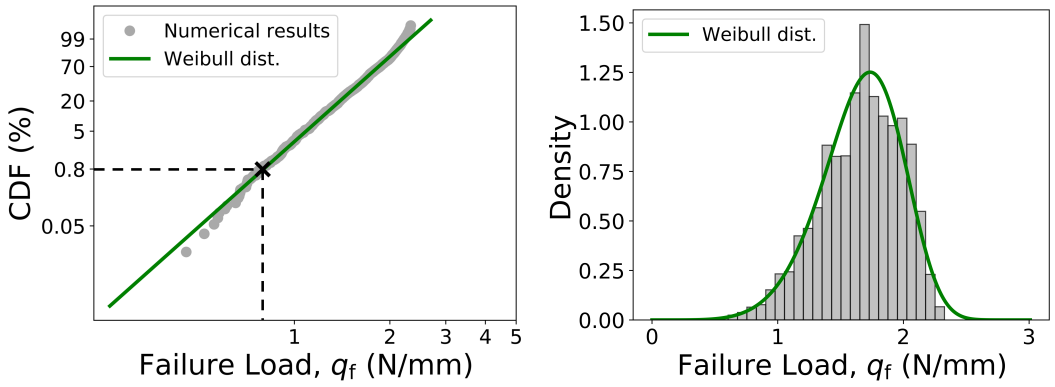

(a) (b)

Fig. 7.22 Weibull distribution of the failure load for the cantilever beam with 29 cracks under uniformly distributed load: (a) Linearised cumulative distribution function; (b) Probability density function

The sampling probability distribution of the critical edge crack size is fitted with the Fréchet distribution in Fig. 7.23. The estimated Fréchet distribution parameters, as well as those of the Weibull distribution, are listed in Tab. 7.5.

The point of origin of failure is located between $x = 15$ mm and $x = 30$ mm as shown in Fig. 7.24.

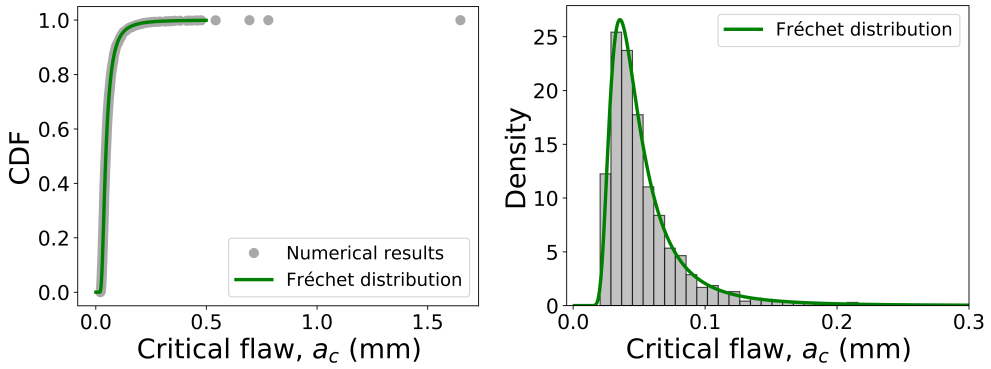

(a) (b)

Fig. 7.23 Fréchet distribution of the critical edge crack size for the cantilever beam with 29 cracks under uniformly distributed load: (a) Cumulative distribution function (CDF); (b) Probability density function

Table 7.5 Weibull and Fréchet parameters for the cantilever beam under uniformly distributed load. Case with 29 cracks

n. of cracks	Pareto param.		Weibull parameters		Fréchet parameters	
m	a_0 (mm)	c	$\hat{\theta}$ (N/mm)	$\hat{\beta}$	$\hat{\lambda}$	$\hat{\alpha}$
29	0.02	3.0	1.8	6.0	1.6E-4	2.7

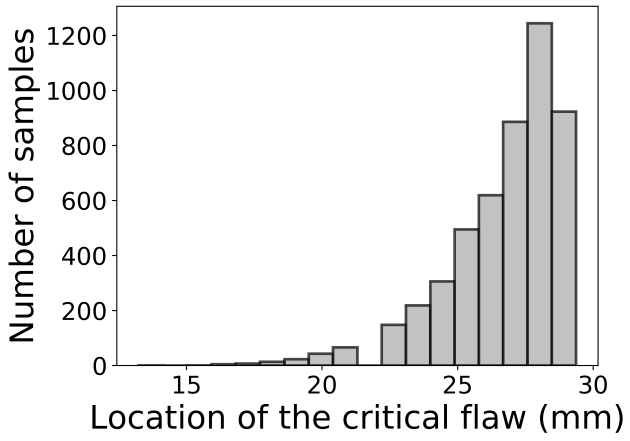

Fig. 7.24 Location of the critical edge crack for the cantilever beam under uniformly distributed load. Case with 29 cracks

The load resistance of the cantilever beam evaluated with the stress-based failure criteria is:

$$q_{\mathrm{R}} = \frac{2\mathrm{M}_{\mathrm{z;R}}}{L^2} = 0.44\mathrm{N/mm} \tag{7.12}$$

whereas the load-carrying capacity obtained with the proposed probabilistic approach is $q_{f,0.008} = 0.80\,\mathrm{N/mm}$ (see Fig. 7.22a). Therefore, the K_I-based prediction is 83% larger than the stress-based prediction.

7.6 Conclusions

A new probabilistic FEM approach is herein proposed for a more reliable and sustainable design of load-bearing glass elements. The main benefit of this methodology consists in the structural optimization of glass components, with a parallel reduction in both emissions and costs. The methodology, that adopts the stress intensity factor-based failure criterion, can be applied to predict the edge strength of glass elements with arbitrary geometry and edge flaws scenario. The proposed approach aims to overcome the drawbacks of the stress-based design approach which relies on a parameter, glass strength, that is not a true material property because it depends on the fracture toughness, the flaws size distribution, the test setup, and the specimen size and geometry.

The case studies reported in this Chapter illustrated that the structural optimization of glass components could not rely on the stress-based design approach, as it underestimates the load-carrying capacity of glass elements, particularly when the stress distribution is far from uniform or in case of stress concentrations. In this regard, for the simply supported beam under uniformly distributed load, the design load-carrying capacity estimated with the K_I-approach is 21% greater than the one evaluated with the stress-based approach, whereas for the three-point bending beam and the cantilever beam this increment is equal to 43% and 83%, respectively. The gap between the two approaches would be larger if irregularities in the geometry of glass components caused stress concentrations.

Unlike prior similar approaches, the developed computational methodology does not require post-processing to get the failure load of glass elements, as the values of the stress intensity factor are directly provided by the XFEM solution. Moreover, the methodology takes into account the interaction among cracks and the effect of stress concentrations on the stress intensity factor. Finally, this methodology allows flexibility in model geometries, boundary conditions, and flaw size statistical distributions.

The current version of the numerical methodology is limited to plane stress/strain models, although its extension to 3D problems is quite straightforward.

Chapter 8

Conclusions and Further Research

8.1 Main Conclusions

A UV-curable polymeric coating has been developed for preventing stress corrosion in glass and a new probabilistic FEM method has been proposed for the structural optimization of glass component. Both the coating and the probabilistic FEM approach aim to maximize the strength and reliability of annealed glass while also pursuing a more sustainable design.

The polymeric coating was prepared with a co-reactive silane primer, a cycloaliphatic UV-curable resin, a fluorinated methacrylate co-monomer, showing good barrier to water vapor, hydrophobicity, transparency and adhesion properties. Thanks to a compositional gradient, good adhesion and high water repellency were present at the same time. The fluorinated co-monomer, which was present in little quantities (1 phr), selectively enriched the coating's outer surface, which caused the hydrophobic behaviour. The adhesion was due to the covalent bonding between the silane layer and the coating itself. Its performance has been assessed by comparing the failure stress of un-coated and coated specimens, tested with the coaxial double ring setup. The results show that the proposed formulation is highly effective for both new and naturally aged glass. The increase of the bending strength corresponding to a probability of failure of 0.8% is equal to 92% for new glass and 62% for aged glass. The durability of the coating against cyclic loading, natural weathering and artificial weathering has been assessed. While after cyclic loading and natural weathering the effectiveness of the coating in preventing stress corrosion was al-

most fully preserved, the effect of the artificial weathering on the durability of the coating was more pronounced. It has to be remarked that the conditions applied for the artificial weathering were very severe in terms of temperature, humidity and UV-light, and exposure period. Even though only the application on the air side has been investigated so far and slight modifications in the formulation of the coating can be brought to further improve its durability, the current formulation has already shown a very good performance, which makes it very promising for future practical applications. Additionally, the developed coating has some advantages compared to other strengthening techniques and coatings: it is solvent free, it has a very fast curing time, it is low-energy consuming, and it can be easily included in the continuous production systems of flat glass as well as it is available for in-situ applications.

The probabilistic FEM approach has been proposed for a more reliable and sustainable design of load-bearing glass elements. The methodology, that adopts a numerical stress intensity factor-based fracture criterion, can be applied to predict the load capacity associated to any given probability of failure of glass components having arbitrary geometry, support conditions and surface/edge flaws scenario. The main novelty consists in the use of the extended finite element method for the numerical modelling of the structural elements, making use of its inherent ability to handle multiple cracks of any length and location without changing the mesh topology, as well as the potential to directly evaluate the stress intensity factors at the crack tips without requiring any post-processing. The method can be adopted for the structural optimization of glass component, since it allows to take into account for the real statistical distribution of the cracks as well as for the actual geometry of the glass component and the support and loading conditions. The numerical results have been showed that the load-carrying capacity of glass components can drastically change even just by varying the loading and support conditions and keeping the statistical distribution of defects unchanged. In particular, it has been shown that, depending on the stress gradient along the glass component, the developed method provides load-carrying capacities larger than the predictions of a stress-based approach, by an extent between 21% and 83%. Although the current version of the numerical methodology has been developed for plane stress/strain models and, therefore, can be directly applied only to in-plane loaded glass elements, whose mechanical resistance is provided by the edge tensile strength, its extension to 3D problems does not change its conceptual foundation and 3D XFEM implementations are also available in

commercial software. In conclusion, the methodology provided has huge potentiality for being generalized for all brittle materials and thus applied to ceramics as well as polysilicon structures for micro-electro-mechanical systems (MEMS).

The results that have been presented are undoubtedly not exhaustive, further studies are suggested below to address the unresolved questions related to the developed coating and the proposed design method.

8.2 Further Research

On the basis of the still-open questions both for the developed coating and proposed design method, the following study directions are recommended:

Durability of the coating - While the durability of the coating against cyclic loading, natural weathering and artificial weathering has been tested in this thesis, the resistance of the coating to scratches, abrasions, impacts and cleaning has to be assessed. Additionally, the artificial weathering could be conducted in accordance to the standards for structural sealants (see ETAG 002-5.1.4.2.1 [83] and EN ISO 11431 [84]). Finally, the gradual delamination due to water attack at the edges of the coating must be analysed. Concerning all these aspects, Refs. [16], [136] and [24] can give guidance.

Environmental impact of the coating - UV-cured coatings were selected for this study because they not include solvents, which makes them attractive from a health and environmental perspective. Furthermore, the polymerization of these coating does not require heating, limiting the energy consumption. Finally, regarding the choice of the fluorinated comonomer, attention was paid in order to use a non-toxic and non-bioaccumulative product, approved by both the U.S. Food & Drugs Administration (FDA) and the European Food Safety Authority (EFSA). Besides the choices made, some additional aspects concerning the effect of the coating on the environment should be investigated. In this regard, the effect of the coating on the potential recycling of the glass and the effect of the reduction in glass transparency on the photosynthesis rate of plants have to be study.

Application of the coating at the cut edges - The performance of the coating when applied on the cut edges of glass plates should be analysed.

Extension to 3D problems of the design method - The current version of the developed numerical methodology for the structural optimization of glass component is limited to plane stress/strain models, its extension to 3D problems must be pursued in order to make it applicable to several products of the glass industry.

Sensitivity analysis of the design method - The load carrying capacity is evaluated with the proposed design method by assuming the crack position, the crack density, and the statistical distribution of the micro cracks. The crack density and the statistical distribution of the cracks could be evaluated, within confidence intervals, by means of experimental tests, while the crack position could be selected randomly from an uniform distribution. To quantify how the uncertainties on these three parameters affect the output variable, a sensitivity analysis should be performed. By the analysis of interactions between the variables, the phenomenon of the failure of glass components under arbitrary stress distributions could be better understood. As a result, decisions about the design and optimization of glass components can be made with greater confidence.

References

[1] B. R. Lawn. *Fracture of Brittle Solids - Second Edition*. Cambridge University Press, 1993.

[2] S. M. Wiederhorn. Influence of water vapor on crack propagation in soda-lime glass. *J. Am. Ceram. Soc.*, 50:407–414, 1967.

[3] B. Arkles. Tailoring surfaces with silanes. *Chemtech*, 7:766–778, 1977.

[4] EN 16612:2019. *Glass in building - Determination of the lateral load resistance of glass panes by calculation*. European Committee for Standardization, Brussels, 2019.

[5] ASTM E1300-16. *Standard practice for determining load resistance of glass in buildings*. American Society for Testing Materials, 2016.

[6] K. Rege and H. G. Lemu. A review of fatigue crack propagation modelling techniques using FEM and XFEM. *IOP Conference Series: Materials Science and Engineering*, 276:012027, dec 2017.

[7] F. Oikonomopoulou, T. Bristogianni, F. Veer, and R. Nijsse. The construction of the crystal houses façade: challenges and innovations. *Glass Structures & Engineering*, 3:87–108, 03 2018.

[8] J. Cupać, C. Louter, and A. Nussbaumer. Flexural behaviour of post-tensioned glass beams: Experimental and analytical study of three beam typologies. *Composite Structures*, 255:112971, 2021.

[9] C. Kothe, A. Bodenko, F. Nicklisch, and C. Louter. Thin glass in façades: Adhesive joints for thin glass composite panels with 3D printed polymer cores. *Civil Engineering Design*, 3(1-2):35–42, 2021.

[10] M. Haldimann, A. Luible, and M. Overend. *Structural Use of Glass*. International Association for Bridge and Structural Engineering IABSE, Zurich, 2008.

[11] M. Jotz, J. Schneider, and E. Radlein. Introducing the "Cylinder Fit Test", a simplified edge strength measurement method for ultra thin glass. In J. Schneider and B. Weller, editors, *Engineered Transparency 2018 - Glass in Architecture and Structural Engineering*, pages 65–73. Wilhelm Ernst & Sohn, 2018.

[12] M. B. Abrams and D. J. Green. Prediction of crack propagation and fracture in residually stressed glass as a function of the stress profile and flaw size distribution. *J. Eur. Ceram. Soc.*, 26:2677–2684, 2006.

[13] M. Overend, S. De Gaetano, and M. Haldimann. Diagnostic interpretation of glass failure. *Struct. Eng. Int.*, 17:151–158, 2007.

[14] M. Overend and K. Zammit. A computer algorithm for determining the tensile strength of float glass. *Eng. Struct.*, 45:68–77, 2012.

[15] B. Afolabi, H. Scott Norville, and S. M. Morse. Experimental study of weathered tempered glass plates from the Northeastern United States. *ASCE J. Architect. Eng.*, 22:04016010, 2016.

[16] K. C. Datsiou and M. Overend. Artificial ageing of glass with sand abrasion. *Constr. Build. Mater.*, 142:536–551, 2017.

[17] K. C. Datsiou and M. Overend. The strength of aged glass. *Glass Struct. Eng.*, 2:105–120, 2017.

[18] M. Overend and C. Louter. The effectiveness of resin-based repairs on the inert strength recovery of glass. *Constr. Build. Mater.*, 85:165–174, 2015.

[19] G. Pisano and G. Royer Carfagni. The statistical interpretation of the strength of float glass for structural applications. *Constr. Build. Mater.*, 98:741–756, 2015.

[20] D. T. Kinsella and K. Persson. A numerical method for analysis of fracture statistics of glass and simulations of a double ring bending test. *Glass Structures and Engineering*, 3:139–152, 2018.

[21] Y. Sakata, N. Terasaki, and K. Nonaka. Development of a novel non-contact inspection technique to detect micro cracks under the surface of a glass substrate by thermal stress-induced light scattering method. *Optics & Laser Technology*, 90:80–83, 2017.

[22] Z. Pan, J. Yang, X. Wang, F. Wang, I. Azim, and C. Wang. Image-based surface scratch detection on architectural glass panels using deep learning approach. *Construction and Building Materials*, 282:122717, 2021.

[23] A. A. Griffith and G. I. Taylor. Vi. the phenomena of rupture and flow in solids. *Philosophical Transactions of the Royal Society of London. Series A, Containing Papers of a Mathematical or Physical Character*, 221(582-593):163–198, 1921.

[24] J. Schneider, S. Schula, and W. P. Weinhold. Characterisation of the scratch resistance of annealed and tempered architectural glass. *Thin Solid Films*, 520(12):4190–4198, 2012. 8th International Conference on Coatings on Glass and Plastics — ICCG8.

[25] F. Veer and Y. Rodichev. The structural strength of glass: Hidden damage. *Strength of Materials*, 43:302–315, 05 2011.

[26] M. Haldimann. *Fracture strength of structural glass elements – Analytical and numerical modelling, testing and design*. PhD thesis, École Polytechnique Fédérale de Lausanne, Lausanne, Switzerland, 2006.

[27] M. Overend, G. A. R. Parke, and D. Buhagiar. Predicting Failure in Glass—A General Crack Growth Model. *Journal of Structural Engineering*, 133:1146–1155, 08 2007.

[28] I. Nurhuda, N. T. K. Lam, E. F. Gad, and I. Calderone. Estimation of strengths in large annealed glass panels. *International Journal of Solids and Structures*, 47(18):2591–2599, 2010.

[29] D. Z. Yankelevsky. Strength prediction of annealed glass plates – a new model. *Engineering Structures*, 79:244–255, 2014.

[30] D. T. Kinsella and K. Persson. An analysis of glass fracture statistics. volume 6. Challenging Glass 6, 2018.

[31] CEN/TS 19100-1. *Design for glass structures – Part 1: Basis of design and materials*. European Standard, European Committee for Standardization (CEN), Brussels, 2021.

[32] S. V. D. Zwaag. The concept of filament strength and the Weibull modulus. *Journal of Testing and Evaluation*, 17:292–298, 1989.

[33] S. A. Kotrechko. A local approach to brittle fracture analysis and its physical interpretation. *Strength of Materials*, 35:334–345, 2003.

[34] L. Afferrante, M. Ciavarella, and E. Valenza. Is Weibull's modulus really a material constant? Example case with interacting collinear cracks. *International Journal of Solids and Structures*, 43(17):5147–5157, 2006.

[35] T. A. Michalske and S. W. Freiman. A molecular mechanism for stress corrosion in vitreous silica. *J. Am. Ceram. Soc.*, 66:284–288, 1983.

[36] S. M. Wiederhorn and L. H. Bolz. Stress corrosion and static fatigue of glass. *J. Am. Ceram. Soc.*, 53:543–548, 1967.

[37] R. J. Charles and W. B. Hillig. The kinetics of glass failure by stress-corrosion. In *Symposium on Mechanical Strength of Glass and Ways of Improving It*, pages 511–527. Union Scientifique Continentale du Verre, Charleroi, Belgium, 1962.

[38] R. Gy. Ion exchange for glass strengthening. *Materials Science and Engineering B: Solid-State Materials for Advanced Technology*, 149:159–165, 2008.

[39] Q. Gao, Q. Liu, M. Li, X. Li, Y. Liu, C. Song, J. Wang, J. Liu, G. Shen, and G. Han. Effect of glass tempering on microstructure and functional properties of SnO_2:F thin film prepared by atmosphere pressure chemical vapor deposition. *Thin Solid Films*, 544:357–361, 2013.

[40] T. Belytschko and T. Black. Elastic crack growth in finite elements with minimal remeshing. *International Journal for Numerical Methods in Engineering*, 45(5):601–620, 1999.

[41] N. Moës, J. Dolbow, and T. Belytschko. A finite element method for crack growth without remeshing. *International Journal for Numerical Methods in Engineering*, 46(1):131–150, 1999.

[42] B. L. Karihaloo and Q. Z. Xiao. Direct evaluation of accurate sif with pum. In *Advances in Fracture Research*. 10th Intenational conference on fracture - ICF10, 2001.

[43] R. Gy. Stress corrosion of silicate glass: review. *J. Non-Cryst. Solids*, 316:1–11, 2003.

[44] L. Grenet. Mechanical strength of glass. *Bulletin de la Société d'Encouragement pour l'Industrie Nationale*, 5(4):838–848, 1899.

[45] C. Ronchetti, M. Lindqvist, C. Louter, and G. Salerno. Stress-corrosion failure mechanisms in soda–lime silica glass. *Eng. Fail. Anal.*, 35:427–438, 2013.

[46] P. C. P. Bouten. *Lifetime of pristine optical fibres*. Technische Universiteit Eindhoven, Eindhoven, The Netherlands, 1987.

[47] C. R. Kurkjian, P. G. Simpkins, and D. Inniss. Strength, degradation, and coating of silica lightguides. *Glass Sci. Technol.*, 76:1106–1112, 1993.

[48] X. M. Chen, B. Ellis, F. Wang, and A. B. Seddon. Strengthening of glass rods with ormosil polymeric coatings. *J. Non-Cryst. Solids*, 185:1–17, 1995.

[49] M. Lindqvist, C. Louter, and J.-P. Lebet. Edge-strengthening of structural glass with protective coatings. *Key Eng. Mat.*, 488–489:331–334, 2012.

[50] B. Wang, B. V. Cunning, S.-Y. Park, M. Huang, J.-Y. Kim, and R. S. Ruoff. Graphene coatings as barrier layers to prevent the water-induced corrosion of silicate glass. *ACS Nano*, 10:9794–9800, 2016.

[51] R. Bongiovanni and A. Vitale. 8 - smart multiphase polymer coatings for the protection of materials. In M.F. Montemor, editor, *Smart Composite Coatings and Membranes*, Woodhead Publishing Series in Composites Science and Engineering, pages 213–234. Woodhead Publishing, 2016.

[52] N. Corrigan, J. Yeow, P. Judzewitsch, J. Xu, and C. Boyer. Seeing the light: Advancing materials chemistry through photopolymerization. *Angewandte Chemie International Edition*, 58(16):5170–5189, 2019.

[53] A. Vitale, R. Bongiovanni, and B. Ameduri. Fluorinated oligomers and polymers in photopolymerization. *Chemical Reviews*, 115:8835–8866, 2015.

[54] K. Zhang, T. Li, T. Zhang, C. Wang, C. Wang, and M. Wu. Adhesion improvement of uv-curable ink using silane coupling agent onto glass substrate. *Journal of Adhesion Science and Technology*, 27(13):1499–1510, 2013.

[55] L. Yang and J.L. Thomason. Effect of silane coupling agent on mechanical performance of glass fibre. *Journal of Materials Science*, 48:1947–1954, 2013.

[56] Z. Wang, I. T. Cousins, M. Scheringer, and K. Hungerbühler. Fluorinated alternatives to long-chain perfluoroalkyl carboxylic acids (PFCAs), perfluoroalkane sulfonic acids (PFSAs) and their potential precursors. *Environment International*, 60:242–248, 2013.

[57] M. Kotthoff and M. Bücking. Four Chemical Trends Will Shape the Next Decade's Directions in Perfluoroalkyl and Polyfluoroalkyl Substances Research. *Frontiers in Chemistry*, 6, 2018.

[58] S. Dalle Vacche, S. Forzano, A. Vitale, M. Corrado, and R. Bongiovanni. Glass lap joints with UV-cured adhesives: Use of a perfluoropolyether methacrylic resin in the presence of an acrylic silane coupling agent. *International Journal of Adhesion and Adhesives*, 92:16–22, 2019.

[59] I. Swentek and J.T. Wood. Measuring polymer composite interfacial strength. *Composites Part B: Engineering*, 58:235–241, 2014.

[60] S. Wu. *Polymer interface and adhesion*. Basel, New York, 1982.

[61] DIN 4768. *Determination of Surface Roughness Values of the Parameters Ra, Rz, Rmax by Means of Electrical Contact (Stylus) Instruments; Terminology, Measuring Conditions*. German Institute for Standardisation, Berlin (Germany), 1990.

[62] ASTM D870-15. *Standard Practice for Testing Water Resistance of Coatings Using Water Immersion*. ASTM International, West Conshohocken (USA), 2015.

[63] ASTM F372-99. *Standard Test Method for Water Vapor Transmission Rate of Flexible Barrier Materials Using an Infrared Detection Technique*. ASTM International, West Conshohocken (USA), 2003.

[64] R. Bongiovanni, V. Lombardi, A. Priola, C. Tonelli, and A. Meo. Surface properties of acrylic coatings containing perfluoropolyether chains. *Surface Coatings International Part B: Coatings Transactions*, 86:53–57, 2003.

[65] C.R. Vistas, A.C.P. Águas, and G.N.M. Ferreira. Silanization of glass chips—A factorial approach for optimization. *Applied Surface Science*, 286:314–318, 2013.

[66] A. Vitale, A. Priola, C. Tonelli, and R. Bongiovanni. Nanoheterogeneous networks by photopolymerization of perfluoropolyethers and acrylic comonomers. *Polym. Int.*, 62:1395–1401, 2013.

[67] R. Bongiovanni, G. Malucelli, A. Pollicino, C. Tonelli, G. Simeone, and A. Priola. Perfluoropolyether structures as surface modifying agents of UV-curable systems. *Macromol. Chem. Phys.*, 199:1099–1105, 1998.

[68] ASTM C1499-19. *Standard Test Method for Monotonic Equibiaxial Flexural Strength of Advanced Ceramics at Ambient Temperature*. ASTM International, West Conshohocken (USA), 2019.

[69] K. C. Datsiou and M. Overend. Weibull parameter estimation and goodness-of-fit for glass strength data. *Struct. Saf.*, 73:29–41, 2018.

[70] S. Amma, J. Luo, C. G. Pantano, and S. H. Kim. Specular reflectance (SR) and attenuated total reflectance (ATR) infrared (IR) spectroscopy of transparent flat glass surfaces: A case study for soda lime float glass. *J. Non-Cryst. Solids*, 428:189–196, 2015.

[71] EN 1288-2:2000. *Glass in building - Determination of bending strength of glass - Part 2: Coaxial double ring test on flat specimens with large test surface areas*. European Committee for Standardization, Brussels, 2000.

[72] A. G. EVANS. A general approach for the statistical analysis of multiaxial fracture. *Journal of the American Ceramic Society*, 61(7-8):302–308, 1978.

[73] EN 12603:2002. *Glass in building - Procedures for goodness of fit and confidence intervals for Weibull distributed glass strength data*. European Committee for Standardization, Brussels, 2002.

[74] E. Le Bourhis. *Glass - Mechanics and Technology*. Wiley-VHC, Weinheim, Germany, 2014.

[75] W. L. Beason and J. R. Morgan. Glass failure prediction model. *J. Struct. Eng.*, 111:2058–2059, 1985.

[76] S.W. Rust, F.R. Todt, B. Harris, D. Neal, and M. Vangel. Statistical methods for calculating material allowables for MIL-HDBK-17. In C.C. Chamis, editor, *Test Methods and Design Allowables for Fibrous Composites: 2nd Volume*, pages 136–149. ASTM International, 1989.

[77] M. Berlinger, S. Kolling, and J. Schneider. A generalized anderson–darling test for the goodness-of-fit evaluation of the fracture strain distribution of acrylic glass. *Glass Structures & Engineering*, 6:1–14, 06 2021.

[78] R. Ballarini, G. Pisano, and G. Royer-Carfagni. The lower bound for glass strength and its interpretation with generalized weibull statistics for structural applications. *Journal of Engineering Mechanics*, 142(12):04016100, 2016.

[79] T. A. Michalske. Fractography of slow fracture in glass. In J. J. Mecholsky and S. R. Powell, editors, *Fractography of Ceramic and Metal Failures*, pages 121–136. American society for testing and materials - ASTM STP 827, 1984.

[80] T. A. Michalske, V. D. Fréchette, and R. Hudson. *Dynamic Effects of Liquids on Surface Crack Extension in Glass*. Pergamon, New York (USA), 1981.

[81] G. Quinn. *Fractography of Ceramics and Glasses, 2nd edition*. 2016.

[82] EN ISO 16474-3:2013. *Paints and varnishes - Methods of exposure to laboratory light sources*. European Committee for Standardization, Brussels, 2013.

[83] EOTA. *ETAG002 - Guidiline for European technical approval for structural sealant glazing kits, t, Part 1: Supported and Unsupported Systems*. 2012.

[84] EN ISO 11431:2002. *Building construction — Jointing products — Determination of adhesion/cohesion properties of sealants after exposure to heat, water and artificial light through glass*. European Committee for Standardization, Brussels, 2002.

[85] P.C. Paris and F. Erdogan. A critical analysis of crack propagation laws. *J. Basic Eng ASME*, 18:528–534, 1963.

[86] B.-T. Lü. Fatigue strength prediction of soda-lime glass. *Theoretical and Applied Fracture Mechanics*, 27(2):107–114, 1997.

[87] J. Schneider and J. Hilcken. Cyclical fatigue of annealed and of thermally tempered soda-lime-silica glass. *MATEC Web of Conferences*, 165:18003, 01 2018.

[88] A. G. Evans and E. R. Fuller. Crack propagation in ceramic materials under cyclic loading conditions. *Metallurgical Transactions*, 5:27–33, 1974.

[89] P. Boyce, N. Eklund, S. Magnum, C. Saalfield, and L. Tang. Minimum acceptable transmittance of glazing. *Light. Res. Technol.*, 27:145–152, 1995.

[90] B. Arkles. Hydrophobicity, hydrophilicity and silanes. *Paint and Coatings Industry*, 22:114, 10 2006.

[91] G. Trusiano, A. Vitale, M. Rizzello, C. Bonneaud, C. Joly-Duhamel, C. M. Friesen, and R. Bongiovanni. Controlling perfluoropolyalkylether rearrangements at the surface of photocured networks. *European Polymer Journal*, 121:109285, 2019.

[92] D.R. Jenkins and R.G. Mathey. *Hail impact testing procedure for solar collector covers*. NBSIR ; 82-2487. U.S. Dept. of Commerce, National Bureau of Standards, Washington, DC, 1982.

[93] M. Corrado, A. Infuso, and M. Paggi. Simulated hail impacts on flexible photovoltaic laminates: testing and modelling. *Meccanica*, 52:1425–1439, 2017.

[94] Z. Wang, A. Pakoulev, Y. Pang, and D. D. Dlott. Vibrational substructure in the oh stretching transition of water and hod. *J. Phys. Chem. A*, 108 (42):9054–9063, 2004.

[95] R. Bongiovanni, A. Medici, A. Zompatori, S. Garavaglia, and C. Tonelli. Perfluoropolyether polymers by UV curing: design, synthesis and characterization. *Polym. Int.*, 61:65–173, 2012.

[96] R. Ballarini, G. Pisano, and G. Royer Carfagni. New calibration of partial material factors for the structural design of float glass. comparison of bounded and unbounded statistics for glass strength. *Construction and Building Materials*, 121:69–80, 2016.

[97] B. Arkles, Y. Pan, and Y. Mi Kim. The role of polarity in the structure of silanes employed in surface modification. In K.L. Mittal, editor, *Silanes and other Coupling Agents*, volume 5, pages 51–64. CRC Press, 2009.

[98] M. Wei, R. S. Bowman, J. L. Wilson, and N. R. Morrow. Wetting properties and stability of silane-treated glass exposed to water, air, and oil. *J. Colloid Interface Sci.*, 157(1):154–159, 1993.

[99] M. Vandebroek, J. Belis, C. Louter, and S. Caspeele. Influence of the load history on the edge strength of glass with arrised and ground edge finishing. *Engineering Fracture Mechanics*, 104:29–40, 2013.

[100] G. Mariggiò, S. Dalle Vacche, R. Bongiovanni, C. Louter, and M. Corrado. A durable coating to prevent stress corrosion effects on the surface strength of annealed glass. *Glass Structures & Engineering*, 6:449–462, 2021.

[101] G. Pisano, A. Bonati, and G. Royer-Carfagni. The effect of size and stress state on the strength of architectural glass. experiments versus theory. *Construction and Building Materials*, 283:122635, 2021.

[102] N. Papadopoulos and C. Drosou. Influence of weather conditions on glass properties. *Journal of the University of Chemical Technology and Metallurgy*, 47:429–439, 2012.

[103] J. Kleuderlein, F. Ensslen, and J. Schneider. Study on edge strength of float glass as a function of edge processing. *Stahlbau*, 85:149–159, 04 2016.

[104] S. Müller-Braun, M. Seel, M. König, P. Hof, J. Schneider, and M. Oechsner. Cut edge of annealed float glass: crack system and possibilities to increase the edge strength by adjusting the cutting process. *Glass Structures & Engineering*, 5:3–25, 2020.

[105] S. Schula, J. Schneider, M. Vandebroek, and J. Belis. Fracture strength of glass, engineering testing methods and estimation of characteristic values. In Jan Belis, Christian Louter, and Danijel Mocibob, editors, *COST Action TU0905, Mid-term Conference on Structural Glass, Proceedings*, pages 223–234. Taylor & Francis Group, 2013.

[106] F. H. Kulhawy and K. Phoon. Engineering Judgment in the Evolution from Deterministic to Reliability-Based Foundation Design. In M.J.S. Roth C.D. Shackelford, P.P. Nelson, editor, *Proceedings of Uncertainty 1996, Uncertainty in the Geologic Environment - From Theory to Practice (GSP 58)*, New York, 1996. ASCE.

[107] M. J. Lamela, A. Ramos, P. Fernández, A. Fernández-Canteli, C. Przybilla, C. Huerta, and A. Pacios. Probabilistic characterization of glass under different type of testing. *Procedia Materials Science*, 3:2111–2116, 2014. 20th European Conference on Fracture.

[108] W. L. Beason. *A failure prediction model for window glass*. Texas Tech University, 1980.

[109] W. L. Beason and J. R. Morgan. Glass failure prediction model. *Journal of Structural Engineering*, 110(2):197–212, 1984.

[110] W. Weibull. A statistical theory of the strength of materials. Proceedings of the Royal Swedish Academy of Engineering, 1939.

[111] M. Lindqvist, M. Vandebroek, C. Louter, and J. Belis. Influence of edge flaws on failure strength of glass. 06 2011.

[112] M. Vandebroek, J. Belis, C. Louter, and G. Van Tendeloo. Experimental validation of edge strength model for glass with polished and cut edge finishing. *Engineering Fracture Mechanics*, 96:480–489, 2012.

[113] G. R. Irwin. Analysis of Stresses and Strains Near the End of a Crack Traversing a Plate. *Journal of Applied Mechanics*, 24(3):361–364, 1957.

[114] J. Mencik. *Strength and Fracture of Glass and Ceramics, Glass Science and Technology*, volume 12. Elsevier, Amsterdam, 1992.

[115] H. Tada, P. C. Paris, and G. R. Irwin. *The Stress Analysis of Cracks Handbook*. The American Society of Mechanical Engineers Press, 2000.

[116] J. Poloniecki and T. Wilshaw. Determination of surface crack size densities in glass. *Nat. Phys. Sci.*, 229:226–227, 1971.

[117] J. Poloniecki. *Statistical Investigation of Surface Flaws. Ph.D. Thesis*. The University of Sussex, 1974.

[118] R. Tandon, B. Paliwal, and C. Gibson. Practical aspects of using Hertzian ring crack initiation to measure surface flaw densities in glasses: influence of humidity, friction and searched areas. *Philosophical Magazine*, 93:2847–2863, 2013.

[119] C. Forbes, M. Evans, N. Hastings, and B. Peacock. *Statistical Distributions, 4th Edition*. Wiley, 2010.

[120] G. Ventura. On the elimination of quadrature subcells for discontinuous functions in the eXtended Finite-Element Method. *Int J Numer Meth Eng*, 66:761–795, 2006.

[121] X. Y. Liu, Q. Z. Xiao, and B. L. Karihaloo. Xfem for direct evaluation of mixed mode sifs in homogeneous and bi-materials. *International Journal for Numerical Methods in Engineering*, 59(8):1103–1118, 2004.

[122] O. C. Zienkiewicz, R. L. Taylor, and J. Z. Zhu. In *The Finite Element Method: its Basis and Fundamentals (Seventh Edition)*. Butterworth-Heinemann, Oxford, seventh edition, 2013.

[123] E. Benvenuti, G. Ventura, and N. Ponara. Finite element quadrature of regularized discontinuous and singular level set functions in 3d problems. *Algorithms*, 5(4):529–544, 2012.

[124] E. Benvenuti, G. Ventura, N. Ponara, and A. Tralli. Variationally consistent extended fe model for 3d planar and curved imperfect interfaces. *Computer Methods in Applied Mechanics and Engineering*, 267:434–457, 2013.

[125] J. Albinmousa, N. Merah, and S.M.A. Khan. A model for calculating geometry factors for a mixed-mode I–II single edge notched tension specimen. *Engineering Fracture Mechanics*, 78(18):3300–3307, 2011.

[126] Q. Z. Xiao and B. L. Karihaloo. Improving the accuracy of XFEM crack tip fields using higher order quadrature and statically admissible stress recovery. *International Journal for Numerical Methods in Engineering*, 66(9):1378–1410, 2006.

[127] J. P. Pereira, C. A. Duarte, D. Guoy, and X. Jiao. hp-Generalized FEM and crack surface representation for non-planar 3-D cracks. *International Journal for Numerical Methods in Engineering*, 77(5):601–633, 2009.

[128] G. Ventura and E. Benvenuti. Equivalent polynomials for quadrature in Heaviside function enriched elements. *Int J Numer Meth Eng*, 102:688–710, 2015.

[129] G. Mariggiò, S. Fichera, M. Corrado, and G. Ventura. EQP - A 2D/3D library for integration of polynomials times step function. *SoftwareX*, 12:100636, 2020.

[130] K. Sanders, F. Bos, E. Brincke, and J. Belis. Edge strength of core drilled and waterjet cut holes in architectural glass. *Glass Structures & Engineering*, 6:1–15, 06 2021.

[131] NEN 2608:2014. *Glass in building—requirements and determination method*. Netherlands Standardization Institute, 2014.

[132] H. Auradou, D. Vandembroucq, C. Guillot, and E. Bouchaud. A probabilistic model for the stress corrosion fracture of glass. Washington DC, August 2001. Transactions, SMiRT 16.

[133] Z. D. Jiang, A. Zeghloul, G. Bezine, and J. Petit. Stress intensity factors of parallel cracks in a finite width sheet. *Engineering Fracture Mechanics*, 35(6):1073–1079, 1990.

[134] O. García. Simplified method-of-moments estimation for the Weibull distribution. *New Zealand Journal of Forestry Science*, 11:304–306, 1 1981.

[135] P. Ramos, F. Louzada, E. Ramos, and S. Dey. The Fréchet distribution: Estimation and application an overview. *Journal of Statistics and Management Systems*, 23:549–578, 05 2020.

[136] J. Giese-Hinz, C. Kothe, C. Louter, and B. Weller. Mechanical and chemical analysis of structural silicone adhesives with the influence of artificial aging. *International Journal of Adhesion and Adhesives*, 117:103019, 2022. AB2021 Special Issue.